How effective is the Mann turbulence model in predicting horizontal turbulence from vertical data?

Mali Ones

University of Bergen

June 2024

Thesis for Master of Science Degree written as a part of the Integrated Master's program in Energy at the Geophysical Institute at the University of Bergen.

©Copyright Mali Ones
The material in this publication is protected by copyright law.

Year: June 2024
Title: How effective is the Mann turbulence model in predicting horizontal turbulence from vertical data?
Author: Mali Ones

Acknowledgements

First of all, I would like to thank my main supervisor Etienne Cheynet for being so helpful and accessible throughout the work on the thesis. Your dedication has been absolutely crucial for the final result. I would also like to thank my co-supervisor Prof. Joachim Reuder for valuable knowledge and input. I have gained a lot of experience by collaborating with both of you!

Thanks to the research project Large Offshore Wind Turbines for financial support to attend the EERA DeepWind conference in connection with the thesis.

Thanks to family and friends who have shown interest in the thesis, even though it has been difficult for me to explain its content to people lacking knowledge in the field. Apologies for any lack of clarity in my response.

Finally, I would like to thank my faithful study buddy, Kamilla Valla Hagen, for going through this process with me. Thanks for all nice lunch breaks, emotional support, and opinions on figures (especially!). This past year would have been far worse without you by my side.

Abstract

Offshore wind turbines are approaching 300 m.a.s.l., where the dynamics of the atmospheric turbulence remain unclear. Present understanding is limited, with direct measurements above 100 m from the sea surface being scarce.

The thesis assesses the feasibility of deducing the along-wind spectrum from measurements of the vertical velocity combined with numerical modeling, using the uniform shear model (Mann, 1994). The vertical component experiences less influence from mesoscale motions, enhancing stationarity and potentially simplifying instrumentation and data collection. The primary objective is to determine if the along-wind standard deviation (σ_u), the governing parameter in modeling wind loads on wind turbines (Wiley et al., 2023), can be accurately estimated from the deduced along-wind spectrum.

The method was tested on sonic anemometer data from the FINO1 platform at 81.5 m collected during 2007 and 2008 for two different cases: 1) all velocity components were known, and 2) only the vertical component was known. Fitting to all components showed good agreement between the estimated σ_u and the target values. Encountering local minima was a challenge when fitting to only the vertical component. This was partially avoided by using a narrower wavenumber interval and lower iteration tolerances in the fitting. The method performed quite well for mean wind speeds up to 17 m s^{-1}. For higher mean wind speeds, σ_u was significantly underestimated, possibly due to underestimation of the model parameter Γ.

Additionally, the method was briefly tested on vertical velocity data from a Leosphere WindCube 100S, with a novel attempt to correct for spatial averaging. Lack of simultaneous point-measurements prevented verification of the correction method and the deduced along-wind spectrum obtained from fitting the uniform shear model to the original and corrected spectrum.

Acronyms

ABL atmospheric boundary layer

CW continuous wave

DBS doppler beam swinging

LOS line-of-sight

MOST Monin-Obukhov similarity theory

PPI plan position indicator

PSD power spectral density

RDT rapid distortion theory

RHI range height indicator

RMSE root mean square error

US uniform shear

VAD velocity azimuth display

Contents

Chapter 1

Introduction

1.1 Motivation

The world is facing one of the greatest crises in history - the climate crisis (Hoegh-Guldberg et al., 2019). A crucial step in mitigating this crisis is to significantly reduce, preferably phase out, the use of fossil fuel. To facilitate this transition, there is an urgent need to strengthen renewable energy production. Following hydropower, wind power stands presently as the second-largest contributor to global renewable electricity generation (IEA, 2023). Together with solar energy, wind plays a central role in realizing the IEA's ambitious goal of achieving Net Zero Emissions by 2050 (IEA, 2021). To reach this target, wind electricity production must reach 7400 TWh by 2030, requiring an average annual capacity increase of 17%. However, as of 2022, the annual increase stood at 14% (IEA, 2023). The continued growth of wind power is essential for meeting renewable energy targets and combating the climate crisis, necessitating ongoing research and innovation in the field.

Wind turbines have grown in size since the early 2000s (EERE, 2023). This is because the power production of a wind turbine is proportional to the square of the rotor radius and the cube of the wind speed, which generally increases with altitude. Offshore environments are characterized by higher wind speeds and lower atmospheric turbulence compared to onshore, facilitating wind energy production. This has led to offshore wind turbines reaching heights of nearly 300 m above sea level. At such heights the dynamics of atmospheric turbulence remain unclear. Present understanding

is limited, with direct measurements above 100 m from the sea surface being scarce. This gap in knowledge represents a significant obstacle in the field of wind energy research, as identified by Veers et al. (2019).

1.2 Problem statement and objectives

This study aims to enhance our understanding of offshore wind turbulence from 50 m to 300 m above the surface by combining field measurements and numerical modelling, using the uniform shear model (Mann, 1994). The along-wind spectrum is of particular interest as the standard deviation of the along-wind component (σ_u) can be estimated from its spectrum. σ_u is the governing parameter in modeling of wind loads on a wind turbine (Wiley et al., 2023). Therefore, the objectives of the thesis are to:

- assess the feasibility of deducing the along-wind spectrum from measurements of only the vertical wind component,
- assess if σ_u can be accurately estimated from the deduced spectrum.

To the author's knowledge, such a study has not been conducted before. The motivation for using only the vertical component lies in its lesser sensitivity to non-turbulent (mesoscale) motions compared to the horizontal components, thereby resulting in greater stationarity. In wind energy, atmospheric turbulence is assumed to be a stationary random process. For such a framework, examining the statistical properties of wind is relevant only when the process is stationary. Hence, stationarity acts as a crucial criterion for conducting a meaningful analysis of wind data. Another benefit of using the vertical component is that the instrumentation and data collection process may be simplified if only one wind component is required, for instance by using a Doppler wind lidar.

The outline for the thesis is visualized in Fig. 1.1. In chapter 2, the theoretical background are explained. Chapter 3 describes the two data sets used in the thesis, the first obtained from sonic measurements at the FINO1 platform (section 3.1) and the second from lidar measurements from the Lollex field campaign at Rødby harbour (section 3.2). Chapter 4 presents the method for fitting the uniform shear (US) model to data. The results and discussion are divided into three; chapter 5, chapter 6, and chapter 7. The final conclusions and thoughts about future work are presented in chapter 8.

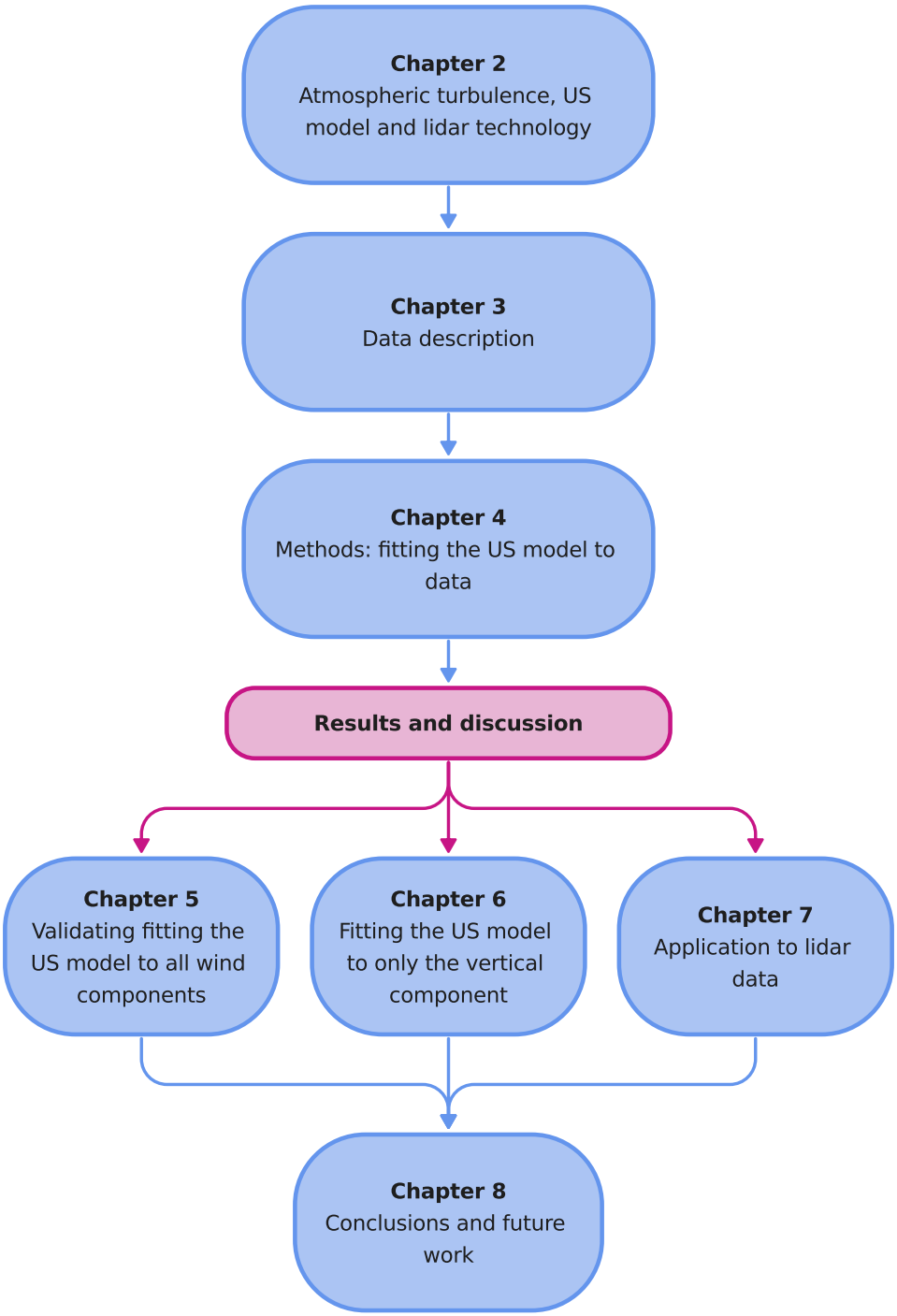

Figure 1.1: Outline for thesis.

Chapter 2

Background

2.1 The atmospheric boundary layer

The atmospheric boundary layer (ABL) is the lowermost part of the atmosphere that is directly influenced by the presence of the surface of the earth. The ABL responds to surface forcings like frictional drag, evaporation and heat transfer within an hour or less (Stull, 1988). The height of the ABL varies between a couple of hundred meters to a few kilometers (Pal & Lee, 2019).

2.1.1 Turbulence

The wind speed can be modelled as a three-dimensional random process with three components; the along-wind u (x-axis), the crosswind v (y-axis) and vertical w (positive z-axis). For each component (u,v,w), the instantaneous velocity can be decomposed in a mean part (denoted by an overline) and a fluctuating (turbulent) part (denoted with a prime). This is called Reynolds decomposition, and is given by (Monin, 1958):

$$u = \overline{u} + u' \tag{2.1}$$

$$v = \overline{v} + v' \tag{2.2}$$

$$w = \overline{w} + w' \tag{2.3}$$

where the overbar denotes the time average.

If the flow is assumed horizontal and stationary, the vertical and lateral velocities are zero in average ($\overline{v} = \overline{w} \approx 0$ m s^{-1}). For structural design, it is

also assumed that the fluctuating part is a stationary and Gaussian random process (Davenport, 1964).

Turbulence can be idealized as consisting of several irregular swirls of motions of different sizes called eddies. Taylor's hypothesis states that turbulence can be considered frozen as it advects past a sensor (Taylor, 1997). Turbulence is not really frozen. However, the simplification holds when the temporal scale for the eddies to evolve is larger than the time required for the eddy to advect past the sensor (Stull, 1988). Taylor's hypothesis makes it possible to convert time series into spatial series. Using Taylor's hypothesis, the wavenumber k can be written as

$$k = \frac{2\pi f}{\overline{u}} \tag{2.4}$$

where $\overline{u}$ is the mean wind speed and f is the frequency.

The relative strength of eddies of different time scales is given by the power spectral density (PSD) of the wind fluctuations (Stull, 1988). The spectral density function of two stationary time series x(t) and y(t) is defined as the Fourier transform of the correlation function R_{xy} between them. The correlation function is called cross-correlation function if the two time series represent different data and autocorrelation function if the two time series are equal. The autospectral and the cross-spectral density functions are given by Bendat & Piersol (1980)

$$S_{xx}(\omega) = \int_{-\infty}^{+\infty} R_{xx}(\tau) e^{-i\omega\tau}\, d\omega \tag{2.5}$$

$$S_{xy}(\omega) = \int_{-\infty}^{+\infty} R_{xy}(\tau) e^{-i\omega\tau}\, d\omega \tag{2.6}$$

where ω is the angular frequency and τ is a time delay. The relation in Eq. (2.5) is called the Wiener-Khinchin theorem (Khintchine, 1934). Equations (2.5) and (2.6) are called two-sided spectra because they are defined over all frequencies. In practice, it is more convenient to work with positive frequencies only (single-sided spectra).

Van der Hoven (1957) found that there is a spectral gap in the horizontal velocity spectra at a period of about 1 hour (Fig. 2.1), due to the lack of physical processes corresponding to these frequencies. The spectral gap separates the turbulent fluctuations from the fluctuations associated with

mesoscale motion. When studying turbulence, the record duration is usually between 10 and 60 minutes, to ensure that the observed fluctuations are caused by turbulence.

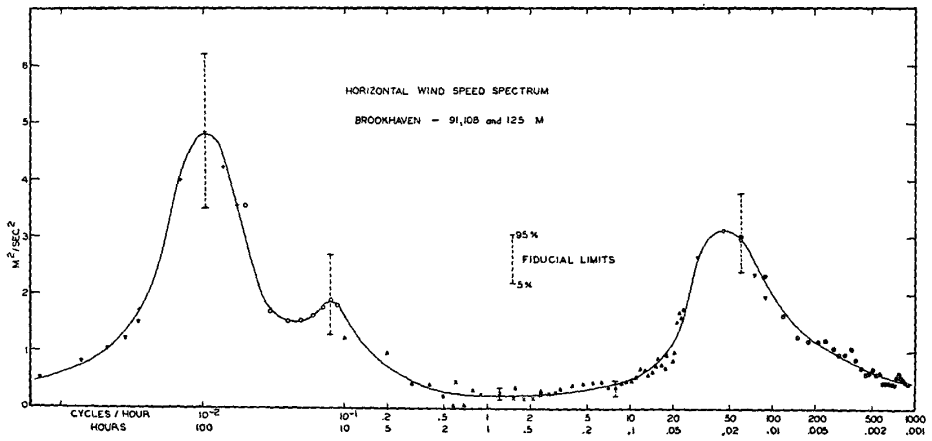

Figure 2.1: Horizontal wind speed spectrum reprinted from Van der Hoven (1957). At about 100 m.

The standard deviation of the wind velocity component can be retrieved using Newland (2012)

$$\sigma_i = \sqrt{\int_0^\infty S_i(f)\,df} \tag{2.7}$$

which is also related to the Wiener-Khinchin theorem (Eq. (2.5)). The standard deviation of the along-wind component (σ_u) governs wind load modeling on wind turbines, which is reflected in the work by Wiley et al. (2023).

The turbulence intensity is a conventional method for quantifying turbulence within the wind energy industry, and is defined by

$$I_i = \frac{\sigma_i}{\overline{u}}. \tag{2.8}$$

The turbulence intensity is for instance used in classification of wind turbines (IEC 61400-1, 2005).

IEC 61400-1 (2005) states that the representative value of the along-wind turbulence standard deviation in the normal turbulence model shall be given by the 90th percentile for a given hub height wind speed. For offshore wind

conditions, the 10-min standard deviation of the along-wind component may be calculated from (IEC 61400-3, 2009)

$$\sigma_{u,\text{10-min}} = \frac{\overline{u}_{\text{hub}}}{\ln(z_{\text{hub}}/z_0)} + 1.28 \times 1.44 \times I_{15} \tag{2.9}$$

where I_{15} is the average value of hub height turbulence intensity at $\overline{u}_{\text{hub}} = 15$ m s^{-1} and the surface roughness parameter z_0 can be derived from the Charnock expression

$$z_0 = \frac{A_C}{g}\left[\frac{\kappa \overline{u}_{\text{hub}}}{\ln(z_{\text{hub}}/z_0)}\right]^2 \tag{2.10}$$

where g is the gravitational acceleration, $\kappa \approx 0.4$ is the von Kármán constant and A_C is Charnock's constant. $A_C = 0.011$ is recommended for open sea (IEC 61400-3, 2009). The 1-hour average turbulence standard deviation can be related to $\sigma_{u,\text{10-min}}$ by

$$\sigma_{u,\text{1-hour}} = \sigma_{1,\text{10-min}} + 0.2 \text{ m s}^{-1}. \tag{2.11}$$

2.1.2 Atmospheric stability

The dynamic stability of the atmosphere is often described using the nondimensional stability parameter

$$\zeta = \frac{z}{L_{MO}} \tag{2.12}$$

where z is the measurement height and L_{MO} is the Obukhov length. The Obukhov length is defined as (Monin & Obukhov, 1954)

$$L_{MO} = \frac{-\overline{\theta_v} u_{*0}^3}{\kappa g (\overline{w'\theta_v'})_0} \tag{2.13}$$

where $\overline{\theta_v}$ is the mean virtual potential temperature, u_{*0} is the friction velocity at the surface, $\kappa \approx 0.4$ is the von Kármán constant, g is the gravitational acceleration and $(\overline{w'\theta_v'})_0$ is the surface flux of virtual potential temperature (Stull, 1988). Monin-Obukhov similarity theory (MOST) assumes that fluxes are constant with height in the surface layer, i.e. $u_{*0} \approx u_*$ and $(\overline{w'\theta_v'})_0 \approx (\overline{w'\theta_v'})$ (Monin & Obukhov, 1954). $\overline{\theta_v}$ is well approximated by

the sonic temperature (Cheynet et al., 2018). Using these assumptions the local Obukhov length

$$L_{MO} = \frac{-\overline{\theta_v} u_*^3}{\kappa g(\overline{w'\theta_v'})} \tag{2.14}$$

can be estimated by a 3D ultrasonic anemometer. The stability of the atmosphere is given by the sign of the stability parameter. $\zeta < 0$ implies dynamically unstable and $\zeta > 0$ implies stable atmosphere. Atmospheric stability may influence wind turbine loads significantly, see e.g. Sathe et al. (2013); Jacobsen & Godvik (2021).

2.2 The uniform shear turbulence model

Mann (1994) presented two models of the spectral tensor of homogeneous, neutral atmospheric surface-layer turbulence. The first one is the uniform shear (US) model without blockage, and the second one includes blockage (US+B). The blockage implies that the flow cannot penetrate the ground, and that the turbulence field is thus affected to a greater extent by the surface than without blockage. However, the US+B model is challenging to implement and Mann (1994) recommend the use of the simpler US model for engineering applications. The US model is the recommended turbulence model in IEC 61400-1 (2005), and will be used in this thesis. The spectral velocity tensor is modeled using three input parameters:

- Γ - the non-dimensional eddy lifetime parameter
- L [m] - the turbulence length scale
- $\alpha\varepsilon^{2/3}$ [$\mathrm{m}^{4/3}\ \mathrm{s}^{-2}$] - the spectral multiplier in the inertial subrange, where α is the spectral Kolmogorov constant and ε is the energy dissipation rate

The US model assumes that the fluctuations are rapidly distorted by a uniform mean velocity shear, and this distortion is modelled using rapid distortion theory (RDT). The initial turbulence conditions are assumed to be isotropic (the same in all directions), and are represented by the isotropic von Kármán tensor. The turbulence will become more and more anisotropic

in time as the eddies are stretched by the shear, which happens on a time period proportional to the wavenumber-dependent eddy lifetime. Therefore, Γ is also commonly called the anisotropy parameter. If Γ is zero, the velocity tensor is fully isotropic and given by the von Kármán tensor. Increasing Γ leads to increase in the along and cross-wind variances while the vertical variance decreases (IEC 61400-1, 2005). Physically, this means that the eddies are stretched in the along-wind direction and tilted relative to the xy-plane. In terms of the velocity spectra, increasing Γ will lower the peak of S_w, slightly shift the peak towards higher wavenumbers and increase the energy at low wavenumbers (Fig. 2.2 upper panel). However, increasing Γ will increase the peak of S_u and shift it towards lower wavenumbers. The model parameter L represents a typical turbulence length scale. Increasing L increases the peak and shifts it towards low wavenumbers for both S_u and S_w (Fig. 2.2 middle panel). The model parameter $\alpha\varepsilon^{2/3}$ can be interpreted as a parameter that scales with the intensity of turbulence. Thus, higher turbulence intensity will be associated with greater values of $\alpha\varepsilon^{2/3}$. Increasing $\alpha\varepsilon^{2/3}$ increases the energy for all wavenumbers without shifting the peak of either S_u or S_w (Fig. 2.2 lower panel).

Even though the US model is developed for neutrally stratified turbulence, it has also been used for non-neutral conditions, where the best parameter values for such situations have been investigated using both onshore (Chougule, 2013; Peña et al., 2010) and offshore measurements (Maré & Mann, 2014).

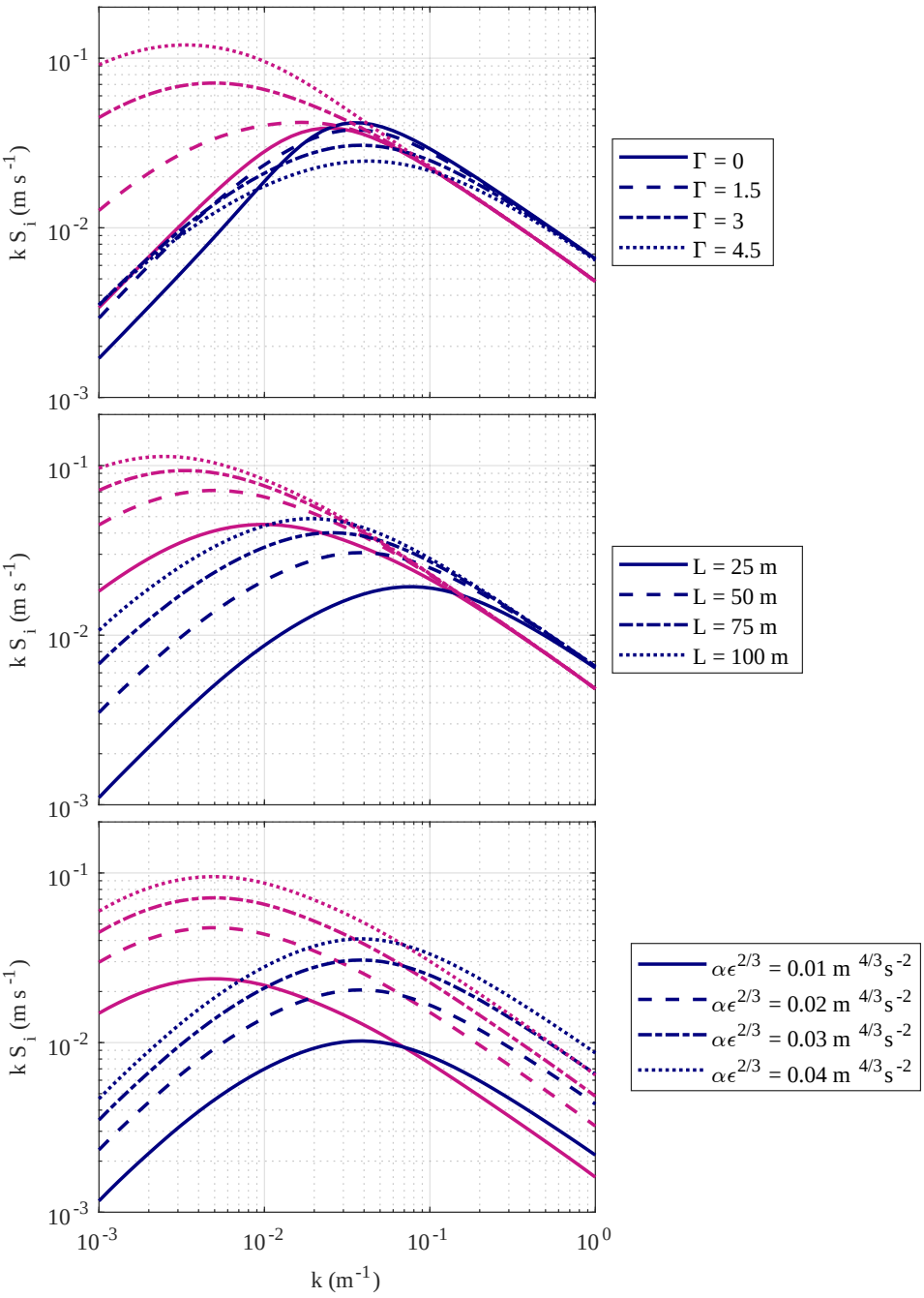

Figure 2.2: Influence of model parameters in the US model on S_u (pink curves) and S_w (dark blue curves). Upper: $L = 50$ m, $\alpha\varepsilon^{2/3} = 0.03$ m^2 s^{-3}. Middle: $\Gamma = 3$, $\alpha\varepsilon^{2/3} = 0.03$ m$^{4/3}$ s^{-2}. Lower: $\Gamma = 3$, $L = 50$ m.

2.3 Lidar

Traditionally, meteorological masts have been used for in-situ turbulence measurements by sonic anemometers. In the North Sea, the tallest masts are typically 100 m tall. Altitudes where large offshore wind turbines operate are generally out of reach of such masts. Doppler lidar (light detecting and ranging) remote sensing is an attractive alternative to the conventional meteorological mast, because of its mobility and absence of need for tall and expensive structures to reach the desired measurement height. Instead, Doppler lidars can be placed at ships, platforms or buoys (Gottschall et al., 2017) and measure the wind speed at several hundred meters above sea level. The basic principles of Doppler lidar technology and challenges due to spatial averaging effects will be presented in the following section.

2.3.1 Basic principles

A Doppler lidar emits laser light with a fixed frequency that are backscattered by atmospheric aerosols. The aerosols are assumed to be moving with the wind speed, and the frequency of the reflected beam (f_r) is therefore shifted relative to the emitted frequency (f_e). The frequency shift is detected by the lidar, from which the line-of-sight (LOS) wind speed (v_{LOS}) can be calculated using (Reuder et al., 2021)

$$f_r = f_e \left(1 + 2\frac{v_{LOS}}{c}\right) \tag{2.15}$$

where c is the speed of light ($3.0 \cdot 10^8$ m s^{-1}). As a single measurement is only a one-dimensional projection of the velocity vector, three linearly independent measurements are needed to reproduce the three dimensional velocity vector.

There are two main categories of Doppler lidar systems; coherent detection lidar and direct detection lidar. A coherent lidar system measures the shift in frequency by comparing the returned signal to a reference signal, while a direct detection system measures the frequency shift by using an optical filter to resolve it into its spectral characteristics (Liu et al., 2019). Coherent lidar systems have several advantages compared to direct lidar systems (Liu et al., 2019). There are two main types of Doppler lidars using a coherent detection system; continuous wave (CW) lidars and pulsed lidars. For a CW lidar, the probe length increases with the square of the distance,

thereby also increasing the spatial averaging effects (Cheynet, 2016). Thus, CW lidars are not relevant for turbulence measurements at long distances. The probe length (and therefore also spatial averaging) of a pulsed lidar is constant along the beam, making it more suitable for long-range measurements. For this reason, only pulsed lidars will be further considered in the thesis.

A pulsed Doppler lidar emits laser light in pulses, and it can therefore measure the wind speed at several distances along the line-of-sight quasi-simultaneously (Puccioni & Iungo, 2021). At any temporal moment, only a limited part of the line-of-sight, a pencil shaped volume known as the probe volume, will be illuminated by the laser beam pulse (Cariou, 2013). Consequently, the detected backscattered signal at a particular time comes from a probe volume at a specific distance from the lidar. The length of each probe volume is the same, but the distance between them (the range gate), can be chosen to achieve a desired overlap. The distance from the lidar to the probe volume can be found from the time difference between the emitted and received pulse (Cariou, 2013).

The head of a Doppler lidar can be either rotating or non-rotating. A Doppler wind lidar profiler does not have a rotating head, thus only allowing vertical profiles of the mean wind speed to be measured using either the doppler beam swinging (DBS) or velocity azimuth display (VAD) mode. A scanning Doppler lidar has a rotating head which makes it possible to have several scanning modes in addition to the DBS or VAD mode; the plan position indicator (PPI), the range height indicator (RHI) and LOS (staring) mode. The scanning modes are characterized by the radial distance, the azimuth angle Φ (defined with respect to the North) and the elevation angle Ψ (defined with respect to a horizontal plane). In this thesis, only measurements from vertical staring mode (Fig. 2.3a) and the 4-beam DBS mode (Fig. 2.3b) from a scanning lidar are utilized, hence only these modes will be explained. Unlike the other modes, staring mode uses only one single beam with fixed elevation and azimuth angle, allowing for a higher sampling frequency. The vertical scanning mode ($\Psi = 90°$) can be used for measurements of vertical velocity variances. Fig. 2.3b shows the 4-beam DBS mode, which uses four LOS measurements spaced equally 90° apart at a fixed elevation angle Ψ. While a lidar profiler can only measure wind speed up to 300 m from the instrument, a scanning Doppler wind lidar can reach distances beyond 1 km.

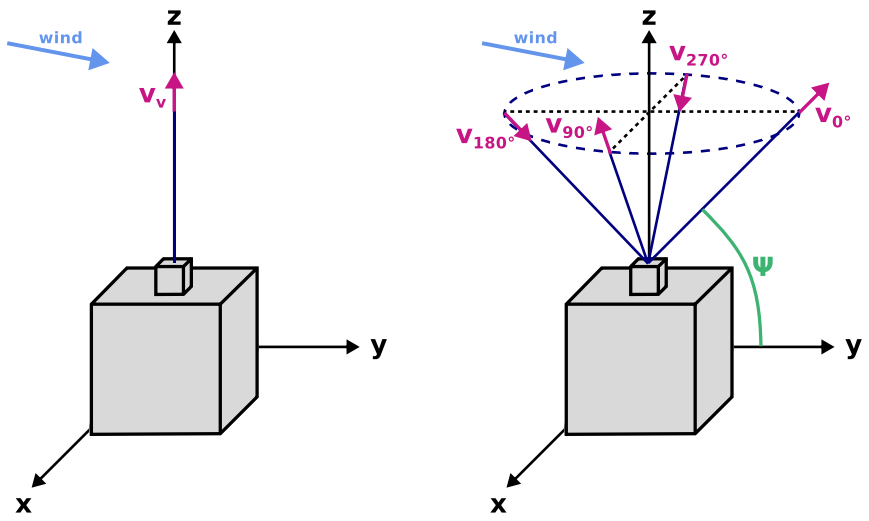

(a) (b)

Figure 2.3: Sketch of (a) vertical staring mode and (b) 4-beam DBS mode inspired by Fig.2 in Reuder et al. (2021).

2.3.2 The spatial averaging effect

The estimated velocity is a spatial average of the true LOS velocity over the probe volume. The spatial averaging effect is generally considered as a convolution of the true LOS wind field with an unknown weighting function ϕ characterizing the energy distribution of the laser pulse along the probe length volume (Puccioni & Iungo, 2021), which can be written as (Mann et al., 2009)

$$v_{LOS}(r) = \int_{-\infty}^{\infty} \phi(s)\mathbf{n}\cdot\mathbf{v}(s+r)\mathbf{n}\,ds \tag{2.16}$$

where $\mathbf{n}$ is a unit vector along the beam, s is the integration variable and r is the focus distance from the lidar, defined as the center of the probe volume of interest. The spatial resolution of a pulsed Doppler lidar depends on the pulse width and the travelled distance of the pulse. The spatial resolution can be improved by shortening the pulse duration, but this needs to be selected carefully to ensure accuracy of the velocity estimation (Liu et al., 2019).

When the laser beam is aligned with the wind direction, Equation (2.16) can be calculated directly using a scalar convolution product (Mann et al.,

2009). The vertical velocity can be measured directly by choosing an elevation angle of 90°, and is thus such a scenario. For a pulsed lidar, the weighting function is commonly expressed as

$$\phi(s) = \begin{cases} \frac{l-|s|}{l^2}, & \text{if } |s| < l \\ 0, & \text{otherwise} \end{cases} \tag{2.17}$$

where l is the length of the probe volume and s is the LOS position within the considered probe volume. The corresponding spectral transfer function, i.e. the Fourier transform of Eq. (2.17), is

$$H(k) = \left[\frac{\sin(kl/2)}{kl/2} \right] \tag{2.18}$$

where k is the wavenumber given by Eq. (2.4). Doppler wind lidar measurements can be considered as the result of the actual wind field undergoing low-pass filtering (Sjöholm et al., 2009). The influence of probe volume length on the vertical wind spectrum is illustrated in Fig. 2.4 where the filtered S_w is obtained by

$$(S_w)_{\text{filtered}} = H^2 S_w. \tag{2.19}$$

Lidars can measure 10 minutes mean wind speed with acceptable accuracy, as proven in several studies by comparing lidar measurements with measurements from anemometers, see for example Cheynet et al. (2017) where measurements by a WindCube 100S prototype is compared to sonic anemometer measurements. For turbulence measurements, the impact of spatial averaging becomes significant, and an effective solution to address this issue is yet to be identified.

Rearranging Eq. (2.19) so that it is solved for S_w is a simplified method to correct for spatial averaging. However, the spectral transfer function is close to zero at high wavenumbers (Fig. 2.5 right panel), leading to "overcorrection" of S_w (Fig. 2.5 left panel). A novel aspect of the thesis, aiming to limit the overcorrection, is to add a regularization method to the deconvolution process by including a constant λ, so that the corrected deconvoluted spectrum is on the form

$$(S_w)_{\text{corrected}} = \frac{(S_w)_{\text{lidar}}}{H^2 + \lambda}. \tag{2.20}$$

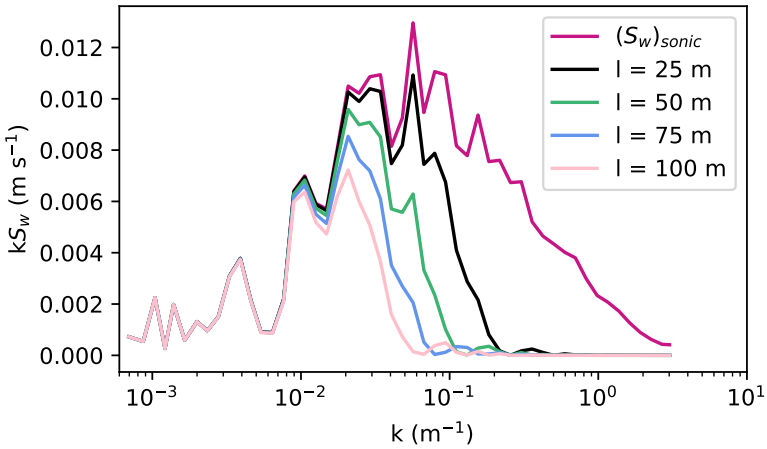

Figure 2.4: The influence of probe volume length (l) on spatial averaging of the vertical wind spectrum (S_w). The pink curve is obtained from measurements by a sonic anemometer at height 81.5 m on the FINO1 platform, and serves here as an unfiltered spectrum.

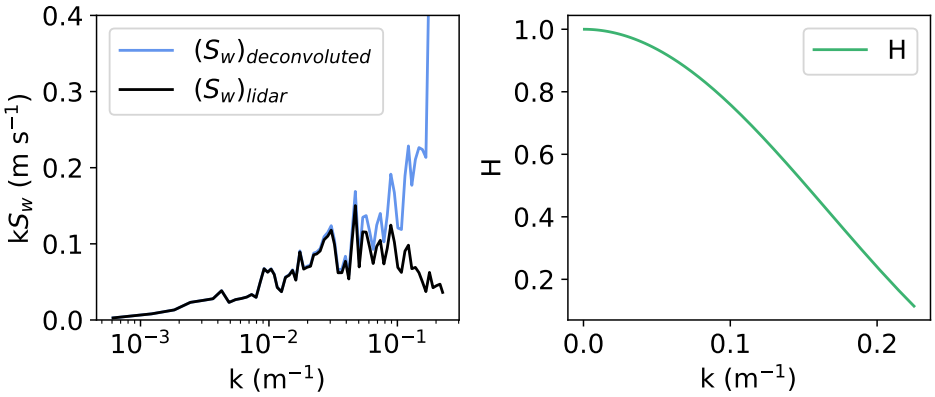

Figure 2.5: Left panel: S_w obtained from measurements at 80 m from a Leosphere WindCube 100S and deconvoluted S_w calculated using the inverse of Eq. (2.19). Right panel: Spectral transfer function H calculated using Eq. (2.18). The probe volume length is 25 m.

2.4 Previous studies

To this author's knowledge there has been no previous studies assessing whether σ_u can be estimated from the along-wind spectrum retrieved from vertical measurements alone. However, the relation between σ_u and σ_w has been investigated by several authors. Solari & Piccardo (2001) found that there are great variability among studies in the ratio σ_w/σ_u based on measurements. In their analysis, the selected experimental measurements showed σ_w/σ_u ranging from 0.40 to 0.64.

A common assumption for estimating σ_u from the vertical component is (IEC 61400-1, 2005)

$$\sigma_u = 2\sigma_w. \tag{2.21}$$

In Engineering Sciences Data Unit (ESDU) (2001) the ratio σ_w/σ_u for neutral atmosphere is given by

$$\frac{\sigma_w}{\sigma_u} = 1 - 0.45\cos^4\left(\frac{\pi}{2}\frac{z}{h}\right) \tag{2.22}$$

where z is the height and h is the ABL depth. This relation is based on simultaneous measurements of σ_u and σ_w, which states that the ratio remain essentially constant regardless of the terrain characteristics. h can be estimated using

$$h = \frac{u_*}{6f} \tag{2.23}$$

where f is the Coriolis parameter.

2.5 Key assumptions

In wind energy, atmospheric turbulence is assumed to be a stationary random process. In the marine atmospheric boundary layer around 20% to 30% of wind conditions may be non-stationary (Cheynet et al., 2018), but the framework of non-stationary wind is beyond the scope of this thesis. Turbulence is assumed to be a Gaussian ergodic random process, which means that the time average operator is a good approximation of the ensemble average. Gaussian turbulence implies that it can described adequately by only focusing on the second-order turbulence characteristics (the mean and variance/standard deviation) (Davenport, 1964). In this thesis, vertical profiles of σ_u is of interest, so the turbulence is not assumed to be homogeneous.

Chapter 3

Data

3.1 FINO1

Reference data were collected at the FINO1 platform located in the North Sea (Fig. 3.1) during 2007 and 2008. The 20 m high jacket platform has a steel square lattice tower of 81 m height and linearly decreasing width from 3.5 m at its base to 1.4 m at its top (Fig. 3.2). The reference data were collected from a Gill R3-50 sonic anemometer at 81.5 m a.s.l. with a sampling frequency of 10 Hz. The sonic anemometer is mounted with an azimuth of 311° on a boom of length 3 m on the north-west side of the mast on a corner of the rectangular lattice. More information about the location and instrumentation can be found in Cheynet et al. (2018).

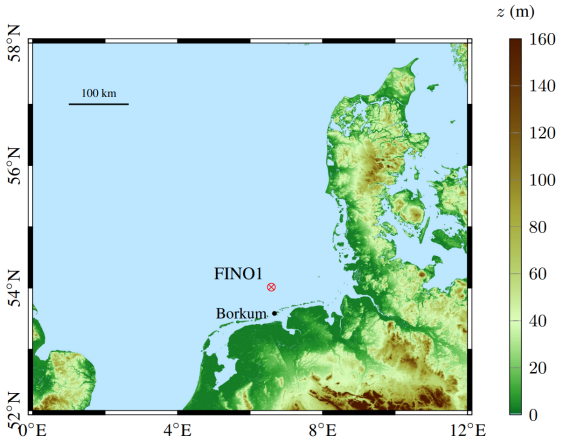

Figure 3.1: The location of the FINO1 platform (Cheynet et al., 2018).

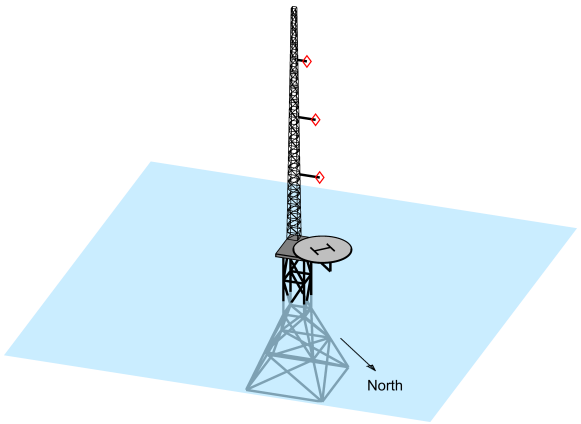

Figure 3.2: Sketch of the FINO1 platform (Cheynet et al., 2018).

The data set had undergone some data processing before being provided to this author. To avoid disturbance from the tower, only wind directions from 190° to 359° were considered. Wind speeds were filtered from 5 to 28 m s^{-1} to be consistent with wind speeds at which turbines operate, and hours with turbulence intensity higher than 0.2 or below 0.001 were disregarded, as these are considered abnormal fluctuations. PSD for each velocity component were computed using the periodogram with a Hamming window. A stationarity test was performed, and only data passing this test are considered in this thesis. These processed wind spectra were assigned to the author for further analysis.

As data from high altitudes are of interest of this thesis, only data from 81.5 m height were considered. A quality check of the data, aiming to eliminate samples displaying unrealistic PSD in the inertial subrange, was performed. This were done by fitting a pointed model based on Olesen et al. (1984) to the vertical velocity spectra using a least-square method. The pointed model is on the form

$$fS_w = \frac{Af}{1 + Bf^C} \tag{3.1}$$

where A, B and C are constants to be determined. C is the slope on a log-log graph when the spectrum is plotted against frequency. Theoretically, the slope should be equal to 5/3 in the inertial subrange. Two criteria were created for the slope and the root mean square error (RMSE) calculated from fS_w from the data set and the pointed model, and only samples satisfying

one of these were kept in the analysis. The criteria were: 1) slope > 1.1 and RMSE < 0.03 m^{2}s^{-2} or 2) slope > 1.5 and RMSE < 0.1 m^{2}s^{-2}. In other words, the spectrum might meet the criteria despite exhibiting unfavorable slope if its RMSE is low, or if it demonstrates a favorable slope despite having a comparatively higher RMSE. Samples not satisfying the criteria were assumed to have unrealistic PSD in the inertial subrange. A spectrum that satisfies both criteria is visualized in Fig. 3.3. The number of samples left after removing the samples not satisfying either of the criteria are shown in Table 3.1. The stability is classified in consistency with Cheynet et al. (2018). inpaint_nans (D'Errico, 2012) versions of the original sonic data have been used. This function aims to non-linearly interpolate over data marked as NaNs (Not a Number).

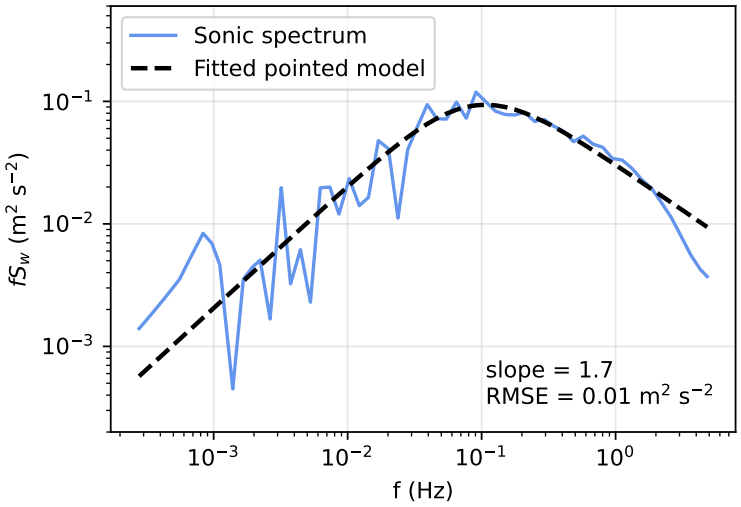

Figure 3.3: A pointed model fitted to sonic measurement of the vertical wind spectrum. The measurements are taken by a sonic anemometer at 81.5 height at the FINO1 platform in January 2008.

Table 3.1: The number of samples before and after removing bad S_w measurements based on fitting the vertical wind spectrum to a pointed model. The samples are collected by a sonic anemometer at FINO1 at 81.5 m during 2007 and 2008.

Stability	Before	After
Stable ($\zeta \geq 0.1$)	1942	1871
Neutral ($-0.1 < \zeta < 0.1$)	2074	2007
Unstable ($\zeta \leq -0.1$)	2934	2787

3.2 Lollex field campaign

The lidar measurements were taken during the Lollex field campaign performed as part of the H2020 MSCA-ITN Train2Wind in Denmark. From October to December 2022 a scanning wind lidar system, using the Leosphere WindCube 100S, was operating on shore at the RWE base in Rødby harbour (Fig. 3.4). The lidar operated in an alternating configuration with 25 minutes of vertical staring mode (Fig. 2.3a) to measure vertical velocity variances, followed by 5 minutes of DBS mode (Fig. 2.3b) for wind profiling. Velocity data from the lidar were collected with a sampling frequency of 1 Hz. The range gate length was 25 m with an overlap of 60% resulting in an along-beam spatial resolution of 10 m. The measurement heights ranged from 50 m to 2630 m above the surface.

Figure 3.4: Leosphere WindCube 100S placed at Rødby harbour (photo courtesy of Shokoufeh Malekmohammadi).

Chapter 4

Method for fitting the US model

The US model was fitted to velocity spectra from the FINO1 platform for two different cases; 1) all velocity spectra (S_u, S_v, S_w and S_{uw}) were known and 2) only the vertical spectrum (S_w) was known. The fitting function fitMann.m (Cheynet, 2022) uses a least-square method to fit the US model to data, estimating the model parameters Γ, L and $\alpha\varepsilon^{2/3}$. In addition to wind spectra, the fitting function requires single-sided wavenumbers in the along-wind direction. For both cases, this required information about the horizontal mean wind speed ($\overline{u}$), to convert the frequency from the spectral analysis to wavenumber using Eq. (2.4). The fitting function also has some optional inputs. The initial guess used in the fitting was $\Gamma = 3$, $L = 40$ m and $\alpha\varepsilon^{2/3} = 0.1$ m$^{4/3}$ s^{-2}, which was chosen after testing the fitting function on data from FINO1. The initial guess can affect the convergence of the fitting algorithm. Using MultiStart in Matlab was considered unnecessary since the initial guess was satisfactory in most cases, and its implementation would come at the expense of the effectiveness of the method. Tolerances for the fitting procedure (denoted $tolX$ and $tolFun$ in the fitting function) were also used as inputs, and different values were tested. Tolerances are used to ensure that convergence of the fitting algorithm is achieved, thus a smaller tolerance is usually recommended but at the cost on heavier computational cost. The parameter limits in the fitting function were adjusted based on parameter values obtained in fittings to the FINO1 data, see Table 4.1.

Several fittings were performed with different wavenumber intervals and iteration tolerances to decide which gave the best fitting results. For each fitting, a minimum k value (k_{min}) and a maximum k value (k_{max}) were

Table 4.1: Parameter limits used initially in the fitting function.

Model parameter	Initial minimum	Initial max	Adjusted minimum	Adjusted max
Γ	0	6	0.5	4.5
L [m]	1	100	1	300
$\alpha\varepsilon^{2/3}$ [$m^{4/3}$ s^{-2}]	0	2	0	2

chosen, and a new logarithmically spaced k array was created based on these chosen endpoints. The velocity spectra obtained from spectral analysis of the sonic data (later denoted with "**sonic**" as subscript) were interpolated over this new k array, and the interpolated versions were used in the fittings. The interpolated spectra and the resulting σ_u obtained from the interpolated along-wind spectrum will be referred to using the subscript "**targ**" (short for "target"). The estimated model parameters obtained from fitting the US model to the target spectra were used to generate new wind spectra using the function MannTurb.m (Cheynet, 2022). The generated spectra will be referred to using the subscript "**Mann**". The quality of the fittings were checked by comparing the standard deviation of u (Eq. (2.7)) calculated from $(S_u)_{\text{targ}}$ and $(S_u)_{\text{Mann}}$

$$(\sigma_u)_{\text{targ}} = \sqrt{\int_{f_{\min}}^{f_{\max}} (S_u)_{\text{targ}}\, df} \tag{4.1}$$

$$(\sigma_u)_{\text{Mann}} = \sqrt{\int_{f_{\min}}^{f_{\max}} (S_u)_{\text{Mann}}\, df} \tag{4.2}$$

where $f_{\min}$ and $f_{\max}$ are calculated from the chosen $k_{\min}$ and $k_{\max}$ in the fitting using Eq. (2.4). A visualization of the integrals are shown in Fig. 4.1, where the darkest blue area in the upper panel corresponds to the integral in Eq. (4.1) and the darkest pink area in the lower panel correspond to the integral in Eq. (4.2). $(\sigma_u)_{\text{targ}}$ and $(\sigma_u)_{\text{Mann}}$ are not realistic representations of the actual σ_u, because they are calculated over a limited f interval, giving a smaller value than the actual σ_u (which we are interested in when calculated wind loads). However, the numbers are helpful in checking the quality of the fitting.

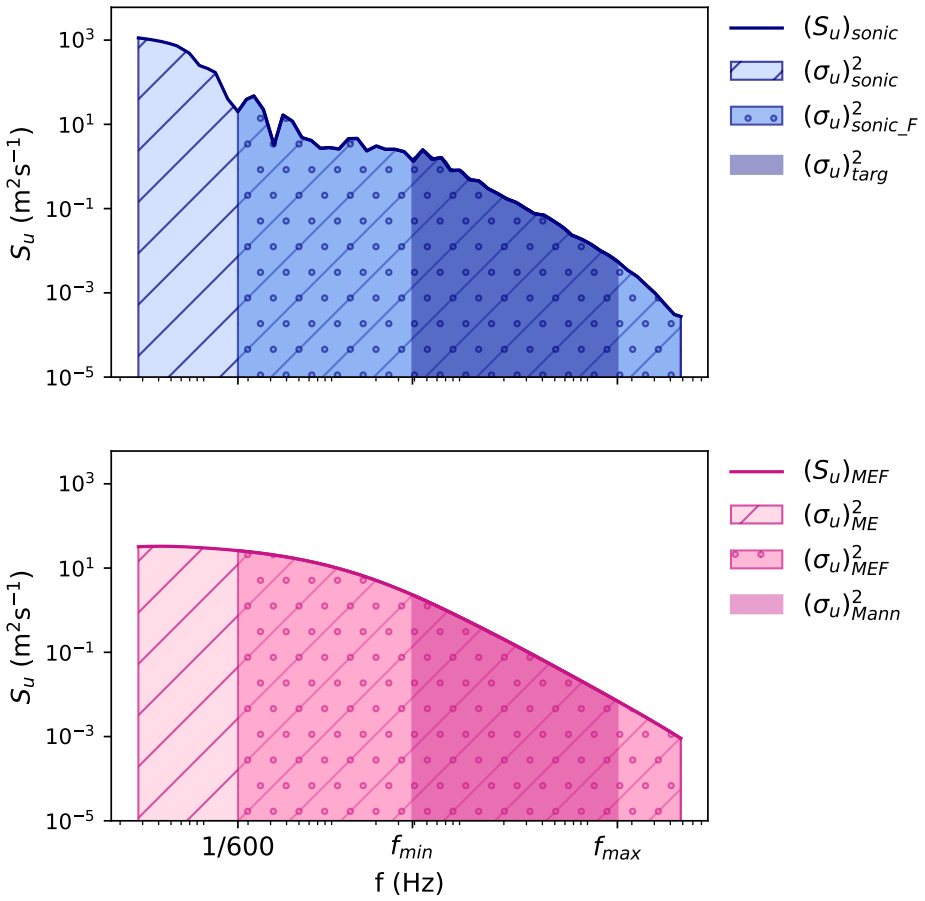

Figure 4.1: Upper panel: visualization of the integrals in Eq. (4.1), Eq. (4.3) and Eq. (4.5). Lower panel: visualization of the integrals in Eq. (4.2), Eq. (4.4) and Eq. (4.6).

The estimated parameters obtained in fittings with a limited k interval, were used to generate spectra over the original k interval from the spectral analysis of the sonic data. These extended spectra generated by the model parameters will be referred to with subscript "**ME**", which is short for "Mann Extended". The quality of the extended results were checked by comparing σ_u calculated from $(S_u)_{\text{sonic}}$ and $(S_u)_{\text{ME}}$

$$(\sigma_u)_{\text{sonic}} = \sqrt{\int_{(f)_{\text{sonic}}} (S_u)_{\text{sonic}}\, df} \tag{4.3}$$

$$(\sigma_u)_{\mathrm{ME}} = \sqrt{\int_{(f)_{\mathrm{ME}}} (S_u)_{\mathrm{ME}}\, df} \tag{4.4}$$

The US model does not simulate mesoscale motion or very large eddies generated by buoyancy, so its ability to model low-frequency turbulence with a period beyond 10 minutes is limited. To be consistent with IEC guidelines, the data were then filtered by only including frequencies larger than 1/600 Hz, which corresponds to a time period of 10 minutes. This will be denoted "**F**" for "filtered". The quality of the results only including frequencies above 1/600 Hz were checked by comparing the σ_u (Eq. (2.7)) calculated from $(S_u)_{\mathrm{sonic\_F}}$ and $(S_u)_{\mathrm{MEF}}$ for frequencies above 1/600 Hz

$$(\sigma_u)_{\mathrm{sonic\_F}} = \sqrt{\int_{(f)_{\mathrm{sonic}} > \frac{1}{600}\ \mathrm{Hz}} (S_u)_{\mathrm{sonic\_F}}\, df} \tag{4.5}$$

$$(\sigma_u)_{\mathrm{MEF}} = \sqrt{\int_{(f)_{\mathrm{ME}} > \frac{1}{600}\ \mathrm{Hz}} (S_u)_{\mathrm{MEF}}\, df} \tag{4.6}$$

The (extended and) filtered results were compared to Eq. (2.21) and Eq. (2.9). A list explaining the different name definitions is found in Table 4.2.

Table 4.2: Name definitions used in the thesis.

Sonic data	
$(S_i)_{\text{sonic}}$	Spectrum obtained from spectral analysis of sonic data.
$(f)_{\text{sonic}}$	The corresponding frequencies from the spectral analysis.
$(k)_{\text{sonic}}$	Calculated from $(f)_{\text{sonic}}$ using Eq. (2.4).
$(\sigma_i)_{\text{sonic}}$	Square root of $(S_i)_{\text{sonic}}$ integrated over $(f)_{\text{sonic}}$. Calculated using Eq. (4.3).
$(S_i)_{\text{sonic\_F}}$	Equal to $(S_i)_{\text{sonic}}$ for $(f)_{\text{sonic}} > 1/600$ Hz
$(\sigma_i)_{\text{sonic\_F}}$	Square root of $(S_i)_{\text{sonic\_F}}$ integrated over $(f)_{\text{sonic}} > \frac{1}{600}$ Hz. Calculated using Eq. (4.5).
Target spectra	
$(k)_{\text{targ}}$	A new logarithmically spaced k array created from the chosen k_{min} and k_{max} in the fitting.
$(f)_{\text{targ}}$	Calculated from $(k)_{\text{targ}}$ using Eq. (2.4).
$(S_i)_{\text{targ}}$	$(S_i)_{\text{sonic}}$ has been interpolated over $(k)_{\text{targ}}$. This is the spectra that the US model is fitted to.
$(\sigma_i)_{\text{targ}}$	Square root of $(S_i)_{\text{targ}}$ integrated over $(f)_{\text{targ}}$. Calculated using Eq. (4.1).
Fitting results	
$(S_i)_{\text{Mann}}$	Spectra generated from the estimated parameters obtained in the fitting with the limited k interval.
$(k)_{\text{Mann}}$	Obtained from MannTurb.m when generating $(S_i)_{\text{Mann}}$.
$(f)_{\text{Mann}}$	Calculated from $(k)_{\text{Mann}}$ using Eq. (2.4).
$(\sigma_i)_{\text{Mann}}$	Square root of $(S_i)_{\text{Mann}}$ integrated over $(f)_{\text{Mann}}$. Calculated using Eq. (4.2).
Extended fitting results	
$(S_i)_{\text{ME}}$	The estimated parameters obtained in fitting with the limited k interval have been used to generate spectra for a k interval matching $(k)_{\text{sonic}}$.
$(k)_{\text{ME}}$	Obtained from MannTurb.m when generating $(S_i)_{\text{ME}}$.
$(f)_{\text{ME}}$	Calculated from $(k)_{\text{ME}}$ using Eq. (2.4).
$(\sigma_i)_{\text{ME}}$	Square root of $(S_i)_{\text{ME}}$ integrated over $(f)_{\text{ME}}$. Calculated using Eq. (4.4).
$(S_i)_{\text{MEF}}$	Equal to $(S_i)_{\text{ME}}$ for $(f)_{\text{ME}} > \frac{1}{600}$ Hz
$(\sigma_i)_{\text{MEF}}$	Square root of $(S_i)_{\text{MEF}}$ integrated over $(f)_{\text{ME}} > \frac{1}{600}$ Hz. Calculated using Eq. (4.6).

Chapter 5

Validating the US model fitted to all wind components

5.1 Limited wavenumber interval

Fitting the US model to all velocity components works relatively well for all the tested k intervals and tolerances, at least when comparing the resulting $(\sigma_u)_{\text{Mann}}$ and $(\sigma_u)_{\text{targ}}$. Spectral values with $k_{\max} > 1.0$ m^{-1} were not tested in case the spectra had undergone a low-pass filter to avoid aliasing (noise at high frequencies) before being handed to the author. Fig. 5.1 compares $(\sigma_u)_{\text{Mann}}$ and $(\sigma_u)_{\text{targ}}$ obtained from fittings to data from January 2008 for different combinations of k intervals and tolerances. The vertically aligned panels share the same k interval but have different iteration tolerances, 10^{-3} for the upper panels and 10^{-4} for the lower panels. Except for a few outliers, the dots follow nicely a $y = x$ line for all stabilities, resulting in relatively low RMSE values for all six situations. This indicates that the US model can be used for all stability conditions, which is consistent with prior research (Chougule, 2013; Peña et al., 2010; Maré & Mann, 2014). Choosing iteration tolerances of 10^{-3} or 10^{-4} made no difference to the results in terms of the RMSE.

The outliers in the left panels of Fig. 5.1 are associated with $(S_u)_{\text{targ}}$ and $(S_w)_{\text{targ}}$ that do not look like typical wind spectra, an example of this is visualized in Fig. 5.2a. However, the vertical wind spectrum passes the slope and RMSE criteria defined in section 3.1 for them to be kept in the analysis. The slope of the pointed model fitted to S_w from the data set is 1.2, which

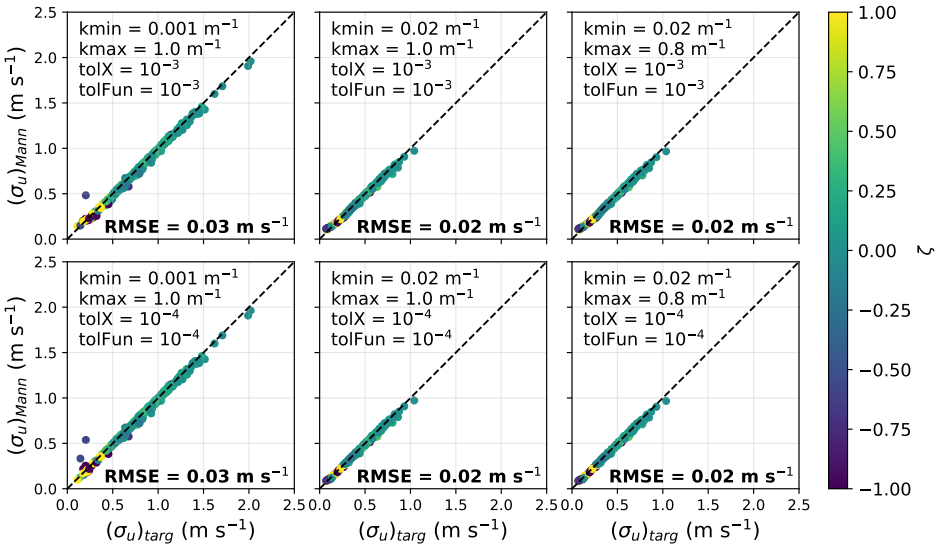

Figure 5.1: Comparison of $(\sigma_u)_{\text{Mann}}$ and $(\sigma_u)_{\text{targ}}$ obtained from fitting the US model to all velocity components using different k_{min}, k_{max} and tolerances. The figure is based on 381 samples obtained from measurements at 81.5 m at FINO1 in January 2008. The dashed line shows $y = x$.

is much less than the theoretical value of 5/3. However, the RMSE value of the data and the pointed model is only 0.002 m^{2}s^{-2}, thereby ensuring fulfillment of the first criterion defined in section 3.1 for a vertical spectrum showing realistic behavior in the inertial subrange. A successful criteria definition that eliminated all poor spectra was not achieved, so the method for filtering out poor S_w samples is not fully adequate. Alternatively, each spectrum could have been manually inspected, but this would have been too time-consuming given the large number of samples. It is possible that the stationarity test conducted prior to this author obtaining the data set was not reliable, resulting in some of the samples being non-stationary. This could potentially lead to unusual PSD at low frequencies. The US model overestimates both S_u and S_w when $0.001\ \text{m}^{-1} \leq k \leq 1.0\ \text{m}^{-1}$ in the fitting (left panels of Fig. 5.2a). For narrower k intervals (middle and right panels) the US model fit better, resulting in no outliers in the middle and left panels of Fig. 5.1. The good correspondence between $(\sigma_u)_{\text{Mann}}$ and $(\sigma_u)_{\text{targ}}$ are probably because the PSD values are very low in these k intervals, resulting in low deviation despite the dissimilar appearance of the graphs in the middle

and right panels of Fig. 5.2a. To ensure that the poor fit in Fig. 5.2a was not due to poor initial guess of the model parameters, several other initial guesses were tested, without any of them resulting in a better fit.

A sample that has a good fit in each k interval is shown in Fig. 5.2b, where the mean wind speed is high ($\overline{u} = 21.3$ m s^{-1}) and the atmosphere is stable ($\zeta = 0.2$). $(\sigma_u)_{\text{Mann}}$ is equal to its target value in each situation (see lower center of each panel). The slope of the pointed model fitted to the vertical wind spectrum from the data set is 1.7 (which is the desired value), and the RMSE of the measured S_w and the pointed model is 0.02 m^{2}s^{-2}. Note that the peak of S_w lies in all of the tested k intervals, but the peak of S_u is at lower wavenumbers, only captured by the interval $0.001 \text{ m s}^{-1} \leq k \leq 1.0 \text{ m s}^{-1}$.

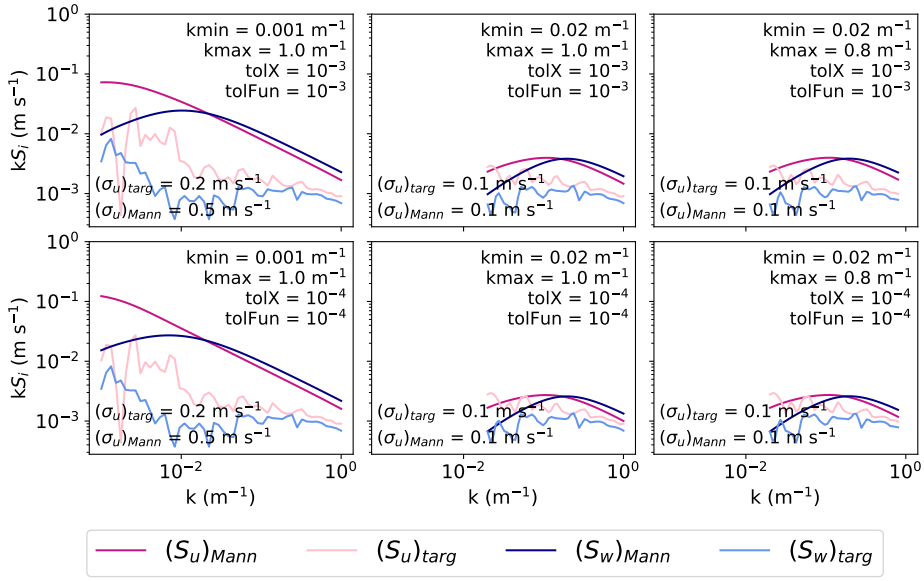

(a) Untypical target wind spectra with $\overline{u} = 7.9$ m s^{-1} and $\zeta = -0.6$ (unstable).

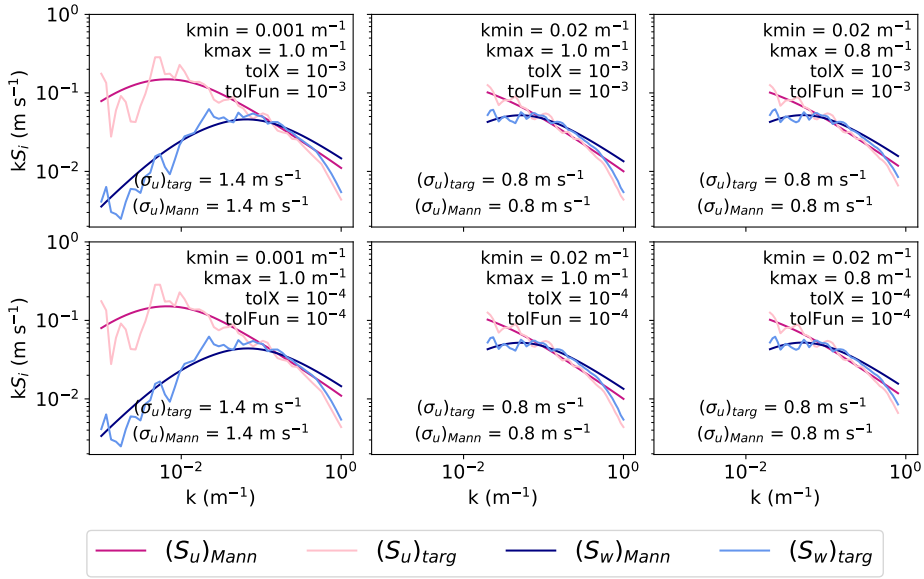

(b) Typical target spectra with $\overline{u} = 21.3$ m s^{-1} and $\zeta = 0.2$ (stable).

Figure 5.2: The US model fitted to all wind components for two different samples using different k_{min}, k_{max} and tolerances. The samples are collected in January 2008 at 81.5 m at FINO1.

5.2 Extended wavenumber interval

Extending the k interval by generating along-wind spectra for an interval corresponding to $(k)_{\text{sonic}}$ from parameters obtained from fittings with a limited k interval, does not work well when including all frequencies, see Fig. A.1. This is probably because the US model cannot model large eddies (small wavenumbers) from non-turbulent motion, as illustrated in Fig. 5.3. Mathematically, this can be explained because the wind spectra in the US model are unimodal functions. This is also the reason why k_{min} below 0.001 m^{-1} were not tested in fittings.

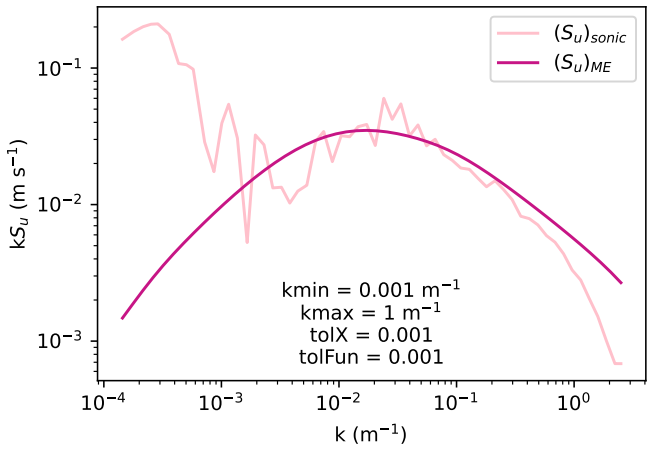

Figure 5.3: Along-wind spectrum obtained from sonic measurements from January 2008 and fitting the US model to the measurements when all wind components were known. The fitting was performed for the interval 0.001 $\text{m}^{-1} \leq k \leq 1.0\ \text{m}^{-1}$. $\zeta = 0.05$, $\overline{u} = 12.1\ \text{m s}^{-1}$

When only considering frequencies larger than 1/600 Hz, the results are much better. The correspondence between $(\sigma_u)_{\text{MEF}}$ and $(\sigma_u)_{\text{sonic\_F}}$ depends on the range of the fitted k interval (Fig. 5.4). A broad k interval in the fitting leads to better σ_u correspondence than a narrower k, which is different from when only the k interval used in the fitting were considered. As for the limited k interval, when looking at one particular interval, the RMSE remains unchanged for both tolerances. Tolerances of 10^{-3} may be favorable due to the lower iteration time and decreased computational costs. However, it is also more risky due to possible local minima. For January 2008, the broad

k interval 0.001 $\mathrm{m}^{-1} \leq k \leq 1.0\ \mathrm{m}^{-1}$ gives the lowest RMSE (0.04 $\mathrm{m\ s}^{-1}$ for both tolerances). Observing plots of the wind spectra, it appears that the peak of S_w typically occurs above $k = 0.02\ \mathrm{m}^{-1}$, making the peak of S_w visible in all the considered k intervals in Fig. 5.4. The peak of S_u typically occurs at lower wavenumbers, posing a challenge in accurately estimating S_u when $k_{\min} = 0.02\ \mathrm{m}^{-1}$. This is because the peak falls outside the fitting interval, which might result in poor estimation of σ_u. Some poor fitting might be due to insufficient initial guess of the model parameters, which is equal in all fittings. In this thesis, two different combinations of k intervals and tolerances will be analysed in detail, the broad k interval with $k_{\min} = 0.001\ \mathrm{m}^{-1}$, $k_{\max} = 1.0\ \mathrm{m}^{-1}$ and $tolX = tolFun = 10^{-3}$ (upper left panel of Fig. 5.4) and the narrow k interval with $k_{\min} = 0.02\ \mathrm{m}^{-1}$, $k_{\max} = 0.8\ \mathrm{m}^{-1}$ and $tolX = tolFun = 10^{-4}$ (lower right panel of Fig. 5.4). These two fitting inputs are chosen based on the first one giving very good results when all velocity components are known and the second giving rather good results when only S_w is known (which will be seen in chapter 6).

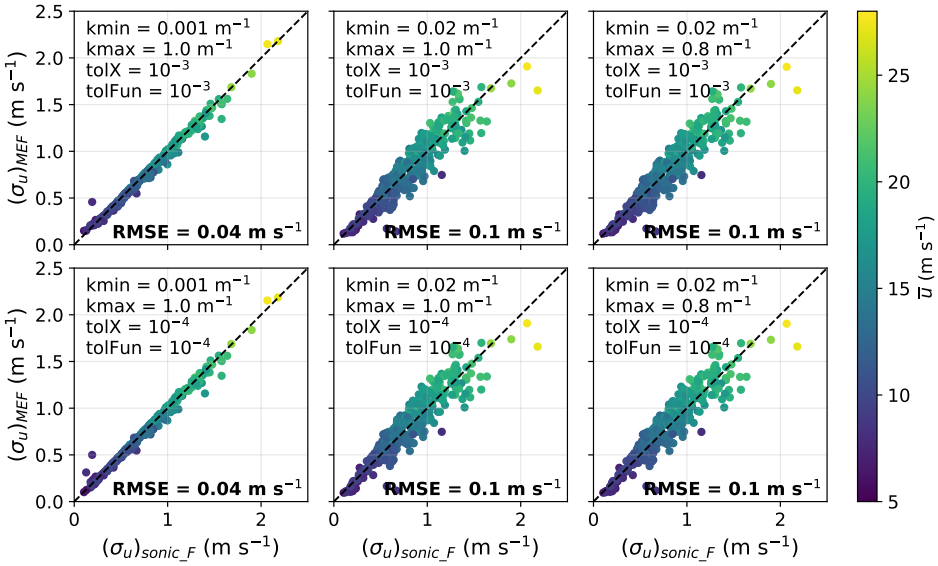

Figure 5.4: Comparison of $(\sigma_u)_{\mathrm{MEF}}$ and $(\sigma_u)_{\mathrm{sonic\_F}}$ obtained from fitting the US model to all velocity components using different $k_{\min}$, $k_{\max}$ and tolerances. The figure is based on 381 samples obtained from measurements at 81.5 m at FINO1 in January 2008. The dashed line shows $y = x$.

So far, only data from January 2008 (381 samples) have been included. When including all months in 2007 and 2008 (6665 samples), $(\sigma_u)_{\text{MEF}}$ and $(\sigma_u)_{\text{sonic\_F}}$ still match well for $0.001\ \text{m}^{-1} \leq k \leq 1.0\ \text{m}^{-1}$ and iteration tolerances 10^{-3} (Fig. 5.5a), with RMSE values of 0.03 m s^{-1}, 0.05 m s^{-1} and 0.04 m s^{-1} for stable, neutral and unstable atmosphere. Using tolerances of 10^{-3} or 10^{-4} lead to the same RMSE (when using only one significant digit), see Fig. B.1a in appendix B for tolerances 10^{-4}. Due to the reduced iteration time, tolerances of 10^{-3} for this k interval will be used. The density plots of $(\sigma_u)_{\text{MEF}}$ vs $(\sigma_u)_{\text{sonic\_F}}$ (corresponding to Fig. 5.5a) follows very good the $y = x$ line (Fig. 5.5b).

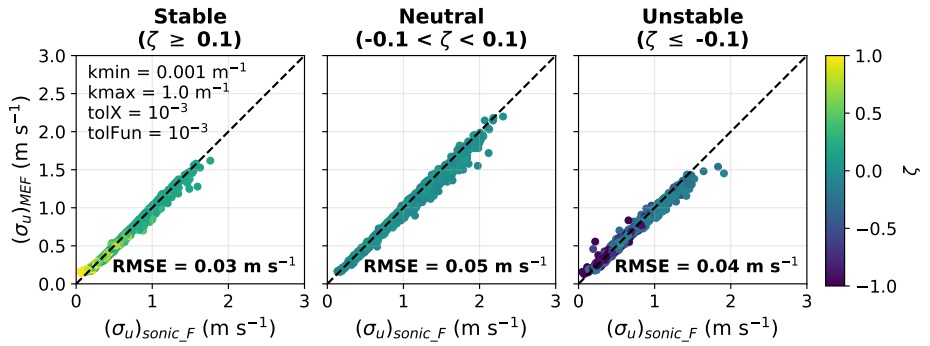

(a) Scatter plot with colors showing stability.

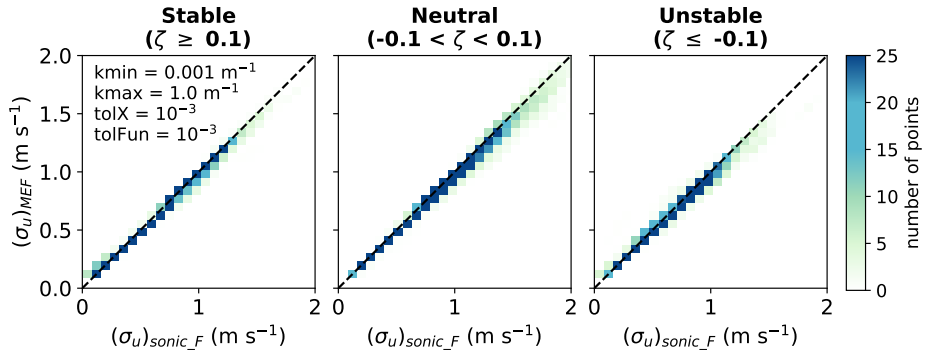

(b) Density plot with colors showing number of points.

Figure 5.5: $(\sigma_u)_{\text{sonic\_F}}$ obtained from Eq. (2.7) for frequencies above 1/600 Hz. $(\sigma_u)_{\text{MEF}}$ obtained from fitting the US model to data of all wind components, calculated using Eq. (4.6). The figure is based on 1871 stable, 2007 neutral and 2787 unstable samples collected by sonic anemometer at height 81.5 m at FINO1 during 2007 and 2008. The dashed line shows $y = x$.

Fittings with $0.02\ \mathrm{m}^{-1} \leq k \leq 0.8\ \mathrm{m}^{-1}$, which gave very good match between $(\sigma_u)_{\mathrm{Mann}}$ and $(\sigma_u)_{\mathrm{targ}}$ (Fig. 5.1 right panels), give large spread and RMSE when comparing $(\sigma_u)_{\mathrm{MEF}}$ and $(\sigma_u)_{\mathrm{sonic\_F}}$ for both tolerances (see Fig. 5.6a for tolerances 10^{-4}). The choice of tolerances make a small difference to the RMSE value for the k interval $0.02\ \mathrm{m}^{-1} \leq k \leq 0.8\ \mathrm{m}^{-1}$. For stable and neutral conditions, the two tolerances result in the same RMSE. For unstable situations, tolerances of 10^{-4} result in RMSE of $0.1\ \mathrm{m\,s}^{-1}$ while 10^{-3} give RMSE of $0.2\ \mathrm{m\,s}^{-1}$ (see Fig. B.2a in appendix B for tolerances 10^{-3}). Thus, for the k interval $0.02\ \mathrm{m}^{-1} \leq k \leq 0.8\ \mathrm{m}^{-1}$, tolerances of 10^{-4} are analysed further. For this fitting option, the majority of the points lie below $y = x$ for neutral and unstable atmosphere (Fig. 5.6b). In other words, the US model has a tendency to underestimate σ_u for $0.02\ \mathrm{m}^{-1} \leq k \leq 0.8\ \mathrm{m}^{-1}$ and tolerances 10^{-4}.

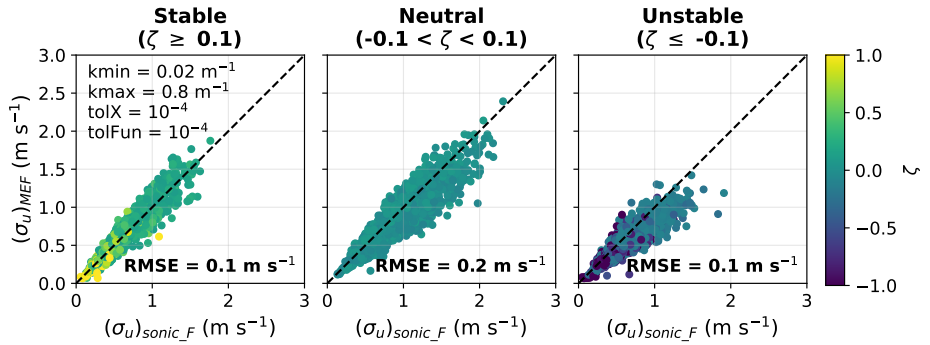

(a) Scatter plot with colors showing stability.

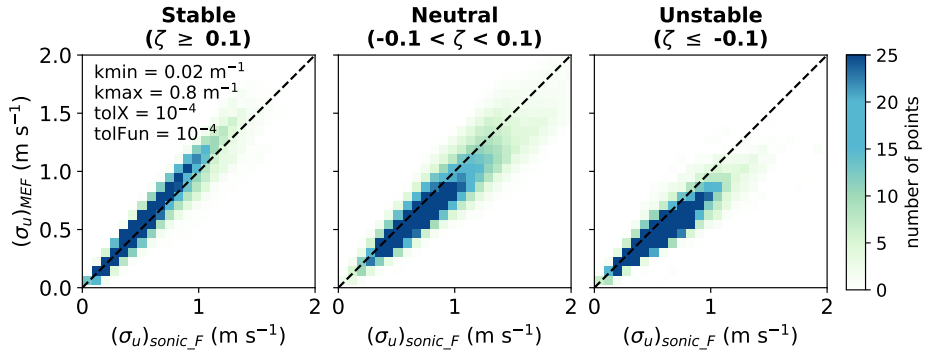

(b) Density plot with colors showing number of points.

Figure 5.6: $(\sigma_u)_{\text{sonic\_F}}$ obtained from Eq. (2.7) for frequencies above 1/600 Hz. $(\sigma_u)_{\text{MEF}}$ obtained from fitting the US model to data of all wind components, calculated using Eq. (4.6). The figure is based on 1871 stable, 2007 neutral and 2787 unstable samples collected by sonic anemometer at height 81.5 m at FINO1 during 2007 and 2008. The dashed line shows $y = x$.

5.3 Model parameters

The estimated model parameter values obtained from fittings with $k_{\text{min}} = 0.001$ m^{-1}, $k_{\text{max}} = 1$ m^{-1} and tolerances 10^{-3} are considered reliable due to the strong σ_u correspondence for frequencies larger than 1/600 Hz (Fig. 5.5a and Fig. 5.5b). In contrast to Γ and $\alpha\varepsilon^{2/3}$, the mean value of L vary significantly with stability (Table 5.1), with relatively small turbulence length scale for stable atmosphere and large for unstable. The standard deviation of each parameter is large compared to its mean value, meaning that there is large variation in parameter values for each stability condition.

Table 5.1: Mean values and standard deviation of the model parameters after stability obtained from fittings with all velocity components known and $k_{\min} = 0.001$ m^{-1}, $k_{\max} = 1$ m^{-1} and tolerances 10^{-3}. Stable: $\zeta \geq 0.1$, neutral: $-0.1 < \zeta < 0.1$, unstable: $\zeta \leq -0.1$

Model parameter	Stable	Neutral	Unstable
Γ	2.7 ± 0.6	3.4 ± 0.7	2.9 ± 1.0
L [m]	33 ± 35	83 ± 57	157 ± 89
$\alpha\varepsilon^{2/3}$ [m$^{4/3}$ s^{-2}]	0.03 ± 0.02	0.03 ± 0.01	0.01 ± 0.01

Fig. 5.7 compares Γ, L and $\alpha\varepsilon^{2/3}$ obtained from fittings with $k_{\min} = 0.001$ m^{-1}, $k_{\max} = 1$ m^{-1} and $tolX = tolFun = 10^{-3}$ with the corresponding parameters obtained when $k_{\min} = 0.02$ m^{-1}, $k_{\max} = 0.8$ m^{-1} and $tolX = tolFun = 10^{-4}$. Note the different color scaling for each parameter. As illustrated in Fig. 2.2 (which uses parameter values matching the FINO1 results), varying Γ or L significantly affects the S_u and S_w curves at low wavenumbers. At high wavenumbers, the curves (particularly S_u) maintain a similar shape despite different parameter values. Changing $\alpha\varepsilon^{2/3}$ on the other hand, makes a big difference to the energy level of both S_u and S_w at all wavenumbers. The wavenumber interval 0.02 m$^{-1} \leq k \leq 0.8$ m^{-1} consists of relatively high wavenumbers, placed to the right in Fig. 2.2. Fig. 2.2 suggests that obtaining accurate estimations of Γ and L within this interval can be challenging, and this is partly the observations in Fig. 5.7. The estimation of $\alpha\varepsilon^{2/3}$ from fittings in the narrow k interval is quite good (the density plot follows $y = x$ quite good), with some overestimation for low $\alpha\varepsilon^{2/3}$ values and some underestimation for high values. Changing $\alpha\varepsilon^{2/3}$ has great impact of the energy level of S_u and S_w in this k interval, and that may explain why rater good estimations of $\alpha\varepsilon^{2/3}$ is achievable. The estimation of L looks quite good until it flats out somewhere below 75 m at the y axis. Increasing L shifts the peak of both S_u and S_w towards lower wavenumbers. The higher value of L, the more to the left the peak of S_u is in a plot corresponding to the middle panel of Fig. 2.2, and the more similar the curves become at high wavenumbers. The same holds for S_w. It may be difficult to estimate L in the interval 0.02 m$^{-1} \leq k \leq 0.8$ m^{-1} because when L becomes sufficiently large, a wide range of L values give approximately the same curves in this interval. This may explain the shape of the plot in the

middle panel of Fig. 5.7. The Γ values obtained for the narrow k interval do not match the values obtained for the broad interval (left panel of Fig. 5.7). The anisotropy parameter Γ affects the height and location of the peak of both S_u and S_w, though the shift in S_w's peak is very small. The peak of S_u is not in the interval $0.02\ \mathrm{m}^{-1} \leq k \leq 0.8$. Since both Γ and L affect the location (in terms of k) of S_u, maybe this can be the reason why it is more difficult give a good estimation of these parameters compared to $\alpha\varepsilon^{2/3}$. However, L decides the location (in terms of k) of the peak of S_w, and since this is in the interval, L can still be estimated with quite good accuracy up to a certain value.

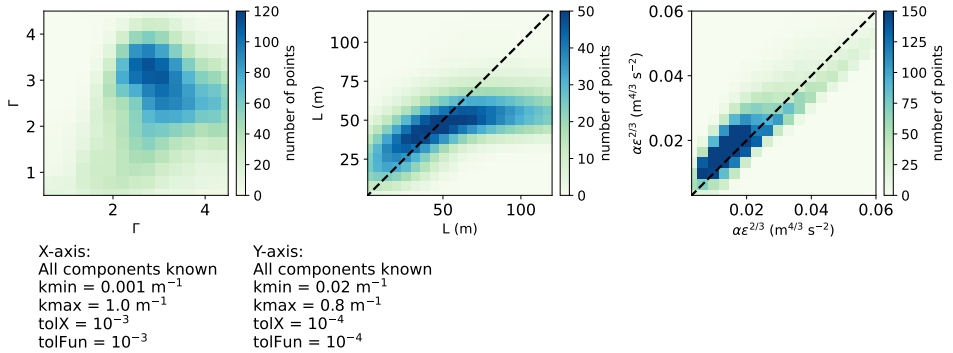

Figure 5.7: Comparison of the model parameters Γ (left panel), L (middle panel) and $\alpha\varepsilon^{2/3}$ (right panel) obtained from fitting the US model to data using different inputs (written under "X-axis" and "Y-axis"). The figure is based on 6665 samples collected during 2007 and 2008 at 81.5 m at FINO1. The dotted line shows $y = x$.

Fig. 5.8 shows the relation between the model parameters obtained from fittings with $0.001\ \mathrm{m}^{-1} \leq k \leq 1.0\ \mathrm{m}^{-1}$ and tolerances 10^{-3} with the mean wind speed. For low mean wind speeds (5 m s^{-1} to 10 m s^{-1}) the value of Γ varies between 0.5 and 4.5 (which are the parameter limits in the fitting function). For higher $\overline{u}$ there is lower occurrence of small Γ values. For $\overline{u} > 20$ m s^{-1}, the minimum Γ value estimated is 2.5. The value of L varies significantly for low wind speeds. For wind speeds above 20 m s^{-1}, L is usually less than 100 m. The highest estimated L for wind speeds above 20 m s^{-1} is 171 m. $\alpha\varepsilon^{2/3}$ increases with $\overline{u}$, and is often below 0.03 $\mathrm{m}^{4/3}$ s^{-2} for mean wind speeds below 8 m s^{-1}. For wind speeds above 20 m s^{-1} $\alpha\varepsilon^{2/3}$ usually exceeds 0.03 $\mathrm{m}^{4/3}$ s^{-2}. A similar figure for $k_{\mathrm{min}} = 0.02\ \mathrm{m}^{-1}$,

$k_{\max} = 0.8$ m^{-1} and tolerances 10^{-4} can be seen in Fig. D.1 in appendix D.

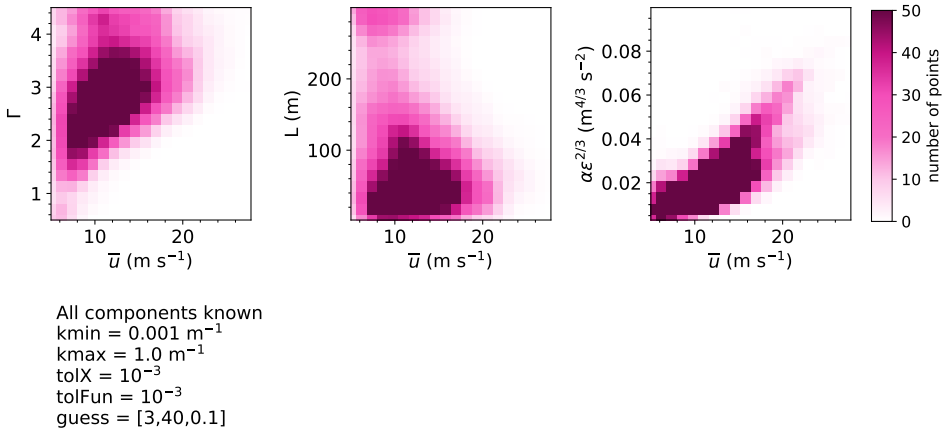

Figure 5.8: Relating the model parameters Γ (left panel), L (middle panel) and $\alpha\varepsilon^{2/3}$ (right panel) to $\overline{u}$. The model parameters are obtained from fitting the US model to all wind components. "guess" refers to the initial guess of the model parameters, and is on the form [Γ, L, $\alpha\varepsilon^{2/3}$]. The figure is based on 6665 samples collected during 2007 and 2008 at 81.5 m at FINO1.

5.4 Comparison with IEC standards

Fig. 5.9a shows σ_u at 81.5 m a.s.l., as a function of the mean wind speed, with errrorbars marking the 10th and 90th percentile. The bin width is 0.5 m s^{-1}, in consistency with IEC 61400-3 (2009), and the center of each bin is at each half m s^{-1}. The Mann values (pink dots) are $(\sigma_u)_{\text{MEF}}$ obtained from fitting the US model to all velocity components with $k_{\min} = 0.001$ m^{-1}, $k_{\max} = 1.0$ m^{-1} and tolerances 10^{-3}. The sonic values (blue dots) corresponds to $(\sigma_u)_{\text{sonic\_F}}$. The Mann and sonic values match very well for all wind speeds, but the overlap is particularly good for wind speeds below 10 m s^{-1}. There are some deviation for high wind speeds, but the number of samples for these wind speeds are very low. The dashed line shows the representative value of σ_u as presented by IEC 61400-3 (2009) calculated from Eq. (2.9). Here $z_{\text{hub}} = 81.5$ m, I_{15} is calculated as the mean turbulence intensity for mean wind speeds between 14.75 m s^{-1} and 15.25 m s^{-1} from the sonic data (that is the blue dot at 15 m s^{-1} in Fig. 5.9b), and z_0 is obtained numerically

from Eq. (2.10). IEC accounts for the 90th percentile, and the curve lies well above the 90th percentile calculated for both the Mann and sonic σ_u, except for mean wind speeds below 7 m s^{-1}. This may suggest that the IEC representation is somewhat too high (conservative), which is also stated by several other studies (Ernst & Seume, 2012; Colone et al., 2018; Cheynet et al., 2024). The same can be observed for the 1-hour σ_u when comparing Eq. (2.11) with the 90th percentile of the measured 1-hour σ_u from the sonic data (Fig. 5.10), although the deviation is less than for the 10-min averages. As to the question of whether $(\sigma_u)_{\text{sonic\_F}}$ is a realistic representation of the 10-min based σ_u, this cannot be checked because only 1-hour averages are available in the data set, and these will be higher than 10-min averages.

Fig. 5.9b is a similar figure as Fig. 5.9a, but for the turbulence intensity rather than σ_u. The turbulence intensity decreases with wind speed up to mean wind speed of 8 m s^{-1}, and increases with wind speed above this (except for at very high wind speeds). The sea roughness increases with the wind speed, which will contribute to increased turbulence intensity. The correspondence between the binned turbulence intensity calculated from $(\sigma_u)_{\text{MEF}}$ (pink dots) and $(\sigma_u)_{\text{sonic\_F}}$ (blue dots) is good. For mean wind speeds 26.5, 27.5 and 28.0 m s^{-1} there are only one sample, thus there are no 10th or 90th percentile visible in Fig. 5.9 and Fig. 5.10.

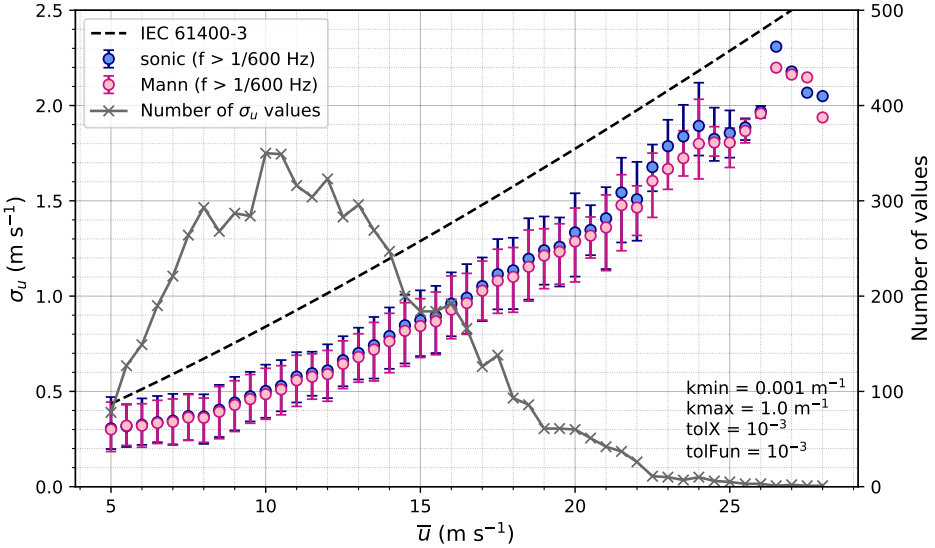

(a) σ_u as a function of $\overline{u}$. The dashed line is calculated using Eq. (2.9).

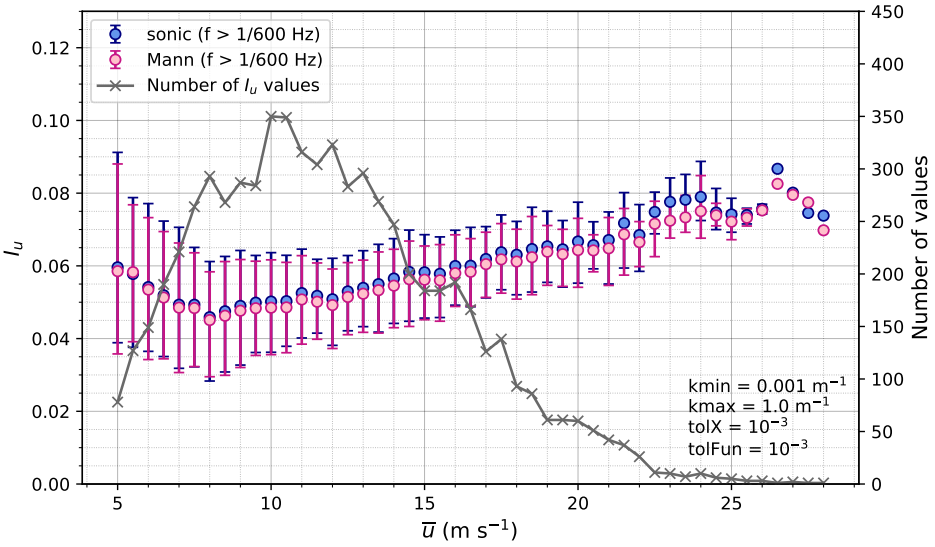

(b) I_u as a function of $\overline{u}$.

Figure 5.9: (a) σ_u and (b) I_u as a function of $\overline{u}$. The bin width is 0.5 m s^{-1}, and the center of each bin is placed at each half m s^{-1}. The error bars mark the 10th and 90th percentile. The blue dots are calculated from $(\sigma_u)_{\text{sonic\_F}}$. The pink dots are calculated from $(\sigma_u)_{\text{MEF}}$ obtained from fitting the US model to all velocity components. The figure is based on 6665 samples collected during 2007 and 2008 at 81.5 m at FINO1.

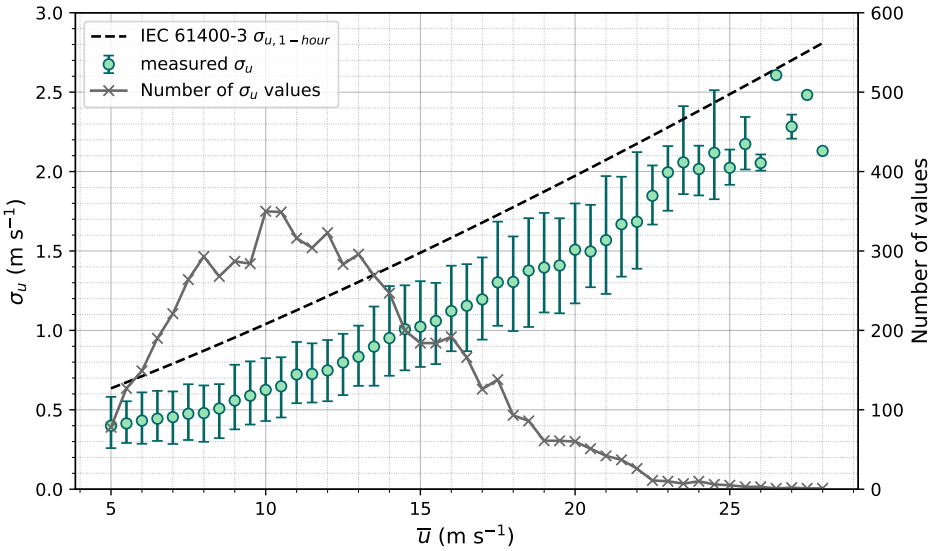

Figure 5.10: σ_u as a function of $\overline{u}$. The bin width is 0.5 m s^{-1}, and the center of each bin is placed at each half m s^{-1}. The error bars mark the 10th and 90th percentile. The dashed line is calculated using Eq. (2.11) for 1-hour statistics. The green dots are measured by sonic anemometer over an averaging period of one hour. The figure is based on 6665 samples collected during 2007 and 2008 at 81.5 m at FINO1.

Chapter 6

Fitting the US model to the vertical component only

6.1 Limited wavenumber interval

The results after fitting the US model to the vertical component only, give quite different results than when all components are known. When only the vertical component is known, the agreement between $(\sigma_u)_{\text{Mann}}$ and $(\sigma_u)_{\text{targ}}$ is significantly affected by the choice of k interval in the fitting. Several different combinations of k intervals and iteration tolerances were tested on data collected in January 2008 to see which combination led to the best correspondence between $(\sigma_u)_{\text{Mann}}$ and $(\sigma_u)_{\text{targ}}$. Six of these are shown in Fig. 6.1, with three different k intervals placed horizontally, the upper panels having tolerances of 10^{-3} and the lower panels having tolerances of 10^{-4}. The broad k interval $0.001\ \text{m}^{-1} \leq k \leq 1.0\ \text{m}^{-1}$ (left panels), which give very good fitting results both for the limited and extended k interval when all components are known, results in significantly higher RMSE than the other narrower intervals with a higher k_{min}. In all situations in Fig. 6.1, the US model does a slight overestimation of $(\sigma_u)_{\text{Mann}}$ compared to $(\sigma_u)_{\text{targ}}$ for low wind speeds, except for a few outliers. The wind spectra $(S_u)_{\text{targ}}$ and $(S_w)_{\text{targ}}$ corresponding to these outliers do not look like typical wind spectra, but they still satisfy the slope and RMSE criteria defined in section 3.1. Note that these outliers are not the same samples as the outliers in the left panels of Fig. 5.1 mentioned in section 5.1. This emphasizes that the method for filtering out poor measurements is sometimes insufficient.

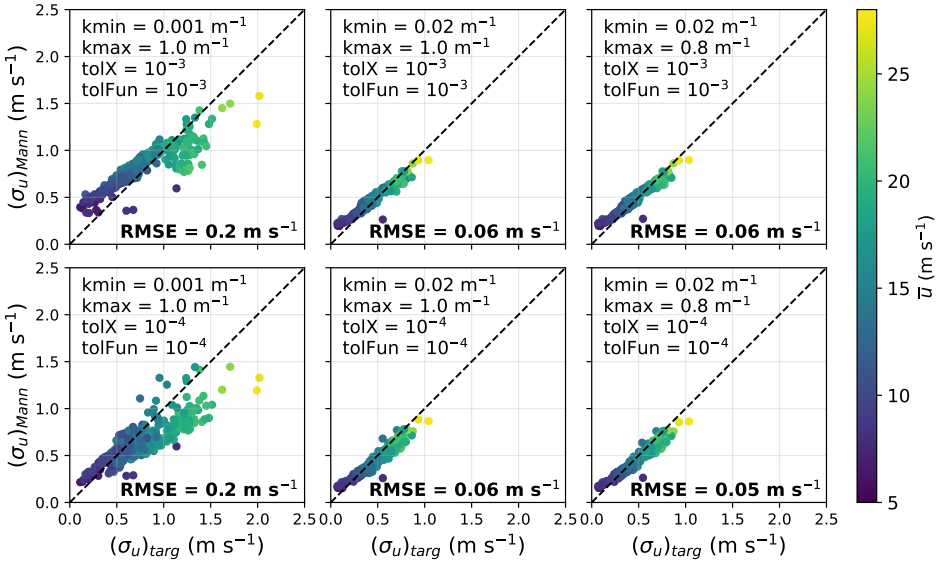

Figure 6.1: Comparison of $(\sigma_u)_{\text{Mann}}$ and $(\sigma_u)_{\text{targ}}$ obtained from fitting the US model to S_w using different k_{min}, k_{max} and tolerances. The figure is based on 381 samples obtained from measurements at 81.5 m at FINO1 in January 2008.

The choice of iteration tolerances exert a notable influence on the scatter plots in Fig. 6.1, but the two tolerances lead to the same RMSE value (when considering only one significant digit) for the k intervals in the left and middle panels. For $0.001\ \text{m}^{-1} \leq k \leq 1.0\ \text{m}^{-1}$ (left panels), choosing tolerances of 10^{-3} tends to overestimate $(\sigma_u)_{\text{Mann}}$ when $(\sigma_u)_{\text{targ}} < 1.0\ \text{m s}^{-1}$. The overestimation happens especially for mean wind speeds below 20 m s^{-1}, and is also observed in similar plots created for each month of 2007 and 2008. The overestimation of $(\sigma_u)_{\text{Mann}}$ is due to overestimation of $(S_u)_{\text{Mann}}$, which seem to be a common result when fitting the US model to S_w only, using $k_{\text{min}} = 0.001\ \text{m}^{-1}$, $k_{\text{max}} = 1.0\ \text{m}^{-1}$ and tolerances 10^{-3}. Such tendencies are not observed in fittings when all components are known. The overestimation of $(S_u)_{\text{Mann}}$ for $k_{\text{min}} = 0.001\ \text{m}^{-1}$, $k_{\text{max}} = 1.0\ \text{m}^{-1}$ and tolerances 10^{-3} will be discussed further in section 6.3. Iteration tolerances of 10^{-4} give the same RMSE value, but there are more points below the $y = x$ line compared to tolerances of 10^{-3}. At high mean wind speeds, σ_u is underestimated by the US model for $0.001\ \text{m}^{-1} \leq k \leq 1.0\ \text{m}^{-1}$ (the two yellow dots in the left panels of Fig. 6.1). This trend is also evident for

other intervals of k, though to a significantly lesser extent. The wind spectra corresponding to these two yellow dots look normal, and have good fits when all components are known. When only the vertical component is known, $(S_w)_{\text{Mann}}$ fits good to $(S_w)_{\text{targ}}$ (even better than when all components are known), but the estimation of the along-wind spectrum is bad (which explains the outlier tendencies in Fig. 6.1).

Of all the tested combinations, the smallest RMSE is obtained for $k_{\min} = 0.02$ m^{-1}, $k_{\max} = 0.8$ m^{-1} and tolerances 10^{-4} (lower right panel of Fig. 6.1). Note that narrower k intervals than this were tested, but did not result in a lower RMSE. The fitting options $k_{\min} = 0.02$ m^{-1}, $k_{\max} = 0.8$ m^{-1} and tolerances 10^{-4} generally give low RMSE for all months when comparing $(\sigma_u)_{\text{Mann}}$ and $(\sigma_u)_{\text{targ}}$.

6.2 Extended wavenumber interval

As for the case when all components are known, the results are not good when extending the k interval to match the original $(k)_{\text{sonic}}$ (Fig. A.2), but they are better when only frequencies larger than 1/600 Hz are considered. For January 2008, comparing $(\sigma_u)_{\text{MEF}}$ and $(\sigma_u)_{\text{sonic\_F}}$ result in the same RMSE (when only considering one significant digit) for the different k intervals and tolerances in Fig. 6.2. However, the scatter plots look quite different for the two tolerance options, tolerance 10^{-3} generally leads to more points above the $y = x$ line (the upper panels of Fig. 6.2). In all cases, $(\sigma_u)_{\text{MEF}}$ is underestimated compared to $(\sigma_u)_{\text{sonic\_F}}$ for very high wind speeds.

When including all samples from 2007 and 2008, the results are (not surprisingly) worse when only S_w is known compared to when all components are known. For fittings to S_w only, with $k_{\min} = 0.001$ m^{-1}, $k_{\max} = 1.0$ m^{-1} and tolerances 10^{-3}, the RMSE values are the same for all stability cases (Fig. 6.3a), and are in the same order of magnitude as for all component fittings in Fig. 5.6a with a narrower k interval at high values ($k_{\min} = 0.02$ m^{-1} and $k_{\max} = 0.8$ m^{-1}). The density plots (Fig. 6.3b) show that the majority of the points lie above the $y = x$ line for all stability cases, thus the US model tends to overestimate σ_u for $k_{\min} = 0.001$ m^{-1}, $k_{\max} = 1.0$ m^{-1} and tolerances 10^{-3}. This is consistent with plots of $(S_u)_{\text{Mann}}$, which is often overestimated for 0.001 m$^{-1} \leq k \leq 1.0$ m^{-1}.

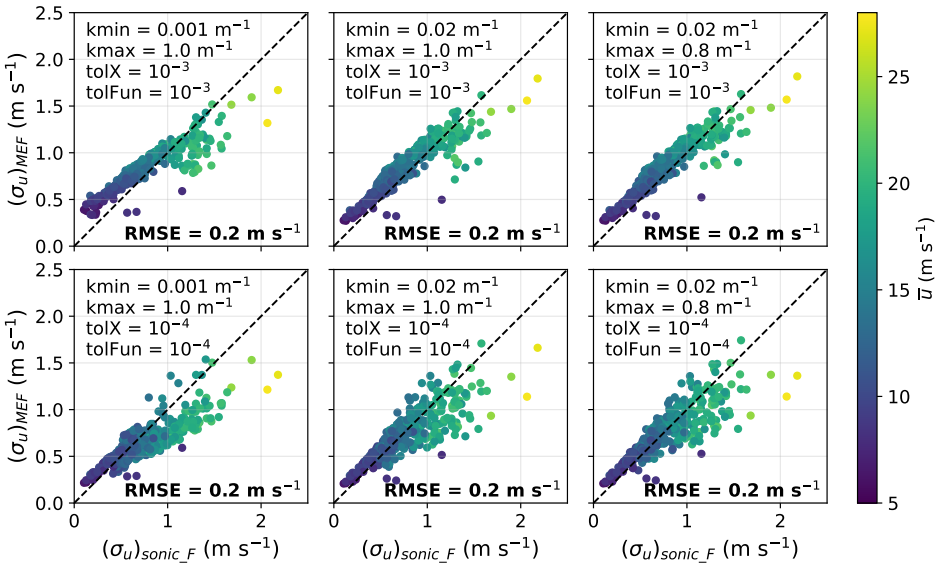

Figure 6.2: Comparison of $(\sigma_u)_{\mathrm{MEF}}$ and $(\sigma_u)_{\mathrm{sonic\_F}}$ obtained from fitting the US model to S_w using different k_{min}, k_{max} and tolerances. The figure is based on 381 samples obtained from measurements at 81.5 m in January 2008. The dashed line shows $y = x$.

Fitting the US model to S_w only with $k_{\mathrm{min}} = 0.02$ m^{-1}, $k_{\mathrm{max}} = 0.8$ m^{-1} and tolerances 10^{-4} result in lower RMSE for stable and unstable atmosphere (Fig. 6.4a) compared to the S_w only fitting with the broader k interval in Fig. 6.3a. However, it seem like the narrower k interval gives larger scatter, especially for stable and neutral conditions. The density plots in Fig. 6.4b show that also for this k interval and tolerances, the majority of the points lie above the $y = x$ line, but more points lie closer to the line than the case in Fig. 6.3b. The density plots also demonstrate that there are few points that deviate significantly from the line in Fig. 6.4a. Thus, choosing a higher k_{min} value and a quite narrow interval may be favorable when only S_w is known compared to when all components are known. When all the components are known, the relatively broad k interval 0.001 m$^{-1} \leq k \leq 1.0$ m^{-1} gives the best fitting results.

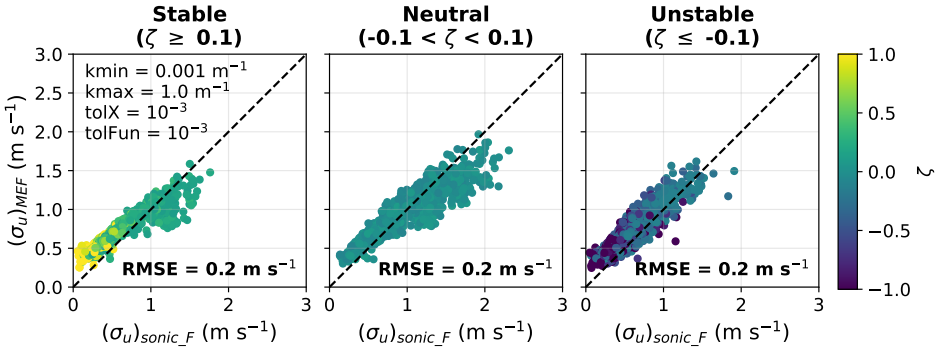

(a) Scatter plot with colors showing stability.

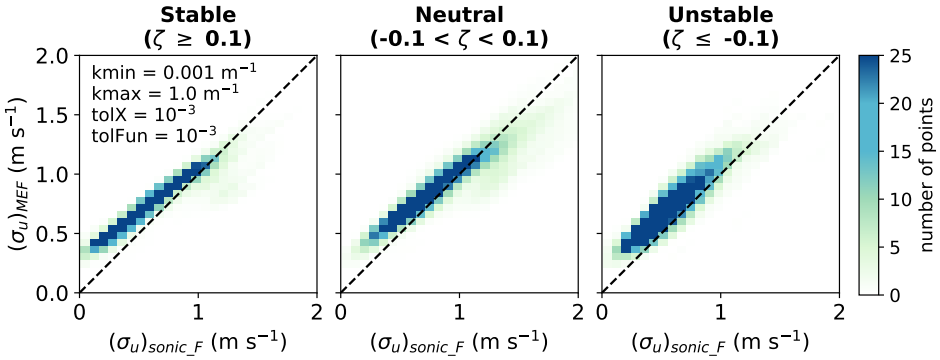

(b) Density plot with colors showing number of points.

Figure 6.3: $(\sigma_u)_{\text{sonic\_F}}$ obtained from Eq. (2.7) for frequencies above 1/600 Hz. $(\sigma_u)_{\text{MEF}}$ obtained from fitting the US model to data of the vertical wind component, calculated using Eq. (4.6). The figure is based on 1871 stable, 2007 neutral and 2787 unstable samples collected by sonic anemometer at height 81.5 m at FINO1 during 2007 and 2008. The dashed line shows $y = x$.

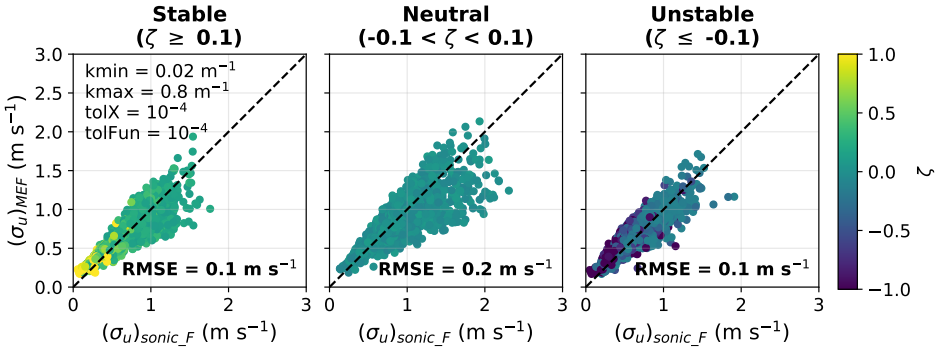

(a) Scatter plot with colors showing stability.

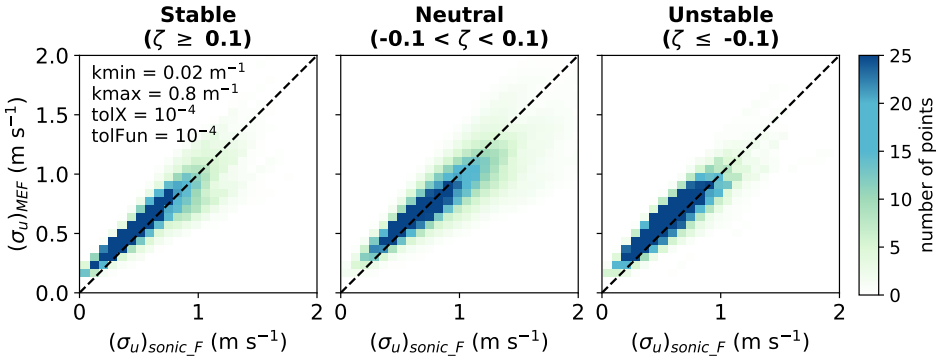

(b) Density plot with colors showing number of points.

Figure 6.4: $(\sigma_u)_{\text{sonic\_F}}$ obtained from Eq. (2.7) for frequencies above 1/600 Hz. $(\sigma_u)_{\text{MEF}}$ obtained from fitting the US model to data of the vertical wind component, calculated using Eq. (4.6). The figure is based on 1871 stable, 2007 neutral and 2787 unstable samples collected by sonic anemometer at height 81.5 m at FINO1 during 2007 and 2008. The dashed line shows $y = x$.

6.3 Model parameters

Fig. 6.5 compares the model parameters obtained from fitting the US model to the vertical component only with the corresponding parameters obtained when all velocity components were known, both cases using $k_{\min} = 0.001$ m^{-1}, $k_{\max} = 1.0$ m^{-1} and tolerances 10^{-3} in the fittings. Again, the values obtained from fittings to all component using these inputs are considered good estimations. The Γ values obtained from fittings to S_w corresponds poorly to the estimation of Γ when all components are known. This is as expected because a good estimation of Γ requires information about both S_u and S_w, as changing Γ has a substantial influence on S_u but not so much on S_w. Γ is overestimated in 79% of the cases when only the vertical component is known, which will contribute to overestimation of S_u and thereby also σ_u. The estimation of $\alpha\varepsilon^{2/3}$ is associated with large uncertainties, with no evident relationship between the parameters obtained when only S_w is known and the parameters obtained when all components are known. Generally, $\alpha\varepsilon^{2/3}$ is also overestimated in fittings to only the vertical component (93% of the cases), which contributes to overestimation of S_u (and σ_u), as this parameter scales with turbulence intensity. Fitting the US model to the vertical component generally underestimates L (84% of the cases), it seem like the pattern in the middle panel of Fig. 6.5 follows some line with a slope smaller than one. Underestimation of L will contribute to underestimation of S_u and thus also σ_u. However, the overestimation of Γ and $\alpha\varepsilon^{2/3}$ outweighs the underestimation of L, resulting in an overall overestimation of σ_u as observed in Fig. 6.3b. The combination of underestimating L and overestimating Γ and $\alpha\varepsilon^{2/3}$ applies to 65% of the samples, and in 97% of these cases $(\sigma_u)_{\text{MEF}}$ is overestimated compared to $(\sigma_u)_{\text{sonic\_F}}$.

It is observed from spectrum plots that in some cases $(S_w)_{\text{Mann}}$ obtained from fitting the US model to S_w is a poor fit to its target spectrum, while the corresponding all-component fit is relatively good, both cases using $k_{\min} = 0.001$ m^{-1}, $k_{\max} = 1.0$ m^{-1} and tolerances 10^{-3}. A typical such situation is shown in Fig. 6.6. While the all-component fit gives very good correspondence between $(\sigma_u)_{\text{sonic\_F}}$ and $(\sigma_u)_{\text{MEF}}$ (both being 0.5 m s^{-1}), fitting to the vertical component overestimates σ_u with $(\sigma_u)_{\text{MEF}} = 0.7$ m s^{-1}. The poor fit might be because the fitting function found a local minimum rather than a local maximum, which can be a challenge when MultiStart is not used. Using Multistart in Matlab, multiple solutions of a problem

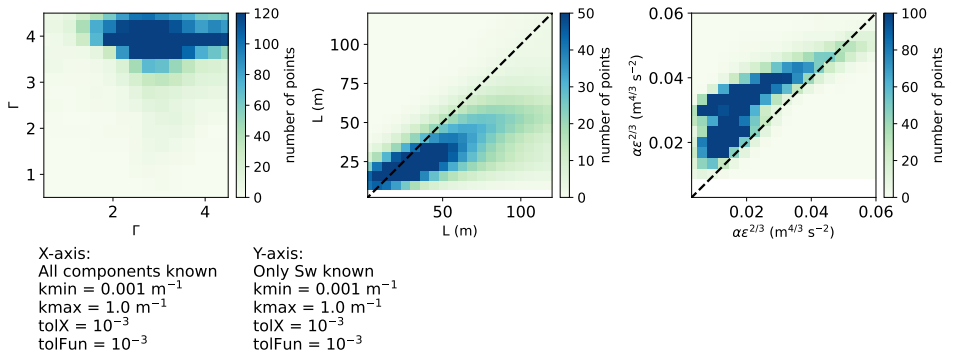

Figure 6.5: Comparison of the model parameters Γ (left panel), L (middle panel) and $\alpha\varepsilon^{2/3}$ (right panel) obtained from fitting the US model to data using different inputs (written under "X-axis" and "Y-axis"). The figure is based on 6665 samples collected during 2007 and 2008 at 81.5 m at FINO1. The dashed line shows $y = x$.

can be found by starting from different initial guesses, aiming to identify the global solution. Nevertheless, this approach is time-consuming. Given that one of the main goals of this thesis is to employ an efficient method, the decision was made to avoid using MultiStart. The initial guess ($\Gamma = 3$, $L = 40$ m and $\alpha\varepsilon^{2/3} = 0.1$ m$^{4/3}$ s^{-2}) is the same in all fittings, which may not suit all samples. To check if the bad fitting to S_w in the right panel of Fig. 6.6 is due to a local minimum, the initial guess was changed to the model parameters obtained when all components where known, namely $\Gamma = 3.5$, $L = 61$ m and $\alpha\varepsilon^{2/3} = 0.01$ m$^{4/3}$ s^{-2}. This did indeed improve the fitting result significantly (Fig. 6.7), with estimated model parameters $\Gamma = 3.3$, $L = 38$ m and $\alpha\varepsilon^{2/3} = 0.02$ m$^{4/3}$ s^{-2}. Even though this L value is still rather different from the all component L, the fitting resulted in $(\sigma_u)_{\mathrm{MEF}} = 0.5$ m s^{-1}, which was the goal. The improved outcome suggests that a local minimum was encountered in the initial fitting. Local minima seem to be a small issue when all components are known (as these results are generally very good), but the effect becomes significant when fitting the US model to the vertical component only. Information lacks when only S_w is available, thus increasing the probability of encountering local minima. Therefore, when only S_w is known, the iteration tolerances might need to be smaller than when all wind components are available. Using tolerances of 10^{-4} instead of 10^{-3} for $k_{\mathrm{min}} = 0.001$ m^{-1} and $k_{\mathrm{max}} = 1.0$ m^{-1} do indeed

give better fitting results for the sample in Fig. 6.6, see Fig. F.1 in appendix F. The parameter estimations are significantly better using 10^{-4}, especially for L, see Fig. C.1 in appendix C. However, the overall $(\sigma_u)_{\text{MEF}}$ results are not very good (see Fig. B.3 and Fig. E.1), so changing the tolerances is not enough to provide good σ_u estimations.

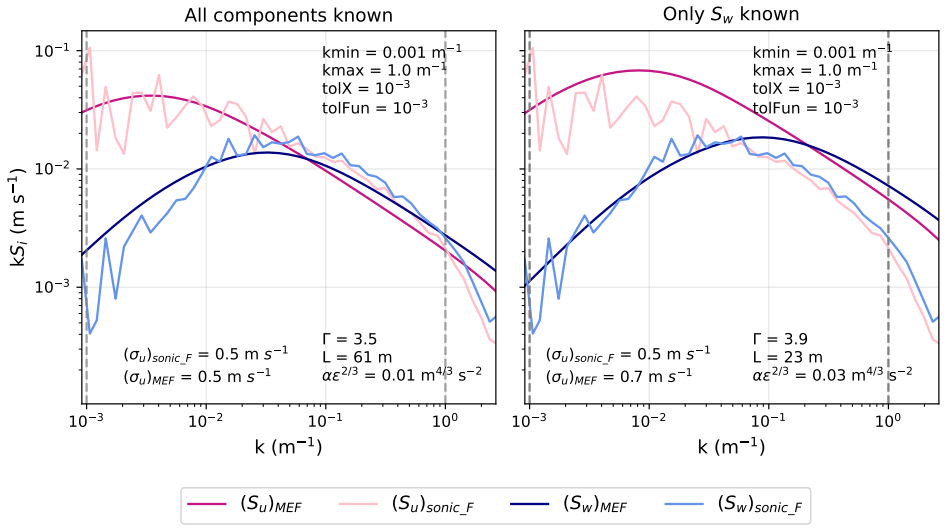

Figure 6.6: Sonic wind spectra obtained from measurements at 81.5 m height at the FINO1 platform in February 2008 ($\zeta = 0.03$ (neutral), $\overline{u} = 11.5$ m s^{-1}). The vertical dashed lines show k_{min} and k_{max} used when fitting the US model to all wind components (left panel) and only S_w (right panel).

The initial guess of $\alpha\varepsilon^{2/3}$ is 0.1 m$^{4/3}$ s^{-2}, which is much larger than the common estimated values (Fig. 6.5). This initial guess is based on early testing of the fitting function to the FINO1 data, and it is likely that a smaller value would have been more appropriate. For fittings when all components are known, this does not seem to be an issue. Since local minima is a challenge when only S_w is known, the poor initial guess for $\alpha\varepsilon^{2/3}$ may affect these fittings significantly. Fig. 6.8 is a similar figure as Fig. 6.5, with the same input parameters except a new initial guess (0.03 m$^{4/3}$ s^{-2}) for $\alpha\varepsilon^{2/3}$ for the Y-axis. Using this lower $\alpha\varepsilon^{2/3}$ as initial guess gives less overestimation of $\alpha\varepsilon^{2/3}$. This also leads to density plots of σ_u lying closer to the $y = x$ line, see Fig. B.4b in appendix B. For tolerances 10^{-4} and new initial guess for $\alpha\varepsilon^{2/3}$, the estimation of L and $\alpha\varepsilon^{2/3}$ looks quite good (Fig. C.2), but the estimation of σ_u is still not very good, see Fig. B.5.

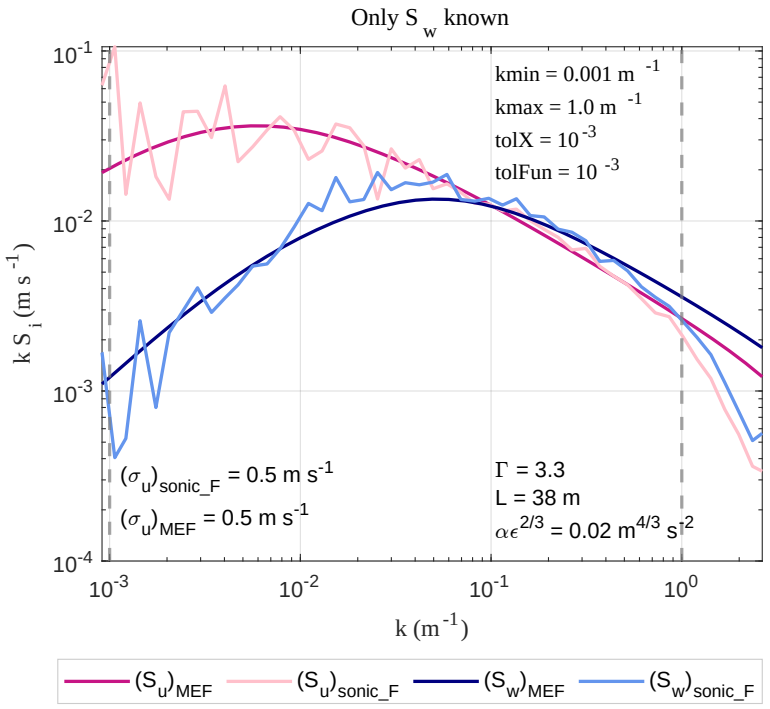

Figure 6.7: Sonic wind spectra obtained from measurements at 81.5 m height at the FINO1 platform in February 2008 ($\zeta = 0.03$ (neutral), $\overline{u} = 11.5$ m s^{-1}). The vertical dashed lines show $k_{\min}$ and $k_{\max}$ used when fitting the US model to S_w. The same fitting inputs as in the right panel in Fig. 6.6, but with new initial guess for the model parameters: $\Gamma = 3.5$, $L = 61$ m and $\alpha\varepsilon^{2/3} = 0.01$ m$^{4/3}$ s^{-2}.

Fig. 6.9 compares the model parameters obtained from fitting the US model to S_w only with $k_{\min} = 0.02$ m^{-1}, $k_{\max} = 0.8$ m^{-1} and tolerances 10^{-4} with the parameters obtained in all component fittings with $k_{\min} = 0.001$ m^{-1}, $k_{\max} = 1.0$ m^{-1} and tolerances 10^{-3}. In other words, it compares the model parameters in Fig. 6.4b and Fig. 5.5b. The estimation of Γ is challenging as expected, due to lack of information about S_u. L follows quite good the $y = x$ line, however the colors are more diffuse (meaning less dense and larger spread) than in Fig. 5.7 and Fig. 6.5. Increasing L results in S_w having both a higher peak and shifting it towards lower wavenumbers. Changing L thus has a considerable impact on S_w. The peak of S_w is generally in the interval 0.02 m$^{-1} \leq k \leq 0.8$ m^{-1}, which might explain why L can be estimated fairly good in this interval solely based on S_w. As for all

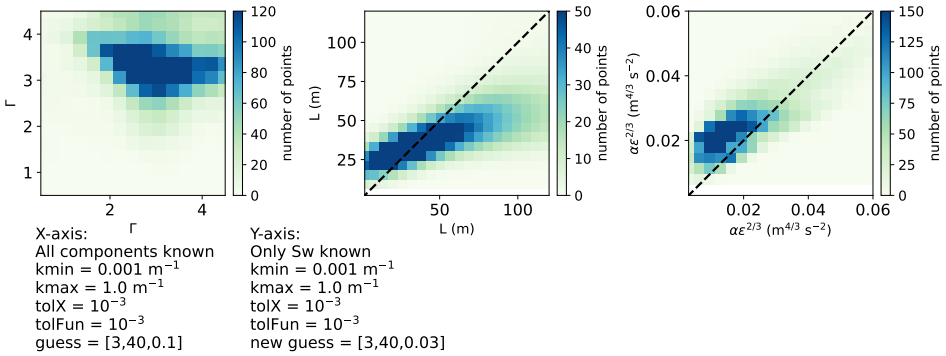

Figure 6.8: Comparison of the model parameters Γ (left panel), L (middle panel) and $\alpha\varepsilon^{2/3}$ (right panel) obtained from fitting the US model to data using different inputs (written under "X-axis" and "Y-axis"). The figure is based on 6665 samples collected during 2007 and 2008 at 81.5 m at FINO1. The dashed line shows $y = x$. Similar as Fig. 6.5, but with new initial guess for $\alpha\varepsilon^{2/3}$ on the Y-axis: $\alpha\varepsilon^{2/3} = 0.03$ m$^{4/3}$ s^{-2}.

component fitting with the same k interval and tolerances (Fig. 5.7), there seem to be some flattening below 75 m, however this is less obvious when only S_w is known. Like for the all component fitting, it might be difficult to estimate L in the interval $0.02\ \text{m}^{-1} \leq k \leq 0.8\ \text{m}^{-1}$ because when L becomes sufficiently large, a wide range of L values give approximately the same S_u and S_w curves in this interval. $\alpha\varepsilon^{2/3}$ do not follow $y = x$, it tends to be slightly overestimated, but the estimation is still quite good. For a similar figure as Fig. 6.9, but with new initial guess (0.03 m$^{4/3}$ s^{-2}) for $\alpha\varepsilon^{2/3}$, see Fig. C.3 in appendix C. The estimation of L and $\alpha\varepsilon^{2/3}$ looks better, and there is some change in the estimation of $(\sigma_u)_{\text{MEF}}$, see Fig. B.6 and Fig. E.4. Since changing the initial guess for $\alpha\varepsilon^{2/3}$ from 0.1 m$^{4/3}$ s^{-2} to 0.03 m$^{4/3}$ s^{-2} was done quite late in the work on the thesis, the choice were made to continue the analysis with the original initial guess.

For S_w only fitting in the interval $0.02\ \text{m}^{-1} \leq k \leq 0.8\ \text{m}^{-1}$ it is difficult to make an overall conclusion, because of the substantial variation in outcomes when observing plots of the wind spectra. The estimated parameters are (of course) depending on the shape of S_w in this interval. In the right panel of Fig. 6.10, it is observed that just to the right of the k_{min} line, it appears as if $(S_u)_{\text{sonic\_F}}$ is about to slope more steeply downward to the left than it actually does. This leads to the fitting function estimating parameters that

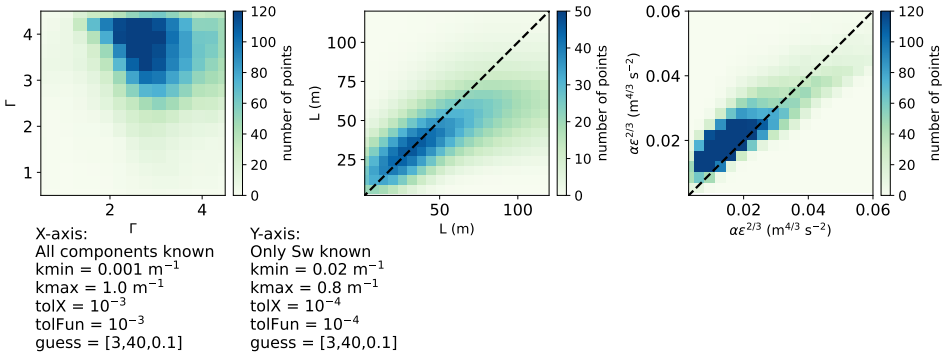

Figure 6.9: Comparison of the model parameters Γ (left panel), L (middle panel) and $\alpha\varepsilon^{2/3}$ (right panel) obtained from fitting the US model to data using different inputs (written under "X-axis" and "Y-axis"). The figure is based on 6665 samples collected during 2007 and 2008 at 81.5 m at FINO1. The dashed line shows $y = x$.

result in an overly sharp $(S_w)_{\mathrm{MEF}}$ (dark blue curve) with too low energy at low wavenumbers. Γ is close to zero (isotropic turbulence). These parameters generate an along-wind spectrum that do not look like the sonic spectrum at all, which result in bad correspondence between $(\sigma_u)_{\mathrm{sonic\_F}}$ and $(\sigma_u)_{\mathrm{MEF}}$. Changing the initial guess to the values obtained in the all component fitting in the left panel of Fig. 6.10 makes little difference to the results, with the estimated parameters being $\Gamma = 0.8$, $L = 38$ m and $\alpha\varepsilon^{2/3} = 0.04$ m$^{4/3}$ s^{-2}. This may indicate that the bad fitting in this case is not due to local minima, rather lack of information of S_w because the k_{min} value is too large for this particular sample. The thought behind choosing such a large k_{min} as 0.02 m^{-1}, is that the uncertainty increases as the frequency decreases. The interval $0.02\ \mathrm{m}^{-1} \leq k \leq 0.8\ \mathrm{m}^{-1}$ is chosen because it gave the lowest RMSE when comparing $(\sigma_u)_{\mathrm{Mann}}$ and $(\sigma_u)_{\mathrm{targ}}$ when only considering data from January 2008. This k_{min} value is maybe not optimal.

The model parameters obtained from fitting the US model to S_w using $k_{\mathrm{min}} = 0.02$ m^{-1}, $k_{\mathrm{max}} = 0.8$ m^{-1} and tolerances 10^{-4} are plotted against $\overline{u}$ in Fig. 6.11. There is no evident relationship between Γ or L and the mean wind speed. $\alpha\varepsilon^{2/3}$ increases with $\overline{u}$, like in Fig. 5.8. For low mean wind speeds, the value of $\alpha\varepsilon^{2/3}$ is also quite low, typically in the range 0.01 m$^{4/3}$ s^{-2} to 0.02 m$^{4/3}$ s^{-2} for mean wind speeds between 5 m s^{-1} and 8 m s^{-1}. Low values of $\alpha\varepsilon^{2/3}$ lead to low PSD values. As previously

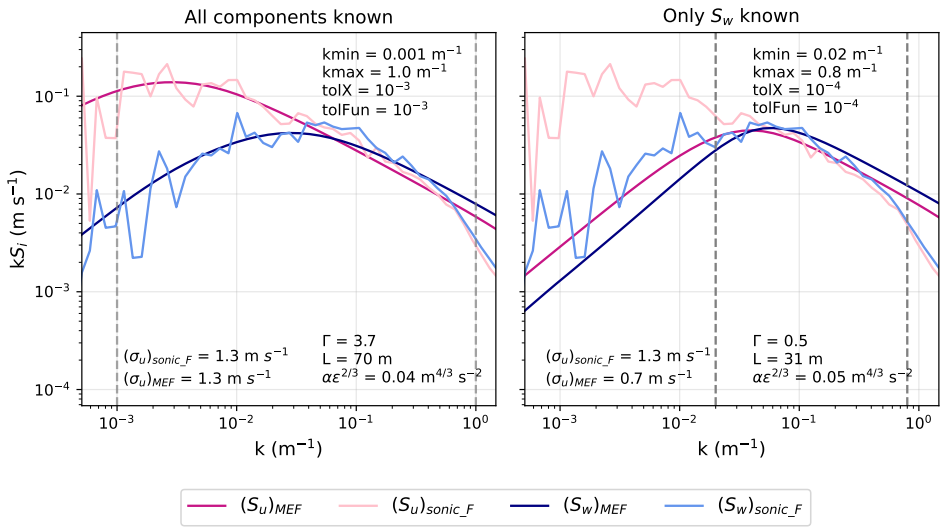

Figure 6.10: Sonic wind spectra obtained from measurements at 81.5 m height at the FINO1 platform in February 2008 ($\zeta = -0.05$ (near neutral), $\overline{u} = 20.6$ m s^{-1}). The vertical dashed lines show $k_{\min}$ and $k_{\max}$ used when fitting the US model to all wind components (left panel) and only S_w (right panel).

stated, the US model estimates $\alpha\varepsilon^{2/3}$ quite well solely based on S_w with $k_{\min} = 0.02$ m^{-1}, $k_{\max} = 0.8$ m^{-1} and tolerances 10^{-4}. Therefore, if the $\alpha\varepsilon^{2/3}$ value obtained from fitting the US model to all wind components (with $k_{\min} = 0.001$ m^{-1}, $k_{\max} = 1.0$ m^{-1} and tolerances 10^{-3}) is low, the corresponding value obtained from fitting to S_w with $k_{\min} = 0.02$ m^{-1}, $k_{\max} = 0.8$ m^{-1} and tolerances 10^{-4} is also low. When only S_w is known, the parameters are adjusted to fit S_w, which means that the estimated parameters may provide a better fit to S_w compared to the all component fit with $k_{\min} = 0.001$ m^{-1}, $k_{\max} = 1.0$ m^{-1} and tolerances 10^{-3}. For small $\alpha\varepsilon^{2/3}$, what seems to be a small adjustment in the shape of the $(S_w)_{\mathrm{MEF}}$ curve can lead to large adjustments in the values of Γ and L and quite significant adjustments in the shape of the $(S_u)_{\mathrm{MEF}}$ curve. Since the PSD values are very low for small $\alpha\varepsilon^{2/3}$, the agreement between $(\sigma_u)_{\mathrm{MEF}}$ and $(\sigma_u)_{\mathrm{sonic\_F}}$ will still be quite good, without $(S_u)_{\mathrm{MEF}}$ necessarily being a good match to $(S_u)_{\mathrm{sonic\_F}}$. For high mean wind speeds ($\overline{u} > 20$ m s^{-1}), $\alpha\varepsilon^{2/3}$ typically exceeds 0.4 m$^{4/3}$ s^{-2}, resulting in high PSD values. This means that large adjustments of Γ and L (which again result in small adjustments in the

shape of $(S_w)_{\mathrm{MEF}}$) will have a significant impact on $(S_u)_{\mathrm{MEF}}$ and thereby also $(\sigma_u)_{\mathrm{MEF}}$. Generally Γ is underestimated for $\overline{u} > 20$ m s^{-1} (86% of the cases) compared to the values in Fig. 5.8. For $\overline{u} > 20$ m s^{-1}, the value of Γ in Fig. 6.11 varies from 0.5 up to 4.5. This is quite different from the case in Fig. 5.8, where the minimum Γ value is 2.5 for such mean wind speeds. When $\overline{u} > 20$ m s^{-1} and Γ is underestimated, $(\sigma_u)_{\mathrm{MEF}}$ is underestimated in 97% of the cases. This may explain why it is challenging to make a good estimation of σ_u solely based on fitting the US model to S_w at mean high wind speeds. This challenge is evident across all the inputs that have been tested, see for instance Fig. E.1, Fig. E.2, Fig. E.4 in appendix E.

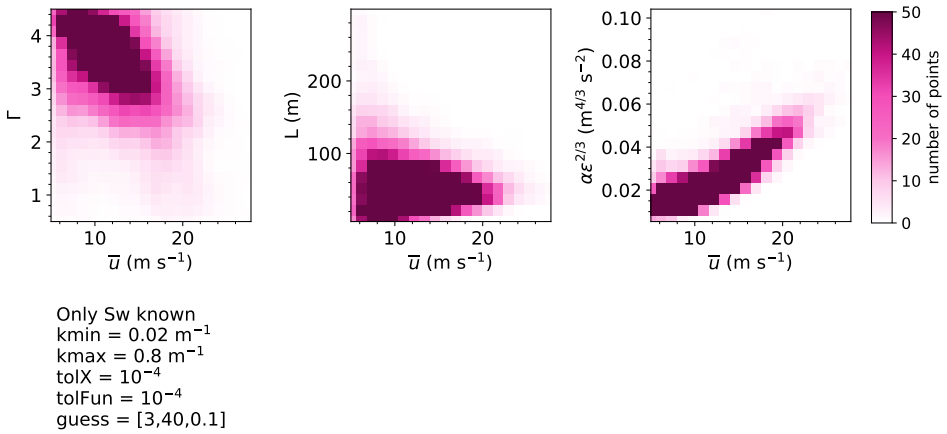

Figure 6.11: Relating the model parameters Γ (left panel), L (middle panel) and $\alpha\varepsilon^{2/3}$ (right panel) to $\overline{u}$. The model parameters are obtained from fitting the US model to S_w. "guess" refers to the initial guess of the model parameters, and is on the form [Γ, L, $\alpha\varepsilon^{2/3}$]. The figure is based on 6665 samples collected during 2007 and 2008 at 81.5 m at FINO1.

6.4 Comparison with IEC standards

Fig. 6.12a shows the results when the standard deviation of the along-wind component is estimated using Eq. (2.21), which is in accordance with the IEC guidelines. Here, the standard deviation of the vertical component is calculated using Eq. (2.7) for frequencies above 1/600 Hz, namely $(\sigma_w)_{\mathrm{sonic\_F}}$. Eq. (2.21) overestimates σ_u, as most point lie above the $y = x$ line, with

only a few exceptions. This is emphasized by the density plot in Fig. 6.12b. Fitting the US model to the vertical component only with $k_{\min} = 0.02\ \mathrm{m}^{-1}$, $k_{\max} = 0.8\ \mathrm{m}^{-1}$ and tolerances 10^{-4} (Fig. 6.4a) results in lower RMSE for stable and unstable atmosphere compared to the IEC method. For neutral atmosphere, the RMSE is the same for both methods, despite Fig. 6.4a showing large scatter. By comparing the density plot in Fig. 6.12b with Fig. 6.4b, it seems like fitting the US model to S_w gives a better estimation of σ_u than Eq. (2.21), because the density plot is closer to the $y = x$ line.

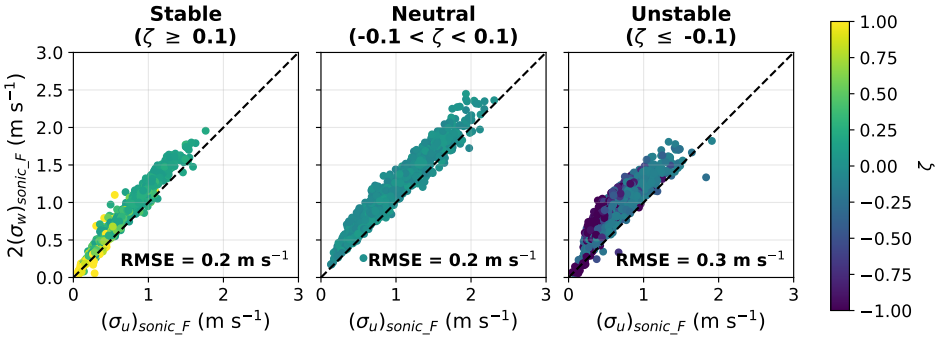

(a) Scatter plot with colors showing stability.

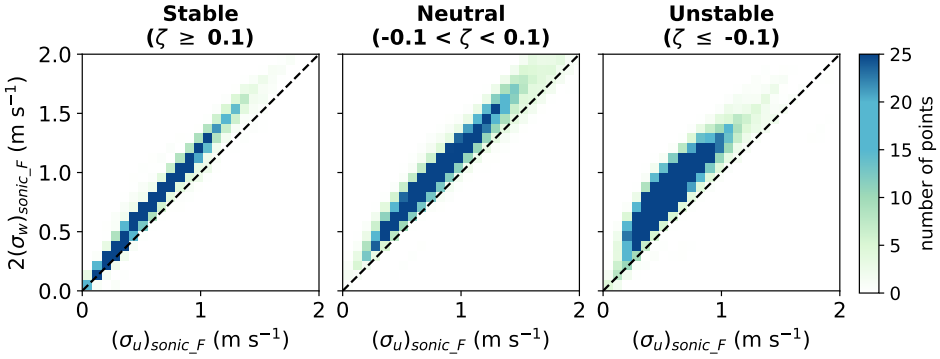

(b) Density plot with colors showing number of points.

Figure 6.12: Comparing $(\sigma_u)_{\mathrm{sonic\_F}}$ with $2\,(\sigma_w)_{\mathrm{sonic\_F}}$ in accordance to Eq. (2.21). $(\sigma_i)_{\mathrm{sonic\_F}}$ calculated using Eq. (2.7) for $f > 1/600$ Hz. The figure is based on 6665 samples collected during 2007 and 2008 at 81.5 m at FINO1.

Fig. 6.13a shows σ_u at 81.5 m a.s.l., as a function of the mean wind speed, with errror bars and bins defined in the same way as for Fig. 5.9a.

The Mann values are $(\sigma_u)_{\text{MEF}}$ obtained from fitting the US model to S_w only with $k_{\text{min}} = 0.02$ m^{-1}, $k_{\text{max}} = 0.8$ m^{-1} and tolerances 10^{-4}. For mean wind speeds below 15 m s^{-1} the Mann values are a little bit higher than the sonic values. For wind speeds above 15 m s^{-1}, the sonic values exceed the Mann values, but also the number of samples in these bins is lower than for mean wind speed below 15 m s^{-1}. Note that the maximum number of values are at 10 m s^{-1} and 10.5 m s^{-1}, corresponding to wind speeds in the ranges 9.75-10.25 m s^{-1} and 10.25-10.75 m s^{-1}. These values are in the typical rated wind speed region. For instance, the 15 MW IEA reference wind turbine has a rated wind speed of 10.59 m s^{-1} (Gaertner et al., 2020). The sonic σ_u values generally increase with increasing mean wind speed, but with a few exceptions after $\overline{u}$ exceeds 21.5 m s^{-1}, where there are few samples. This pattern also applies to the Mann σ_u, but with even greater variation at the highest wind speeds. The challenge of $(\sigma_u)_{\text{MEF}}$ being underestimated for high wind speeds, as explained in section 6.3, is clearly visible in Fig. 6.13a, where the deviation between Mann and sonic is large. As seen in Fig. 5.9a the US model underestimates σ_u for high mean wind speeds also when all components are known, though to a significantly lesser extent. Estimating σ_u from fitting the US model to S_w seems to work relatively well for mean wind speeds up to 17 m s^{-1}, as the deviation between the Mann and sonic values for these wind speeds are quite small (0.08 m s^{-1} or less). For mean wind speeds exceeding this, the method performs poorly. The Mann and sonic 90th percentile corresponds quite good up to 20 m s^{-1}, but have large deviation from the 90th percentile as given by IEC (Eq. (2.9)). As mentioned in section 5.4 about Fig. 5.9a, Eq. (2.9) might estimate too large values for the 90th percentile. Thus, the large deviation from the Mann 90th percentile to the dashed line does not necessarily mean that the 90th percentile estimated from fitting the US model to S_w is poor. For high mean wind speeds, the Mann error bars are much longer than the sonic error bars, which means that there is larger spread in the $(\sigma_u)_{\text{MEF}}$ estimated from fitting the US model model to S_w than $(\sigma_u)_{\text{sonic\_F}}$ values for high wind speeds. The length of the error bars match quite well for mean wind speeds up to 15 m s^{-1}. For mean wind speeds below 20 m s^{-1}, the difference between the turbulence intensity estimated from the sonic and Mann values is 0.01 or less (Fig. 6.13b). To know whether a deviation of 0.01 is significant when it comes to wind loads on a wind turbine, aeroelastic simulation is needed, which is out of the scope of this thesis.

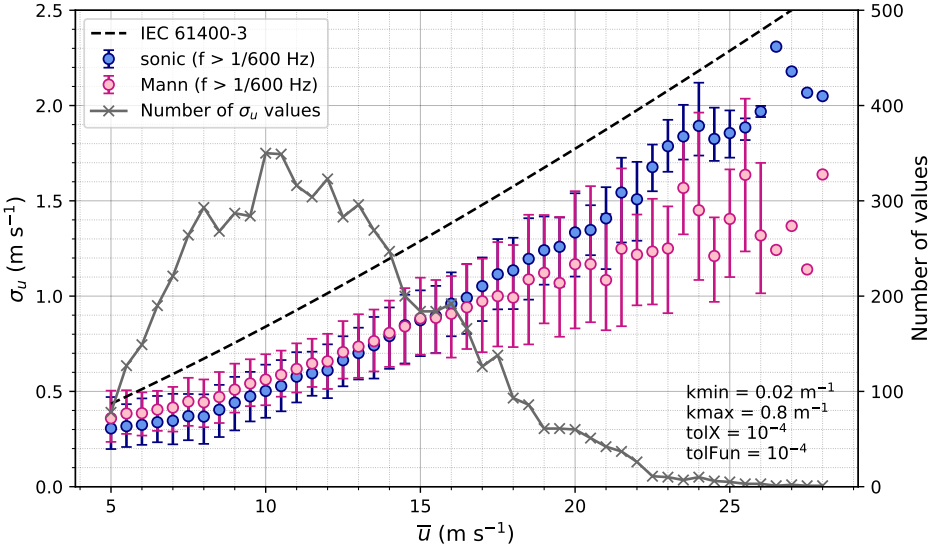

(a) σ_u as a function of $\overline{u}$. The dashed line is calculated using Eq. (2.9).

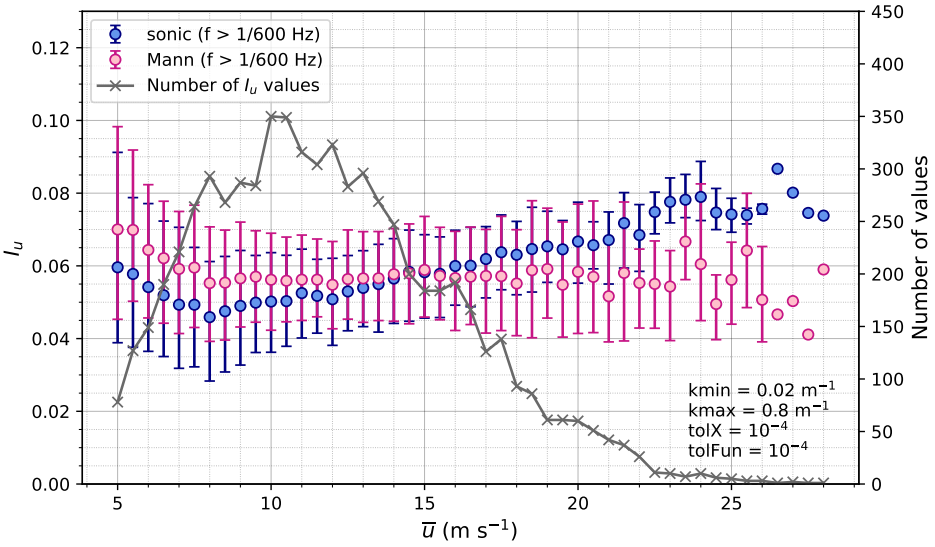

(b) I_u as a function of $\overline{u}$.

Figure 6.13: (a) σ_u and (b) I_u as a function of $\overline{u}$. The bin width is 0.5 m s^{-1}, and the center of each bin is placed at each half m s^{-1}. The error bars mark the 10th and 90th percentile. The blue dots are calculated from $(\sigma_u)_{\text{sonic\_F}}$. The pink dots are calculated from $(\sigma_u)_{\text{MEF}}$ obtained from fitting the US model to S_w. The figure is based on 6665 samples collected during 2007 and 2008 at 81.5 m at FINO1.

Chapter 7

Application to lidar data

The lidar data is measured onshore at Rødby harbour, while FINO1 is located offshore. As there is more turbulence onshore than offshore due to higher surface roughness, the turbulence intensity is expected to be higher at Rødby harbour than at the FINO1 platform. However, the turbulence intensity on the harbour will depend on the analysed sector. To ensure comparability between the turbulence intensity at the two sites (in the sense that the wind comes from similar surface roughness), only wind speeds limited to a sector open to the sea are included from the lidar measurements at the harbour. This corresponds to wind directions of 130° to 295° at Rødby harbour. Since there are no available measurements of the wind direction from the lidar data set, wind directions from NORA3 (Cheynet, 2024) are used to filter the lidar measurements. The NORA3 data set does not provide data at height 80 m, so an average of the wind direction at height 50 m and 100 m are used. This is a simplified approach to determine the wind direction, which may not give precise results. Nevertheless, it is considered sufficient for the intended purpose. The FINO1 (sonic) data only considers wind direction from 190° to 359° to avoid disturbances from the mast. The most frequently observed turbulence intensity measured offshore by the sonic at FINO1 is higher than the most common turbulence intensity measured onshore by the lidar (Fig. 7.1). Spatial averaging of the lidar measurements may explain why the turbulence intensity is higher at the FINO1 platform than at Rødby harbour, which is opposite of expectations.

If the peak of the vertical lidar spectrum had been outside of the k interval affected by spatial averaging, the US model could have been fitted directly

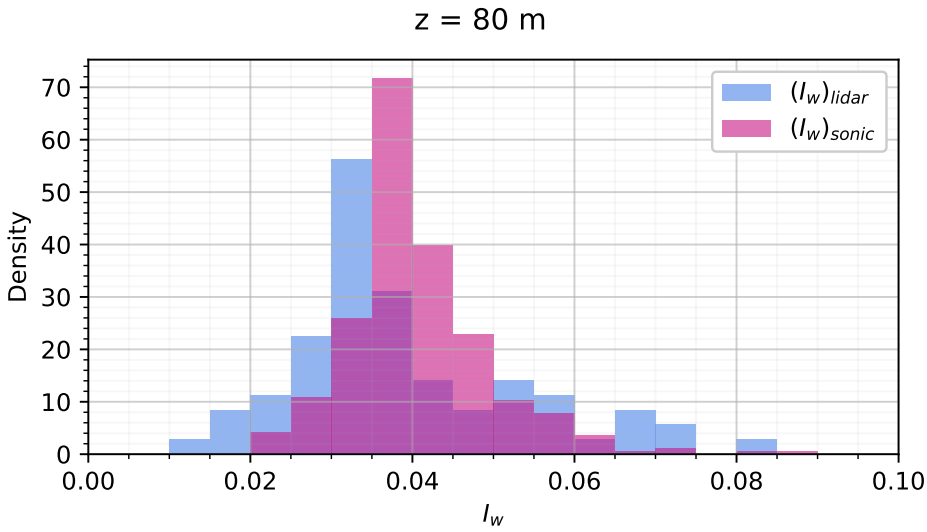

Figure 7.1: Distribution of turbulence intensity. Lidar: based on measurements from a Leosphere WindCube 100S in staring mode at Rødby harbour during November 2022 at height 80.0 m. Only wind directions from 130° to 295° (wind from the ocean) are considered for the lidar data. Sonic: Measurements by a sonic anemometer at the FINO1 platform at 81.5 m during November 2008. For the sonic data, only wind directions from 190° to 359° are considered.

to the spectrum without first attempting deconvolution. Unfortunately, this is not the case, thus spatial averaging correction must be conducted before fitting. Deconvoluting S_w by rearranging Eq. (2.19) does not work well, because the spectral transfer function is close to zero at high wavenumbers, resulting in the spectrum having a rapid growth (blue curve Fig. 7.2). The regularization method in Eq. (2.20) performs poorly because of difficulty in finding a λ that corrects well for high values of k but does not impact low k values (Fig. 7.2 green curve). Therefore, λ is selectively introduced only beyond a certain threshold (k_{lim}), determined empirically in conjunction with λ. $k_{\text{lim}} = 0.13$ m^{-1} and $\lambda = 0.3$ seem appropriate choices, see pink curve Fig. 7.2. This sample is from height 80.0 m, to be comparable to the sonic spectra collected at FINO1. The original lidar spectrum (black curve Fig. 7.2) and the one corrected with λ above k_{lim} (pink curve Fig. 7.2) looks like the convoluted spectrum with probe length 25 m (black curve) and

the original sonic spectrum (pink curve) in Fig. 2.4. This suggests that the very simplified correction method of this thesis may work to some extent. However, since there are no simultaneous point-measurements (for instance by sonic anemometers) from the site, there is no way to validate the lidar measurements or if this simplified deconvolution method is sufficient to correct for spatial averaging.

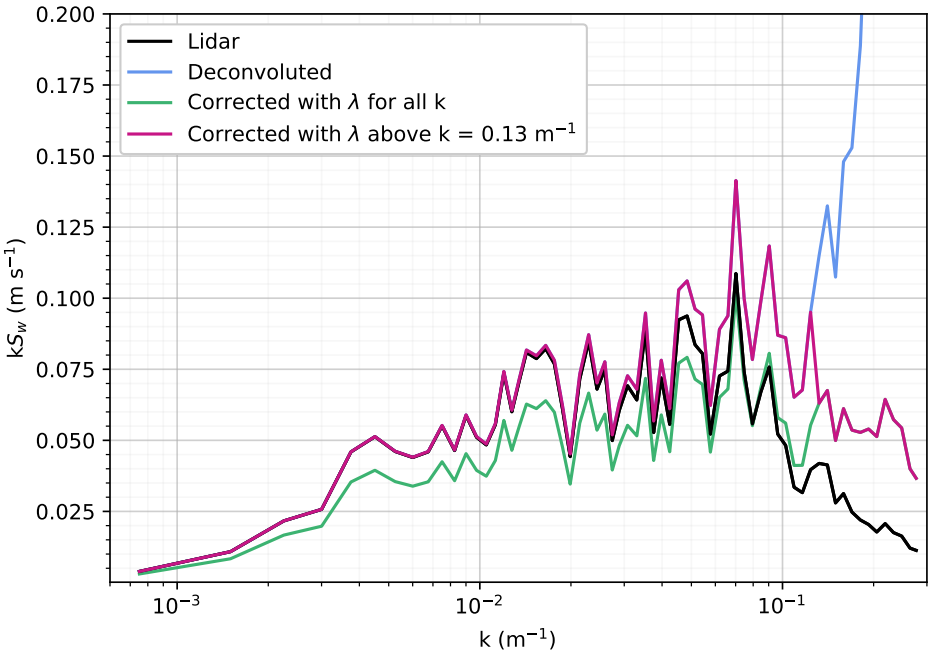

Figure 7.2: S_w obtained from vertical wind measurements taken by a Leosphere WindCube 100S in staring mode with probe length 25 m. The sample is from 15th of November 2022 at 17:47:29 at height 80.0 m, with $\overline{u} = 11.2$ m s^{-1}. The black curve shows the original S_w obtained from spectral analysis of the lidar data. S_w is deconvoluted using Eq. (2.19) (blue curve), and Eq. (2.20) for all k (green curve) and $k > 0.13$ m (pink curve).

Since the sampling rate of the lidar is 1 Hz, the highest measurable frequency (Nyquist frequency) is 0.5 Hz, which is quite different from the sonic anemometer's max frequency of 5 Hz. The sampling period is 25 minutes, meaning that the lowest measurable frequency is 0.001 Hz. As for the FINO1 measurements, this thesis is interested in frequencies above 1/600 Hz (0.002 Hz). The fitting interval of 0.02 m$^{-1} \leq k \leq 0.8$ m^{-1} was found

favorable when testing fitting the US model to the vertical component of the FINO1 data. Because of the low sampling rate of the lidar, the maximum measured k value is lower than the desired $k_{\max} = 0.8\ \mathrm{m}^{-1}$. Therefore, the fitting procedure is tested for $k_{\min} = 0.02\ \mathrm{m\ s}^{-1}$ and using the highest measured k ($0.3\ \mathrm{m}^{-1}$) as $k_{\max}$ on the original lidar spectrum and the corrected (with λ above $k = .13\ \mathrm{m}^{-1}$) spectrum in Fig. 7.2. The initial guess of the model parameters is $\Gamma = 3$, $L = 40$ m and $\alpha\varepsilon^{2/3} = 0.1\ \mathrm{m}^{4/3}\ \mathrm{s}^{-2}$, which is the same as the default for fitting to FINO1 data. $k_{\min} = 0.02\ \mathrm{m\ s}^{-1}$ is too large, because the US model underestimates the spectrum due to the shape of S_w right above $k_{\min}$ (like the case in the right panel of Fig. 6.10). $k_{\min}$ is therefore adjusted to $0.01\ \mathrm{m\ s}^{-1}$. The fitting results are shown in Fig. 7.3, where the upper panel is the original lidar spectrum and the lower panel is the corrected spectrum. There is some difference in the model parameters due to the spectrum shape at high wavenumbers. The US model overestimates S_w slightly for the original lidar spectrum at high wavenumbers. However, spatial averaging is expected at these wavenumbers, so overestimation here may actually give a more realistic PSD than the original lidar spectrum. The fitting to the corrected spectrum looks quite good. The fittings result in $(\sigma_u)_{\mathrm{MEF}} = 0.8\ \mathrm{m\ s}^{-1}$ when fitted to the original lidar S_w and $(\sigma_u)_{\mathrm{MEF}} = 1.1\ \mathrm{m\ s}^{-1}$ when fitted to the corrected spectrum. Again, the accuracy of $(S_u)_{\mathrm{MEF}}$ and $(\sigma_u)_{\mathrm{MEF}}$ cannot be verified because of lack of sonic data. The mean wind speed is $11.2\ \mathrm{m\ s}^{-1}$, which is in a range where there is good correspondence between $(\sigma_u)_{\mathrm{MEF}}$ and $(\sigma_u)_{\mathrm{sonic\_F}}$ in Fig. 6.13a.

Fig. 7.4 shows the vertical profile of $\overline{u}$, σ_w and I_w from the sample corresponding to the vertical wind spectrum in Fig. 7.2 and Fig. 7.3. The Leosphere Windcube 100S had a dead zone of 50 m, and the measurements stopped at 220 m for this sample, which is quite low. The mean wind speed increases with height, and the standard deviation and turbulence intensity of the vertical component decrease with height except for between 110 m and 140 m. The stability of the atmosphere is unknown, but the mean wind speeds are relatively high. Fig. 7.5 shows σ_u (left panel) and I_u (right panel) calculated from σ_w using different methods. The orange curve results from Eq. (2.22) (Engineering Sciences Data Unit (ESDU), 2001) with $h = 225$ m (found from inspection of the lidar measurements). The purple curve is calculated using Eq. (2.21) (IEC 61400-1, 2005). The ESDU equation holds for neutral atmosphere (strong winds). At hub height the difference between the two standards are large, which means that the choice of standard has a

great impact on σ_u and I_u. Fig. 7.5 also includes σ_u and I_u obtained from fitting the US model to S_w using both the original lidar spectrum (black curve) and a corrected spectrum (pink curve). For $z = 80.0$ m the original lidar spectrum corresponds to the black curve in Fig. 7.2 and Fig. 7.3 (upper panel). The corrected spectrum is deconvoluted and corrected with $\lambda = 0.3$ for $k > 0.13$ m^{-1} using Eq. (2.20), which for $z = 80.0$ m corresponds to the pink curve in Fig. 7.2 and Fig. 7.3 (lower panel). Note that in Fig. 7.5, the integration (when estimating σ_u from fitting the US model to S_w) is performed over all frequencies included in the original spectral analysis of the lidar measurements, not just above 1/600 Hz (as it is in Fig. 7.3). This is done to ensure that the values obtained from fitting are comparable to the ESDU and IEC equations which are based on σ_w measurements with averaging period of 25 minutes, thus including frequencies below 1/600 Hz. While the ESDU and IEC equations result in rather smooth profiles, with the ESDU profiles decreasing with height, σ_u obtained from fitting the US model to the original and corrected S_w give large variations in the profiles. This may indicate that the method works bad, especially that the corrected deconvolution method is insufficient. λ and k_{lim} are empirically adjusted to S_w at height 80.0 m. From Fig. 7.5 it can be seen that the pink curve is close to the ESDU curve at this height. The chosen λ and k_{lim} may not suit the spectra at the other heights, and should probably be adjusted for each spectrum. This emphasizes the shortfall of the correction method of this thesis. It is also worth noting that due to lack of σ_u measurements, it is unknown whether the ESDU or IEC equation actually give good σ_u estimations.

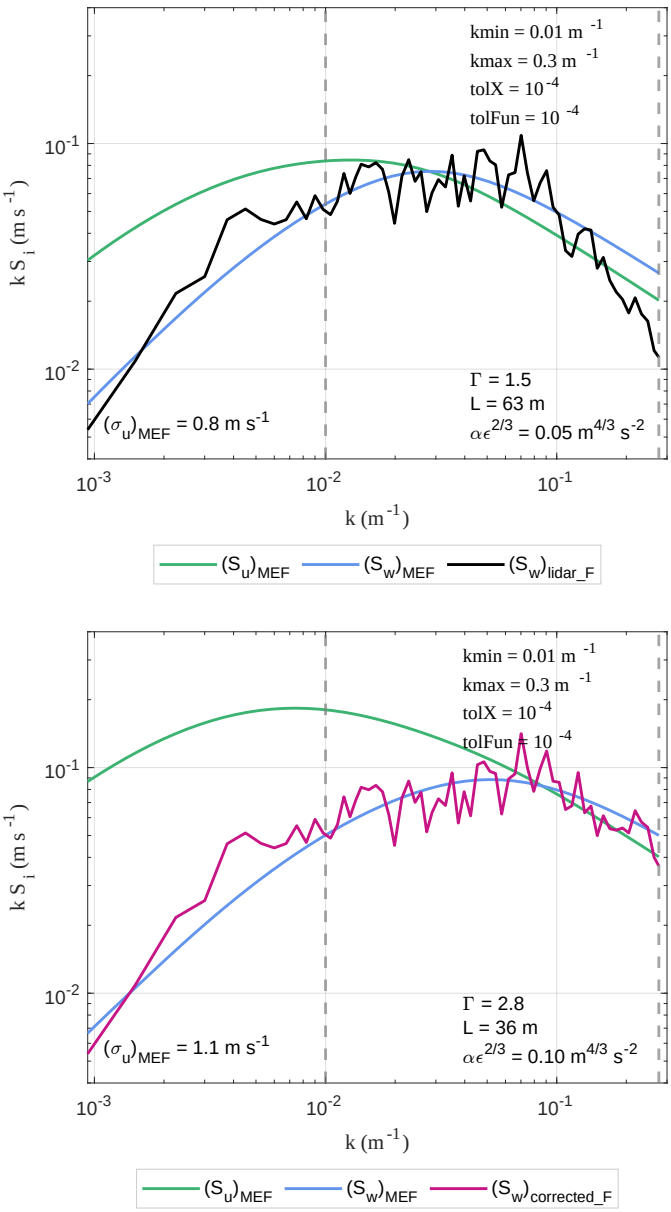

Figure 7.3: The US model fitted to S_w obtained from vertical velocity measurements by a Leosphere WindCube 100S (probe volume length 25 m) in staring mode 15th of November 2022 at 17:47:29 at 80.0 m, with $\overline{u} = 11.2$ m s^{-1}. Upper panel: $(S_w)_{\text{lidar}}$ is from the original spectral analysis of the lidar measurements. Lower panel: the original lidar spectrum is deconvoluted and corrected using Eq. (2.20) with $\lambda = 0.3$ for $k > 0.13$ m.

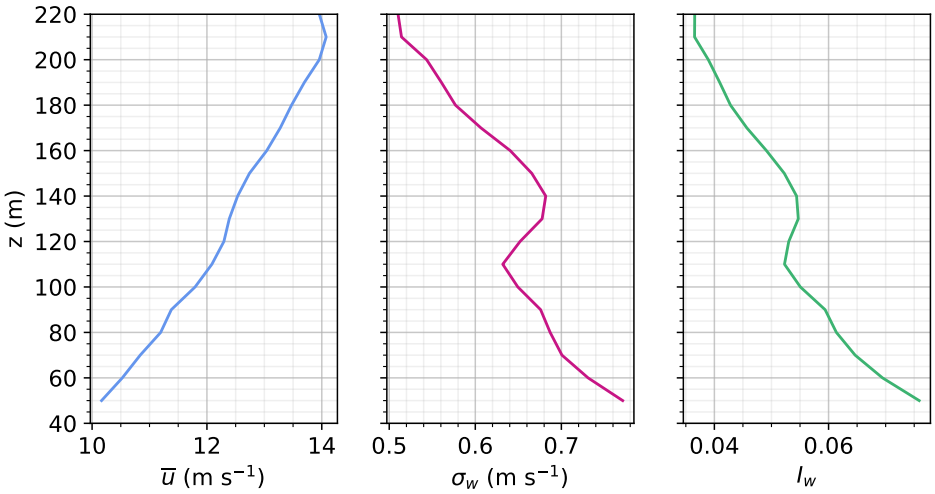

Figure 7.4: Data collected by a Leosphere WindCube 100S (probe length 25 m) 15th of November 2022 at 17:47:29 at Rødby harbour. Left panel: profile of $\overline{u}$ collected in 4-beam DBS mode. Middle panel: profile of σ_w collected in vertical staring mode. Right panel: the resulting $I_w = \sigma_w/\overline{u}$.

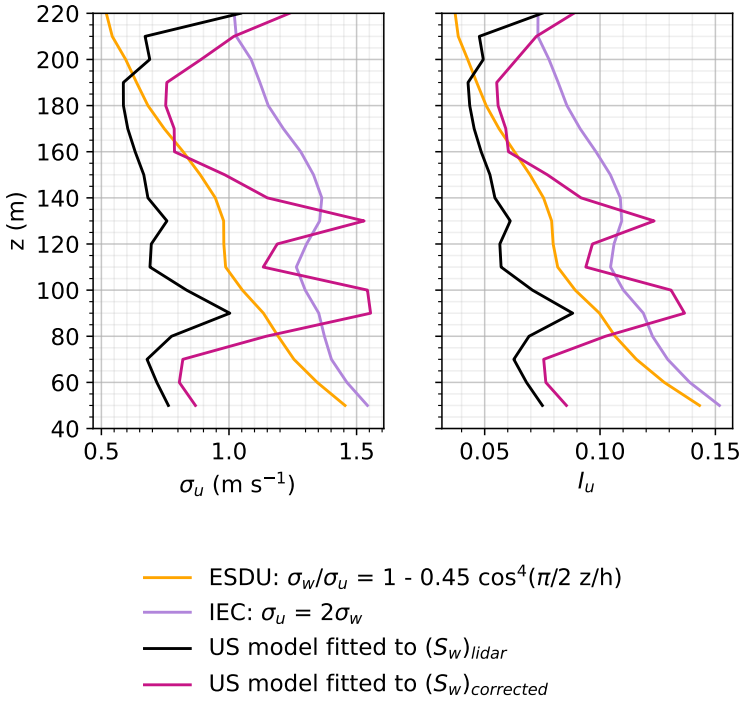

Figure 7.5: Profiles of σ_u (left panel) and I_u (right panel) estimated from vertical velocity measurements by a Leosphere WindCube 100S using Eq. (2.22) (orange curve), Eq. (2.21) (purple curve) and fitting the US model to $(S_w)_{\text{lidar}}$ (black curve) and $(S_w)_{\text{corrected}}$ (pink curve). $(S_w)_{\text{corrected}}$ is calculated using Eq. (2.20) with applying $\lambda = 0.3$ for $k > 0.13$ m^{-1}. The sample is collected 15th of November 2022 at 17:47:29 at Rødby harbour.

Chapter 8

Conclusions

The thesis investigated the feasibility of deducing the along-wind spectrum and the resulting σ_u from measurements of the vertical wind speed combined with numerical modeling, using the uniform shear (US) model (Mann, 1994). The method for fitting the US model to data was tested on measurements taken by sonic anemometer at 81.5 m at the FINO1 platform for two different cases: 1) all velocity components were known, and 2) only S_w was known. The method was also briefly tested on vertical velocity measurements taken by a Leosphere WindCube 100S, which included a novel aspect of correcting for spatial averaging.

8.1 Evaluation of thesis objectives

Fitting the US model to all velocity components worked well for all the tested k intervals and iteration tolerances, as indicated by the agreement between the resulting $(\sigma_u)_{\text{Mann}}$ and $(\sigma_u)_{\text{targ}}$. After extending the fitting results and only including $f > 1/600$ Hz, the best agreement between $(\sigma_u)_{\text{MEF}}$ and $(\sigma_u)_{\text{sonic\_F}}$ was obtained using a relatively broad k interval in the fitting. The extended and filtered results were especially good using the fitting inputs $k_{\text{min}} = 0.001\ \text{m}^{-1}$, $k_{\text{max}} = 1.0\ \text{m}^{-1}$ and iteration tolerances of 10^{-3}, which resulted in good correspondence between $(\sigma_u)_{\text{MEF}}$ and $(\sigma_u)_{\text{sonic\_F}}$ for all stabilities. Thus, the model parameters obtained in these fittings were considered reliable estimations, against which parameters from fittings to the vertical component were later compared.

The results revealed that the accuracy of fitting the US model to only

the vertical component was affected by the k interval used in the fitting. Encountering local minima during the optimization process, rather than the desired global minima, posed a significant challenge. This was particularly evident when attempting to fit the US model to S_w using the inputs $k_{\min} = 0.001$ m^{-1}, $k_{\max} = 1.0$ m^{-1}, and iteration tolerances 10^{-3}. In many cases, this led to overestimation of $(S_u)_{\mathrm{MEF}}$ and consequently $(\sigma_u)_{\mathrm{MEF}}$. Using tolerances of 10^{-4} and adjusting the initial guess of $\alpha\varepsilon^{2/3}$ from 0.1 m$^{4/3}$ s^{-2} to 0.03 m$^{4/3}$ s^{-2} led to some improvement. However, using the fitting inputs $k_{\min} = 0.02$ m s^{-1}, $k_{\max} = 0.8$ m s^{-1} and tolerances 10^{-4} gave better agreement between $(\sigma_u)_{\mathrm{MEF}}$ and $(\sigma_u)_{\mathrm{sonic\_F}}$. It seemed like encountering local minimum was less of an issue for this narrow k interval. Nonetheless, selecting such a narrow interval could pose challenges if the spectrum within this range exhibits a shape that diverges from the characteristics observed outside of the interval. The estimation of $\alpha\varepsilon^{2/3}$ from fitting the US model to S_w with $k_{\min} = 0.02$ m s^{-1}, $k_{\max} = 0.8$ m s^{-1} and iteration tolerances 10^{-4} was quite good. The results revealed that the deviation between $(\sigma_u)_{\mathrm{sonic\_F}}$ and $(\sigma_u)_{\mathrm{MEF}}$ obtained from such fittings was only 0.08 m s^{-1} or less for mean wind speeds up to 17 m s^{-1}. For turbulence intensity, this corresponded to a difference of 0.01 or less. This implies that the along-wind spectrum can quite well be deduced from measurements of only the vertical component for mean wind speeds up to this. At higher mean wind speeds, the PSD values are so large that poor estimations of L and Γ affect the generated along-wind spectrum and therefore also σ_u significantly. Particularly, underestimation of Γ seemed to be a challenge for high mean wind speeds. Thus, the results indicate that for very high mean wind speeds, neither the along-wind spectrum nor σ_u could accurately be retrieved from vertical measurements only using the method of this thesis.

The height of the mast at FINO1 is not sufficient for drawing conclusions regarding the accuracy of estimating σ_u from fitting the US model to S_w at altitudes relevant to wind turbine operation. The US model was fitted to the vertical wind spectrum obtained from lidar measurements, both the original spectrum and one that had undergone an attempt of correcting for the spatial averaging effect. The correction method introduced a constant, λ , beyond a threshold $k_{\min}$, with both values determined empirically using a spectrum at a height of 80.0 m. Validation of the fitting results and the correction attempt presented in this thesis was not possible due to lack of available point measurements. However, large variation with height in the estimated

σ_u from the corrected spectrum implied that the correction method did not work well on all spectra.

8.2 Future work

To properly test the method on lidar measurements, a robust approach for correcting the spatial averaging is first required. Therefore, it is recommended that future work focuses on developing reliable methods to correct for spatial averaging. Alternative ways to estimate Γ would be interesting, as this model parameter seems to be the most challenging to estimate from measurements of only the vertical component. For future work, the author would also recommend using a higher lower limit for Γ for high wind speeds, to avoid some of the underestimation.

Appendix A

Extended comparison

The figures compare $(\sigma_u)_{\mathrm{ME}}$ and $(\sigma_u)_{\mathrm{sonic}}$, thus including frequencies below 1/600 Hz. $(\sigma_u)_{\mathrm{ME}}$ is calculated using Eq. (4.4) with $(S_u)_{\mathrm{ME}}$ and $(f)_{\mathrm{ME}}$ obtained from fitting the US model to data of either all velocity components or only S_w, using different k_{min}, k_{max} and tolerances. $(\sigma_u)_{\mathrm{sonic}}$ is obtained from Eq. (4.3). The figures are based on 381 samples obtained from measurements at 81.5 m at FINO1 in January 2008. The dashed line shows $y = x$.

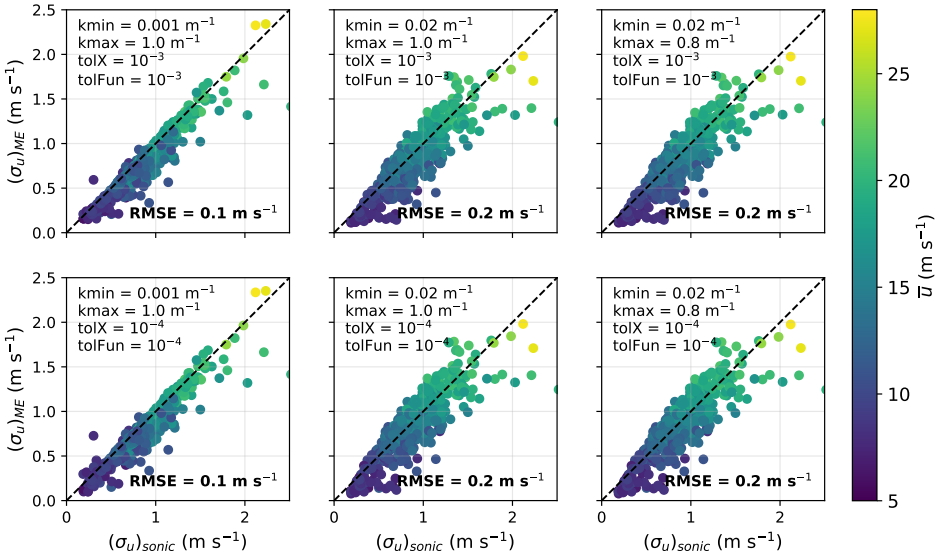

Figure A.1: The US model fitted to all components.

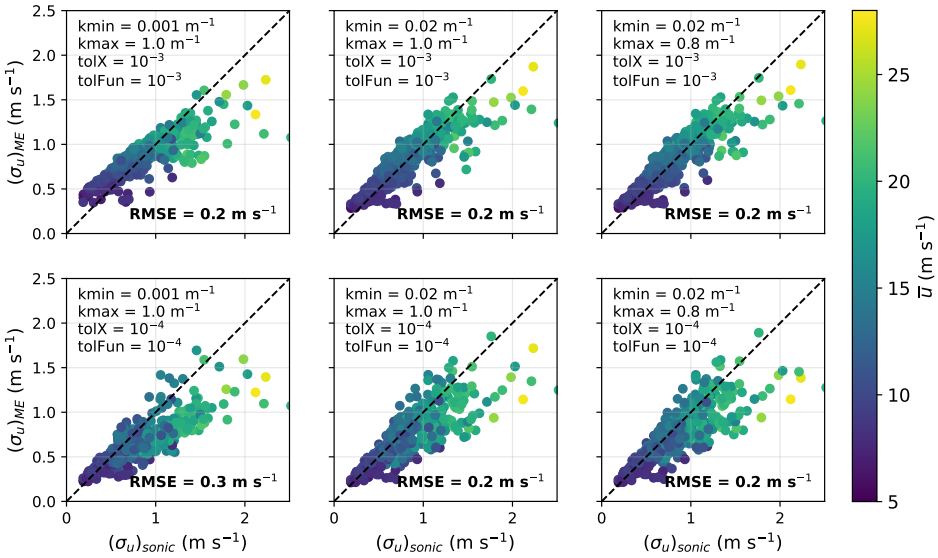

Figure A.2: The US model fitted to S_w.

Appendix B

Filtered comparison

The figures compare $(\sigma_u)_{\mathrm{MEF}}$ and $(\sigma_u)_{\mathrm{sonic\_F}}$, thus only including frequencies above 1/600 Hz. $(\sigma_u)_{\mathrm{sonic\_F}}$ is obtained from Eq. (4.5). $(\sigma_u)_{\mathrm{MEF}}$ is calculated using Eq. (4.6) with $(S_u)_{\mathrm{MEF}}$ and $(f)_{\mathrm{MEF}}$ obtained from fitting the US model to data of either all velocity components or only S_w. If not otherwise specified, the initial guess is $[\Gamma,\ L,\ \alpha\varepsilon^{2/3}]$ = [3, 40, 0.1]. The figures are based on 1871 stable, 2007 neutral and 2787 unstable samples collected by sonic anemometer at height 81.5 m at FINO1 during 2007 and 2008. The dashed line shows $y = x$.

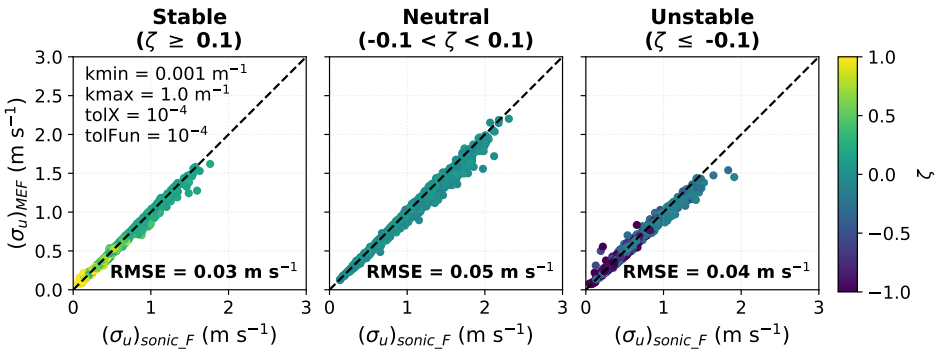

(a) Scatter plot with colors showing stability.

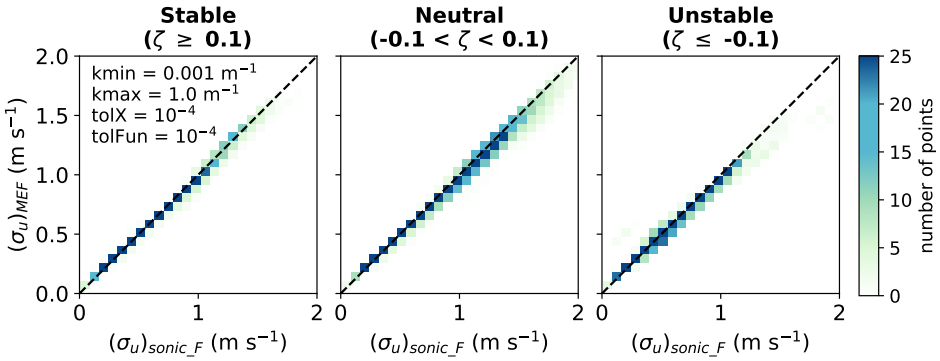

(b) Density plot with colors showing number of points.

Figure B.1: The US model fitted to all components.

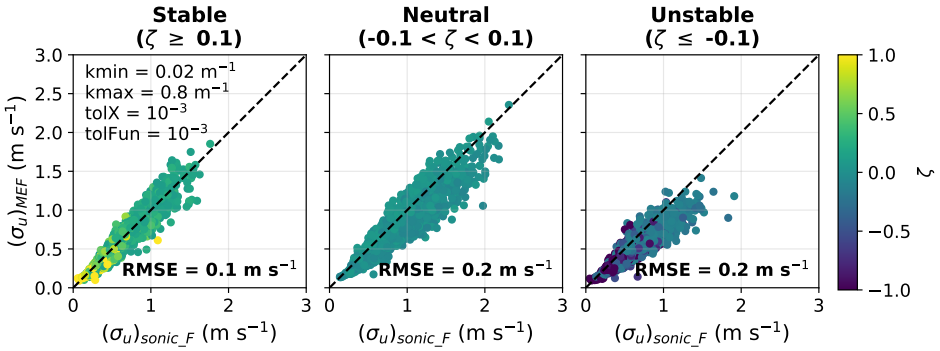

(a) Scatter plot with colors showing stability.

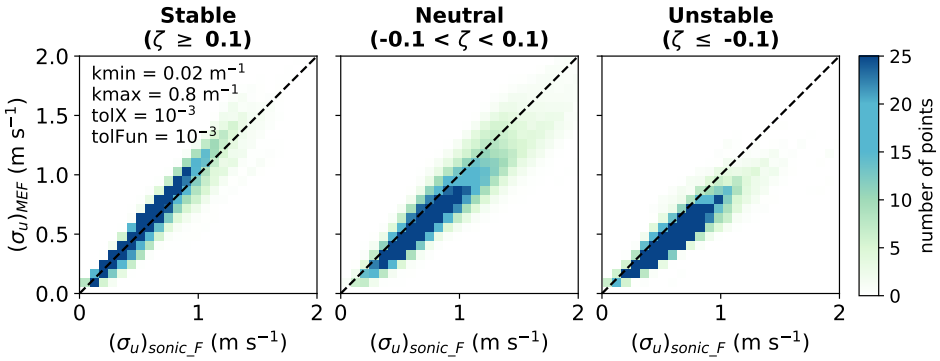

(b) Density plot with colors showing number of points.

Figure B.2: The US model fitted to all components.

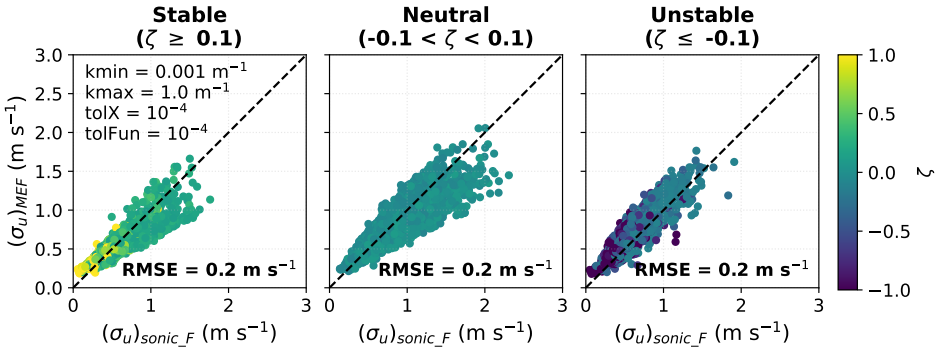

(a) Scatter plot with colors showing stability.

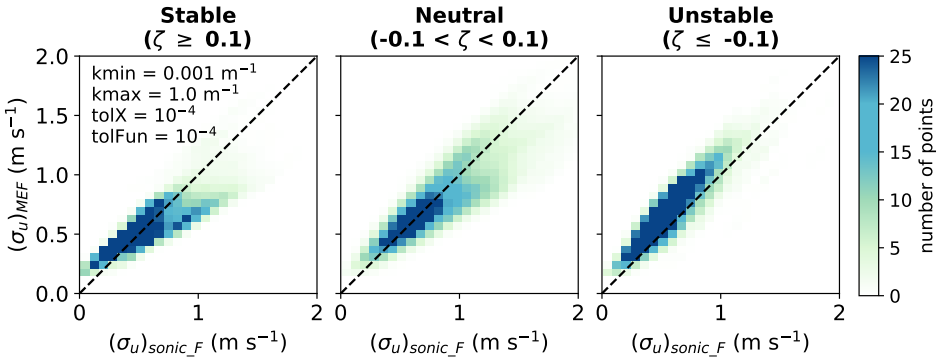

(b) Density plot with colors showing number of points.

Figure B.3: The US model fitted to S_w.

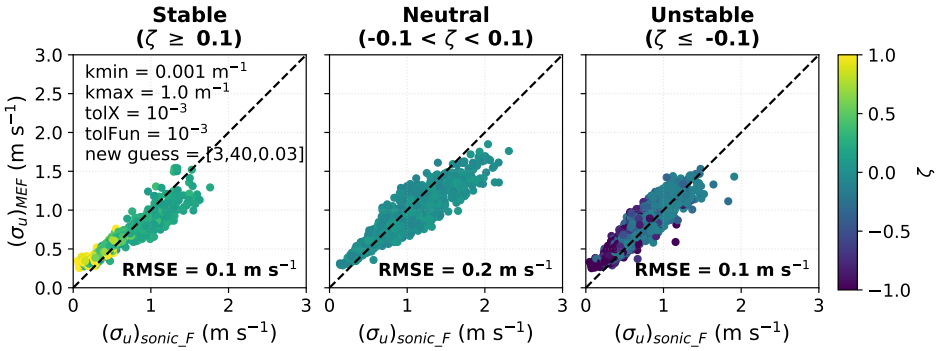

(a) Scatter plot with colors showing stability.

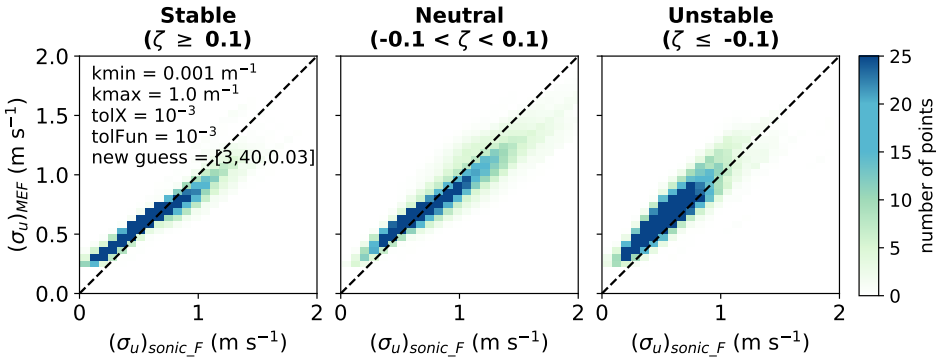

(b) Density plot with colors showing number of points.

Figure B.4: The US model fitted to S_w.

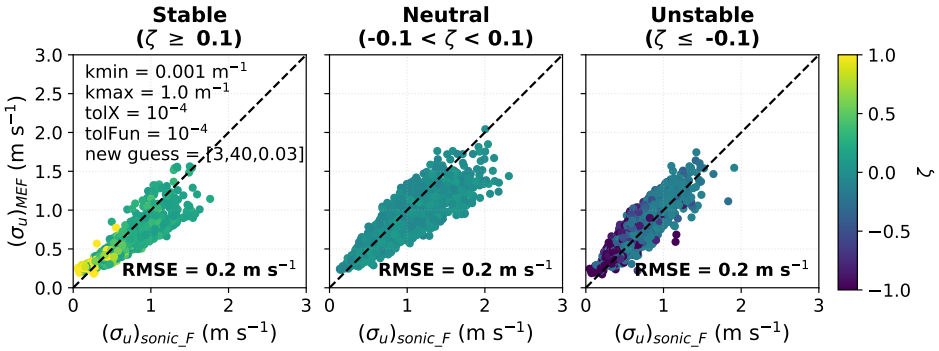

(a) Scatter plot with colors showing stability.

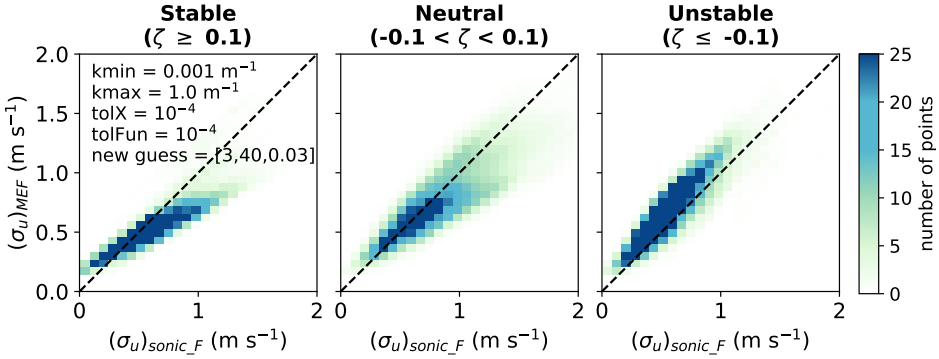

(b) Density plot with colors showing number of points.

Figure B.5: The US model fitted to S_w.

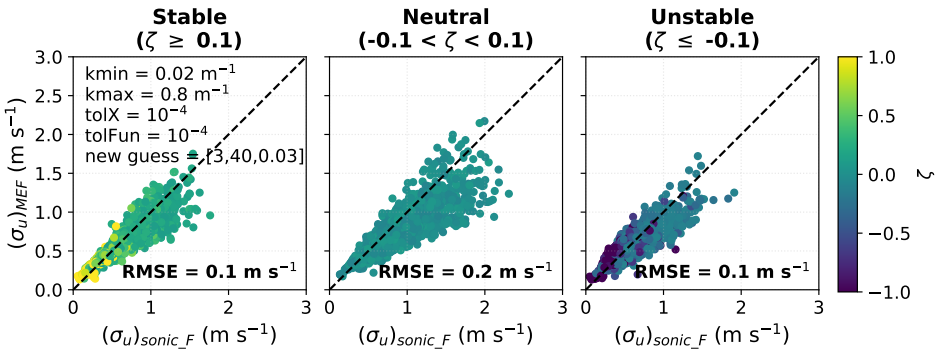

(a) Scatter plot with colors showing stability.

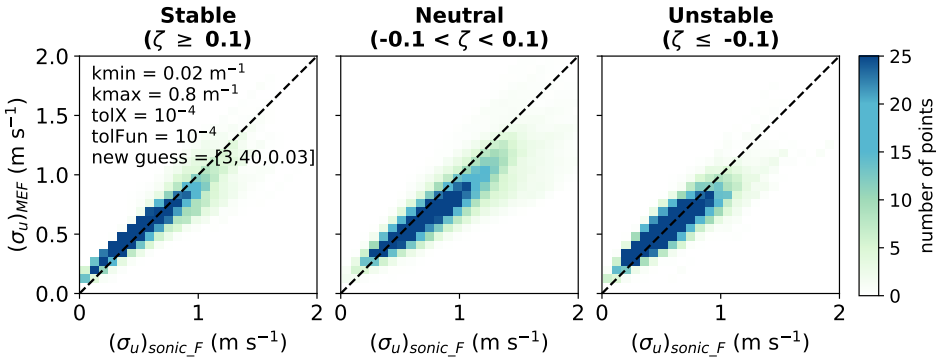

(b) Density plot with colors showing number of points.

Figure B.6: The US model fitted to S_w.

Appendix C

Model parameters

The fogures compare the model parameters Γ (left panel), L (middle panel) and $\alpha\varepsilon^{2/3}$ (right panel) obtained from fitting the US model to data using different inputs (written under ”X-axis” and ”Y-axis”). The figures are based on 6665 samples collected during 2007 and 2008 at 81.5 m at FINO1. The dashed line shows $y = x$.

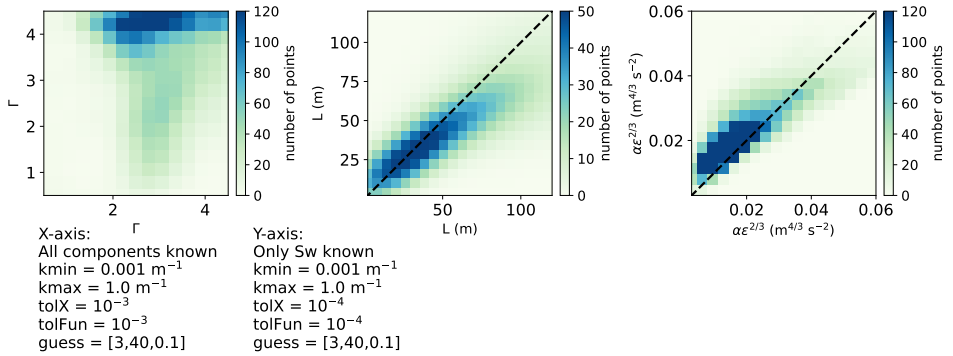

Figure C.1

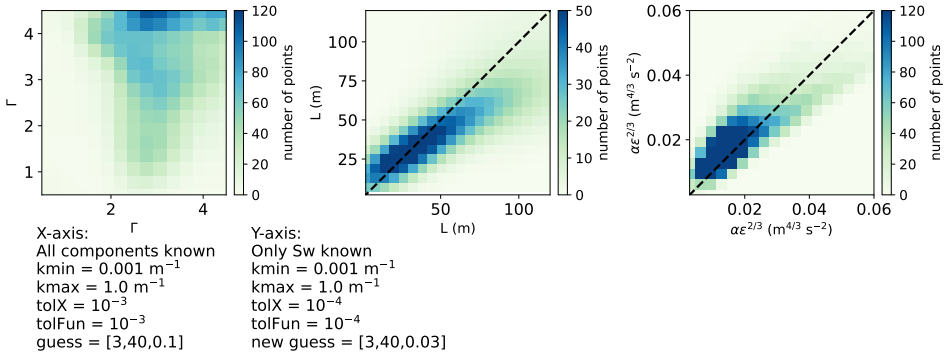

Figure C.2

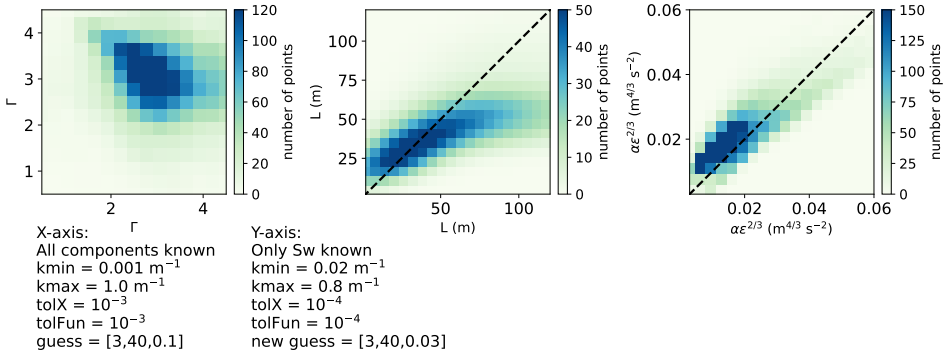

Figure C.3

Appendix D

Comparing model parameters with mean wind speed

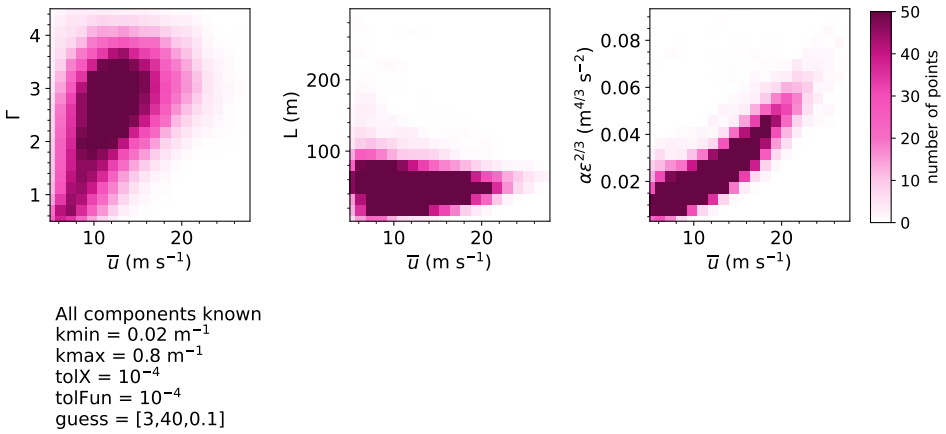

Figure D.1: Relating the model parameters Γ (left panel), L (middle panel) and $\alpha\varepsilon^{2/3}$ (right panel) to $\overline{u}$. The model parameters are obtained from fitting the US model to all wind components. ”guess” refers to the initial guess of the model parameters, and is on the form [Γ, L, $\alpha\varepsilon^{2/3}$]. The figure is based on 6665 samples collected during 2007 and 2008 at 81.5 m at FINO1.

Appendix E

Comparison with IEC 61400-3

σ_u as a function of $\overline{u}$. The bin width is 0.5 m s^{-1}, and the center of each bin is placed at each half m s^{-1}. The error bars mark the 10th and 90th percentile. The dashed line is calculated using Eq. (2.9). The blue dots corresponds to $(\sigma_u)_{\text{sonic\_F}}$. The pink dots corresponds to $(\sigma_u)_{\text{MEF}}$ obtained from fitting the US model to S_w only. If not otherwise specified, the initial guess is [Γ, L, $\alpha\varepsilon^{2/3}$] = [3, 40, 0.1]. The figures are based on 6665 samples collected during 2007 and 2008 at 81.5 m at FINO1.

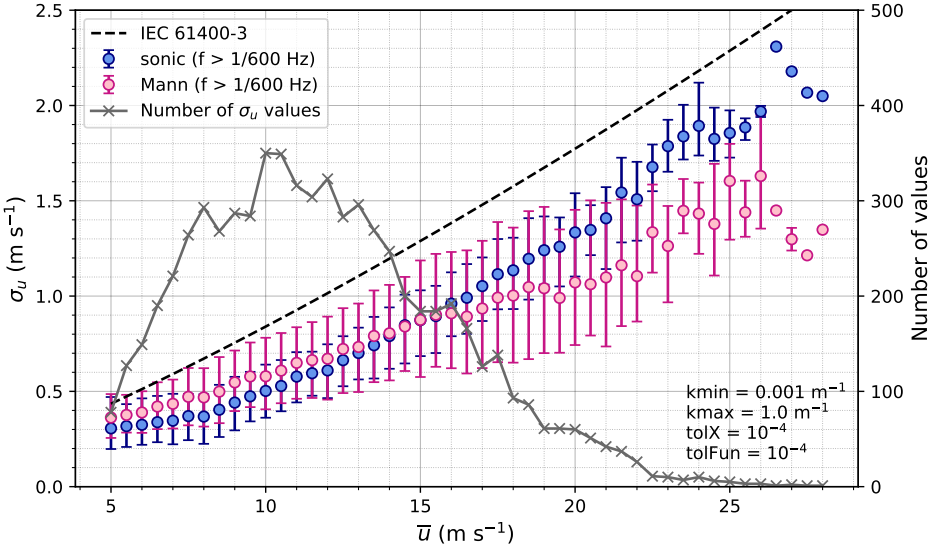

Figure E.1

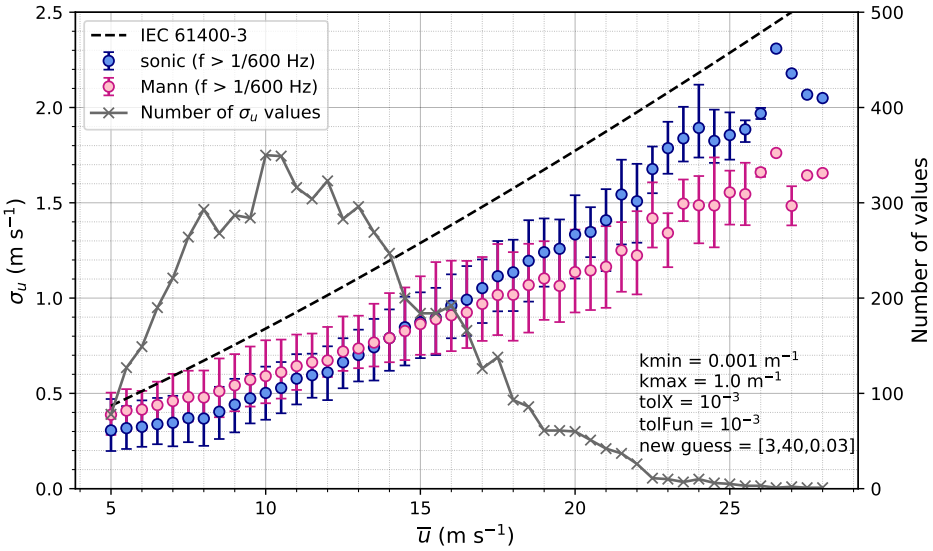

Figure E.2

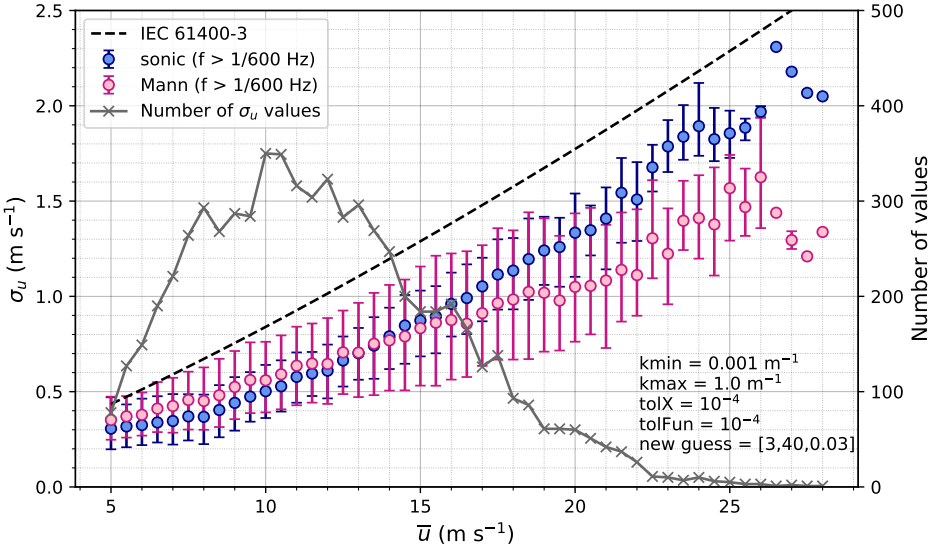

Figure E.3

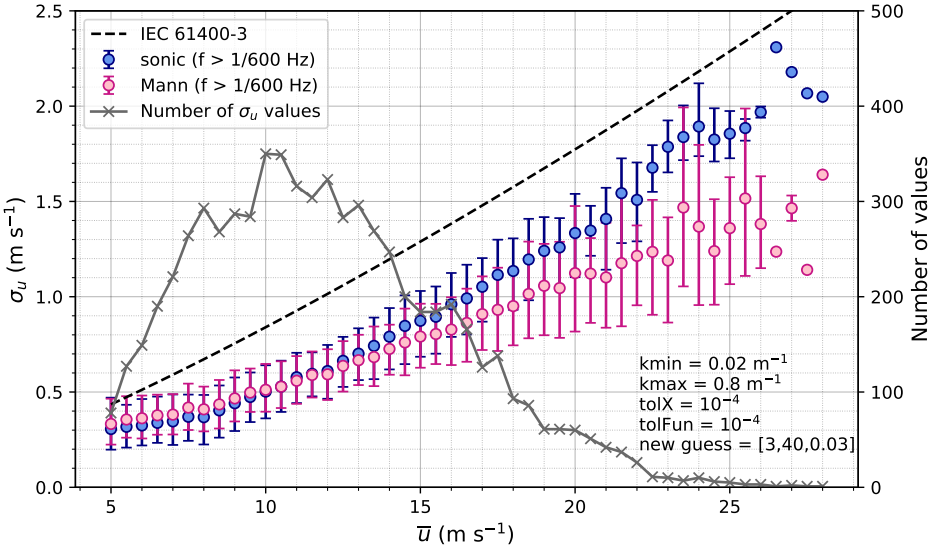
IEC 61400-3
sonic (f > 1/600 Hz)
Mann (f > 1/600 Hz)
Number of σ_u values
kmin = 0.02 m^{-1}
kmax = 0.8 m^{-1}
tolX = 10^{-4}
tolFun = 10^{-4}
new guess = [3,40,0.03]
σ_u (m s^{-1})
$\overline{u}$ (m s^{-1})
Number of values
0.0
0.5
1.0
1.5
2.0
2.5
5
10
15
20
25
0
100
200
300
400
500

Figure E.4

Appendix F

Wind spectrum

Similar figure as Fig. 6.6, but the right panel having tolerances of 10^{-4} instead of 10^{-3}.

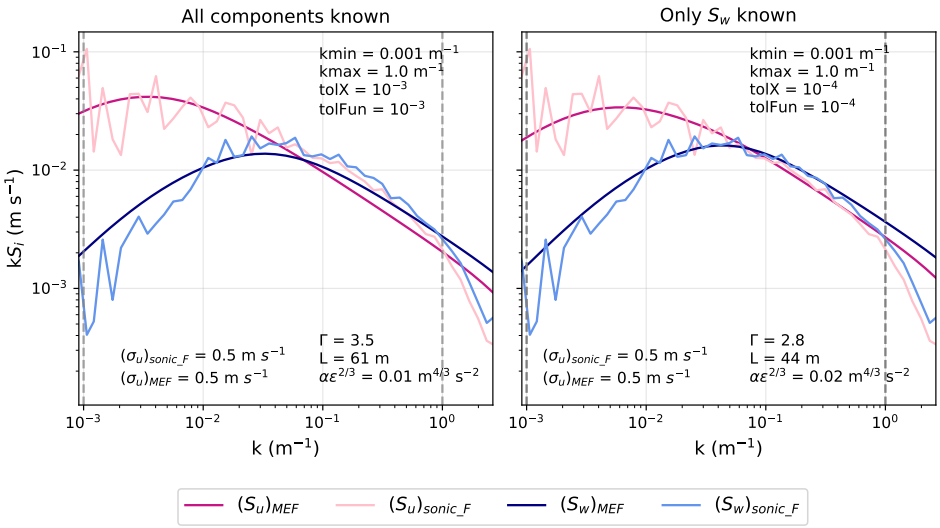

Figure F.1: Sonic wind spectra obtained from measurements at 81.5 m height at the FINO1 platform in February 2008 ($\zeta = 0.03$ (neutral), $\overline{u} = 11.5$ m s^{-1}). The vertical dashed lines show $k_{\min}$ and $k_{\max}$ used when fitting the US model to all wind components (left panel) and only S_w (right panel).

Bibliography

Bendat, J. S., & Piersol, A. G. (1980). *Engineering applications of correlation and spectral analysis*. New York: John Wiley & Sons, Inc.

Cariou, J. P. (2013). *Remote Sensing for Wind Energy, chap. 5 - Pulsed Lidars*. Technical Report DTU Wind Energy-E-Report-0029(EN) DTU.

Cheynet, E. (2016). *Wind-induced vibrations of a suspension bridge: A case study in full-scale*. Doctoral thesis University of Stavanger, Norway. URL: https://uis.brage.unit.no/uis-xmlui/handle/11250/2425472 accepted: 2016-12-19T13:33:26Z ISBN: 9788276446913 ISSN: 1890-1387.

Cheynet, E. (2022). Fitting the Uniform Shear Model to real data. URL: https://se.mathworks.com/matlabcentral/fileexchange/73126-fitting-the-uniform-shear-model-to-real-data.

Cheynet, E. (2024). Gridded NORA3 data: automated and remote data extraction. URL: https://github.com/ECheynet/NORA3/releases/tag/v1.3.

Cheynet, E., Jakobsen, J. B., & Reuder, J. (2018). Velocity Spectra and Coherence Estimates in the Marine Atmospheric Boundary Layer. *Boundary-Layer Meteorology*, *169*, 429–460. URL: https://doi.org/10.1007/s10546-018-0382-2. doi:10.1007/s10546-018-0382-2.

Cheynet, E., Jakobsen, J. B., Snæbjörnsson, J., Reuder, J., Kumer, V., & Svardal, B. (2017). Assessing the potential of a commercial pulsed lidar for wind characterisation at a bridge site. *Journal of Wind Engineering and Industrial Aerodynamics*, *161*, 17–26. URL: https://www.sciencedirect.com/science/article/pii/S016761051530115X. doi:10.1016/j.jweia.2016.12.002.

Cheynet, E., Li, L., & Jiang, Z. (2024). Metocean conditions at two Norwegian sites for development of offshore wind farms. *Renewable Energy*, *224*, 120184. URL: https://www.sciencedirect.com/science/article/pii/S0960148124002490. doi:https://doi.org/10.1016/j.renene.2024.120184.

Chougule, A. S. (2013). *Infulence of atmospheric stability on the spatial structure of turbulence*. Ph.D. thesis Technical University of Denmark Kgs. Lyngby.

Colone, L., Natarajan, A., & Dimitrov, N. (2018). Impact of turbulence induced loads and wave kinematic models on fatigue reliability estimates of offshore wind turbine monopiles. *Ocean Engineering*, *155*, 295–309. URL: https://www.sciencedirect.com/science/article/pii/S002980181830194X. doi:10.1016/j.oceaneng.2018.02.045.

Davenport, A. G. (1964). The Buffeting of Large Superficial Structures by Atmospheric Turbulence. *Annals of the New York Academy of Sciences*, *116*, 135–160. URL: https://onlinelibrary.wiley.com/doi/abs/10.1111/j.1749-6632.1964.tb33943.x. doi:10.1111/j.1749-6632.1964.tb33943.x. _eprint: https://onlinelibrary.wiley.com/doi/pdf/10.1111/j.1749-6632.1964.tb33943.x.

D'Errico, J. (2012). inpaint_nans. URL: https://se.mathworks.com/matlabcentral/fileexchange/4551-inpaint_nans.

EERE (2023). Wind Turbines: the Bigger, the Better. URL: https://www.energy.gov/eere/articles/wind-turbines-bigger-better.

Engineering Sciences Data Unit (ESDU) (2001). Characteristics of Atmospheric Turbulence Near the Ground. Part II: Single Point Data for Strong Winds (Neutral Atmosphere). URL: https://www.esdu.com/cgi-bin/ps.pl?t=doc&p=esdu_85020g published: Engineering Sciences Data Unit.

Ernst, B., & Seume, J. R. (2012). Investigation of Site-Specific Wind Field Parameters and Their Effect on Loads of Offshore Wind Turbines.

Energies, *5*, 3835–3855. URL: https://www.mdpi.com/1996-1073/5/10/3835. doi:10.3390/en5103835. Number: 10 Publisher: Molecular Diversity Preservation International.

Gaertner, E., Rinker, J., Sethuraman, L., Zahle, F., Anderson, B., Barter, G., Abbas, N., Meng, F., Bortolotti, P., Skrzypinski, W., & others (2020). *IEA Wind TCP Task 37: Definition of the IEA 15-Megawatt Offshore Reference Wind Turbine*. Technical Report NREL/TP-5000-75698 National Renewable Energy Laboratory Golden, CO, USA. URL: https://www.nrel.gov/docs/fy20osti/75698.pdf.

Gottschall, J., Gribben, B., Stein, D., & Würth, I. (2017). Floating lidar as an advanced offshore wind speed measurement technique: current technology status and gap analysis in regard to full maturity. *WIREs Energy and Environment*, *6*, e250. URL: https://onlinelibrary.wiley.com/doi/abs/10.1002/wene.250. doi:10.1002/wene.250. _eprint: https://onlinelibrary.wiley.com/doi/pdf/10.1002/wene.250.

Hoegh-Guldberg, O., Jacob, D., Taylor, M., Guillén Bolaños, T., Bindi, M., Brown, S., Camilloni, I. A., Diedhiou, A., Djalante, R., Ebi, K., & others (2019). The human imperative of stabilizing global climate change at 1.5 C. *Science*, *365*, eaaw6974. Publisher: American Association for the Advancement of Science.

Van der Hoven, I. (1957). Power Spectrum of Horizontal Wind Speed in the Frequency Range From 0.0007 to 900 Cycles Per Hour. *Journal of the Atmospheric Sciences*, *14*, 160–164. URL: https://journals.ametsoc.org/view/journals/atsc/14/2/1520-0469_1957_014_0160_psohws_2_0_co_2.xml. doi:10.1175/1520-0469(1957)014<0160:PSOHWS>2.0.CO;2. Publisher: American Meteorological Society Section: Journal of the Atmospheric Sciences.

IEA (2021). *Net Zero by 2050 - A Roadmap for the Global Energy Sector*. Technical Report International Energy Agency. URL: https://www.iea.org/reports/net-zero-by-2050.

IEA (2023). Wind. URL: https://www.iea.org/energy-system/renewables/wind.

IEC 61400-1 (2005). *Wind Turbines Part 1: Design Requirements*. Technical Report International Electrotechnical Committee Geneva, Switzerland.

IEC 61400-3 (2009). *Wind turbines Part 3: Design requirements for offshore wind turbines*. Technical Report International Electrotechnical Committee Geneva, Switzerland.

Jacobsen, A., & Godvik, M. (2021). Influence of wakes and atmospheric stability on the floater responses of the Hywind Scotland wind turbines. *Wind Energy*, *24*, 149–161. URL: https://onlinelibrary.wiley.com/doi/abs/10.1002/we.2563. doi:10.1002/we.2563. _eprint: https://onlinelibrary.wiley.com/doi/pdf/10.1002/we.2563.

Khintchine, A. (1934). Korrelationstheorie der stationären stochastischen Prozesse. *Mathematische Annalen*, *109*, 604–615. URL: https://doi.org/10.1007/BF01449156. doi:10.1007/BF01449156.

Liu, Z., Barlow, J. F., Chan, P.-W., Fung, J. C. H., Li, Y., Ren, C., Mak, H. W. L., & Ng, E. (2019). A Review of Progress and Applications of Pulsed Doppler Wind LiDARs. *Remote Sensing*, *11*, 2522. URL: https://www.mdpi.com/2072-4292/11/21/2522. doi:10.3390/rs11212522. Number: 21 Publisher: Multidisciplinary Digital Publishing Institute.

Mann, J. (1994). The spatial structure of neutral atmospheric surface-layer turbulence. *Journal of Fluid Mechanics*, *273*, 141–168. URL: https://www.cambridge.org/core/product/identifier/S0022112094001886/type/journal_article. doi:10.1017/S0022112094001886.

Mann, J., Cariou, J.-P. C., Parmentier, R. M., Wagner, R., Lindelöw, P., Sjöholm, M., & Enevoldsen, K. (2009). Comparison of 3D turbulence measurements using three staring wind lidars and a sonic anemometer. *Meteorologische Zeitschrift*, *18*, 135–140. URL: http://www.schweizerbart.de/papers/metz/detail/18/57207/Comparison_of_3D_turbulence_measurements_using_thr?af=crossref. doi:10.1127/0941-2948/2009/0370.

Maré, M. d., & Mann, J. (2014). Validation of the Mann spectral tensor for offshore wind conditions at different atmospheric stabilities. *Journal of*

Physics: Conference Series, *524*, 012106. URL: https://dx.doi.org/10.1088/1742-6596/524/1/012106. doi:10.1088/1742-6596/524/1/012106.

Monin, A. S. (1958). The Structure of Atmospheric Turbulence. *Theory of Probability & Its Applications*, *3*, 266–296. URL: https://epubs.siam.org/doi/abs/10.1137/1103023. doi:10.1137/1103023. Publisher: Society for Industrial and Applied Mathematics.

Monin, A. S., & Obukhov, A. M. (1954). Basic laws of turbulent mixing in the surface layer of the atmosphere. *Contrib. Geophys. Inst. Acad. Sci. USSR*, *24*, 163–187.

Newland, D. (2012). *An Introduction to Random Vibrations, Spectral & Wavelet Analysis: Third Edition*. Dover Civil and Mechanical Engineering. Dover Publications. URL: https://books.google.no/books?id=mE9owVg1U1IC.

Olesen, H. R., Larsen, S. E., & Højstrup, J. (1984). Modelling velocity spectra in the lower part of the planetary boundary layer. *Boundary-Layer Meteorology*, *29*, 285–312. URL: https://doi.org/10.1007/BF00119794. doi:10.1007/BF00119794.

Pal, S., & Lee, T. R. (2019). Contrasting Air Mass Advection Explains Significant Differences in Boundary Layer Depth Seasonal Cycles Under Onshore Versus Offshore Flows. *Geophysical Research Letters*, *46*, 2846–2853. URL: https://onlinelibrary.wiley.com/doi/abs/10.1029/2018GL081699. doi:10.1029/2018GL081699. _eprint: https://onlinelibrary.wiley.com/doi/pdf/10.1029/2018GL081699.

Peña, A., Gryning, S.-E., & Mann, J. (2010). On the length-scale of the wind profile. *Quarterly Journal of the Royal Meteorological Society*, *136*, 2119–2131. URL: https://onlinelibrary.wiley.com/doi/abs/10.1002/qj.714. doi:10.1002/qj.714. _eprint: https://onlinelibrary.wiley.com/doi/pdf/10.1002/qj.714.

Puccioni, M., & Iungo, G. V. (2021). Spectral correction of turbulent energy damping on wind lidar measurements due to spatial averaging. *Atmospheric Measurement Techniques*, *14*, 1457–1474. URL:

https://amt.copernicus.org/articles/14/1457/2021/. doi:10.5194/amt-14-1457-2021. Publisher: Copernicus GmbH.

Reuder, J., Cheynet, E., Clifton, A., van Dooren, M. F., Gottschall, J., Jakobsen, J. B., Mann, J., Palma, J., Schlipf, D., Sjøholm, M., Trujillo, J.-J., Thobois, L., Würth, I., & Zasso, A. (2021). Recommendation on use of wind lidars. *33*, . URL: https://uis.brage.unit.no/uis-xmlui/handle/11250/3051025. doi:10.5281/zenodo.4672351. Accepted: 2023-02-15T11:01:17Z Publisher: Geophysical Institute and Bergen Offshore Wind Centre (BOW) University of Bergen.

Sathe, A., Mann, J., Barlas, T., Bierbooms, W., & van Bussel, G. (2013). Influence of atmospheric stability on wind turbine loads. *Wind Energy*, *16*, 1013–1032. URL: https://onlinelibrary.wiley.com/doi/abs/10.1002/we.1528. doi:10.1002/we.1528. _eprint: https://onlinelibrary.wiley.com/doi/pdf/10.1002/we.1528.

Sjöholm, M., Mikkelsen, T., Mann, J., Enevoldsen, K., & Courtney, M. (2009). Spatial averaging-effects on turbulence measured by a continuous-wave coherent lidar. *Meteorologische Zeitschrift*, *18*, 281–287. doi:10.1127/0941-2948/2009/0379.

Solari, G., & Piccardo, G. (2001). Probabilistic 3-D turbulence modeling for gust buffeting of structures. *Probabilistic Engineering Mechanics*, *16*, 73–86. URL: https://www.sciencedirect.com/science/article/pii/S0266892000000102. doi:10.1016/S0266-8920(00)00010-2.

Stull, R. B. (1988). *An Introduction to Boundary Layer Meteorology*. (1st ed.). Dodrecht, The Netherlands: Kluwer Academic Publishers.

Taylor, G. I. (1997). The Spectrum of Turbulence. *Proceedings of the Royal Society of London. Series A - Mathematical and Physical Sciences*, *164*, 476–490. URL: https://royalsocietypublishing.org/doi/abs/10.1098/rspa.1938.0032. doi:10.1098/rspa.1938.0032. Publisher: Royal Society.

Veers, P., Dykes, K., Lantz, E., Barth, S., Bottasso, C. L., Carlson, O., Clifton, A., Green, J., Green, P., Holttinen, H., Laird, D., Lehtomäki, V., Lundquist, J. K., Manwell, J., Marquis, M., Meneveau, C., Moriarty, P.,

Munduate, X., Muskulus, M., Naughton, J., Pao, L., Paquette, J., Peinke, J., Robertson, A., Sanz Rodrigo, J., Sempreviva, A. M., Smith, J. C., Tuohy, A., & Wiser, R. (2019). Grand challenges in the science of wind energy. *Science*, *366*, eaau2027. URL: https://www.science.org/doi/10.1126/science.aau2027. doi:10.1126/science.aau2027.

Wiley, W., Jonkman, J., Robertson, A., & Shaler, K. (2023). Sensitivity analysis of numerical modeling input parameters on floating offshore wind turbine loads. *Wind Energy Science*, *8*, 1575–1595. URL: https://wes.copernicus.org/articles/8/1575/2023/. doi:10.5194/wes-8-1575-2023. Publisher: Copernicus GmbH.